Multi–dimensional Polarized Radiative Transfer Modeling of Titan's Atmosphere

Santo Valentín Salinas Cortijo

International Max Planck Research School
on Physical Processes in the Solar System and Beyond

Multi–dimensional Polarized Radiative Transfer Modeling of Titan's Atmosphere

Dissertation
zur Erlangung des Doktorgrades
der Mathematisch–Naturwissenschaftlichen Fakultäten
der Georg–August–Universität zu Göttingen

vorgelegt von
Santo Valentín Salinas Cortijo
aus Chimbote / Perú

Göttingen 2003

Bibliografische Information Der Deutschen Bibliothek
Die Deutsche Bibliothek verzeichnet diese Publikation in der Deutschen Nationalbibliografie; detaillierte bibliografische Daten sind im Internet über `http://dnb.ddb.de` abrufbar.

D7

Referent: Prof. Dr. Franz Kneer

Korreferent: Dr. habil. Horst Uwe Keller

Tag der mündlichen Prüfung: 23. June 2003

Copyright © Copernicus GmbH 2003

ISBN 3–936586–15–2

Copernicus GmbH, Katlenburg-Lindau
Satz & Coverdesign: Santo Salinas
Front picture credit: ESA
Druck: Schaltungsdienst Lange, Berlin

Printed in Germany

Galileo's intellectual heir, Christiaan Huygens, the landed son of a Dutch diplomat who made science his life ..., had divined that the "moons" Galileo observed at Saturn where really a ring, impossible as that seemed at the time. Huygens also discovered Saturn's largest moon, which he called Titan ...

Dava Sobel
Longitude

DEDICATED TO
ELSIE...

Abstract

The purpose of this thesis work is to develop a multi–dimensional radiative transfer model which includes polarization to model Titan's internal radiation field. This model is developed in the framework of the *Cassini–Huygens* mission to the Saturnian system and posterior *Huygens* probe landing on Titan in early 2005. The model is capable of solving the mono–chromatic radiative transfer equation in full spherical geometry. The algorithm is initialized with a 1–D *doubling & adding* scheme and the multi–dimensional problem is effectively solved by the method of *characteristics*. Polarization is considered by using the four Stokes parameters and the 4×4 scattering phase matrix. The radiative transfer equation is solved for systems containing thermal or collimated solar radiant sources. Boundary conditions account for two types of surface reflection, i.e. Fresnel and Lambert types.

The model development can be split in the following steps:

- Implementation of a 1–dimensional radiative transfer model, including polarization, for multiple scattering atmospheres. The method of choice is the doubling and adding method since it is know to be very efficient for optically thick atmospheres.
- Introduction of a spherical correction for the the direct solar beam to obtain a pseudo–spherical solution. This is done to obtain a good initial guess solution for an iteration scheme which will be used for the full multi–dimensional case.
- Implementation of the Characteristics method to fully solve the polarized radiative transfer equation for a spherical planetary atmosphere. The 3–D radiative transfer equation is effectively solved using an iterative scheme known as the Picard approximation.
- Setting the appropriate atmospheric scenario for Titan's case by embedding its atmospheric parameters in an appropriate form to be directly assimilated by our radiative transfer model.

Another aspect of this research is to apply the model to Titan's atmosphere using its atmospheric properties as they are known to date. A new microphysical model that describes the scattering properties of Titan's aerosols, using the concept of *fractal aggregates*, is introduced and used extensively. Simulation results for the internal polarized radiation field of Titan are presented considering the geometry, frequency, angular resolution and other parameters prescribed for *Huygens* experiments which will take place in early 2005.

Contents

1 Introduction **1**

2 Polarized radiative transfer theory **5**
2.1 Radiative transfer and polarization 5
2.1.1 Polarization ellipse 5
2.1.2 Stokes parameters 7
2.1.3 Mueller matrix 9
2.2 The radiative transfer equation 10

3 Multi–dimensional polarized radiative transfer **17**
3.1 Radiative transfer in curvilinear coordinates 17
3.2 Radiative transfer in spherical coordinates 19
3.3 Spherical atmospheres: Special cases 22

4 Polarized radiation in plane–parallel atmospheres **25**
4.1 The plane–parallel problem 25
4.2 The plane–parallel model 26
4.3 Interaction principle 28
4.3.1 Adding two layers 29
4.3.2 Building the radiation field 32
4.4 The solution method: Doubling and adding 33
4.4.1 The polarized scattering matrix 33
4.4.2 Fourier expansion of the Stokes vector and Scattering matrix . . . 35
4.4.3 The discretized angular grid 37
4.4.4 The discretized spatial grid 38
4.4.5 Boundary conditions 38
4.4.6 Application of the doubling and adding method 40
4.5 The pseudo–spherical approximation 41
4.6 Numerical results 43
4.6.1 Plane parallel tests 43
4.6.2 Pseudo–spherical tests 44

5 Polarized radiation in spherical atmospheres **51**
5.1 Methods of computational radiative transfer 51
5.1.1 Monte Carlo method 52

5.1.2 Methods involving Fourier series . . . 53
5.1.3 Method of moments . . . 54
5.1.4 Other methods . . . 55
5.2 Characteristics method . . . 55
5.2.1 The initial field . . . 58
5.2.2 Multidimensional integration of the RTE . . . 59
5.2.3 Sweeping scheme . . . 61
5.3 Numerical results . . . 62
5.3.1 Convergence of iterative scheme . . . 62
5.3.2 Solar angle variation . . . 62
5.3.3 Validation tests . . . 63

6 Titan **73**
6.1 Introduction . . . 73
6.2 Titan's atmosphere . . . 75
6.2.1 Atmospheric components . . . 75
6.2.2 Thermal structure . . . 76
6.3 Aerosols and condensates : Titan's haze layer . . . 79
6.3.1 Titan's haze in the visible . . . 80
6.3.2 Titan's geometric albedo . . . 80
6.3.3 Imaging and photo–polarimetry . . . 81
6.4 Microphysical models of Titan's aerosols . . . 83
6.4.1 Scattering properties of the haze: Fractal aggregates . . . 83
6.4.2 Microphysical and optical model of the Titan haze . . . 84
6.5 The Cassini–Huygens mission . . . 85

7 Modeling Titan's atmosphere **89**
7.1 Titan atmospheric scenario . . . 89
7.1.1 Microphysical and optical model of the Titan haze . . . 89
7.1.2 Setting up the atmospheric scenario . . . 90
7.2 Results of Titan's simulated solar aureole . . . 91
7.2.1 Spherical/Plane–parallel Intensity comparison . . . 92
7.2.2 Titan's solar aureole at 50° and 90° solar angle . . . 94
7.3 Discussion and conclusions . . . 96

Summary and conclusions **97**

Bibliography **99**

Acknowledgments **107**

Scientific contributions **109**

Lebenslauf **111**

List of Figures

2.1 Elliptical polarization. Top: Decomposition of the electric wave vector $\mathbf{E}$ into two sinusoidal components $\mathbf{E}_v$ and $\mathbf{E}_h$. Bottom: Polarization ellipse, the tip of $\mathbf{E}$ describes an ellipse in the (x, y) plane. 6

2.2 Polarization representation in a Poincaré sphere. The point shown has coordinates (Q, U, V) and radius I. 8

2.3 Interaction of a beam of light with an element $dV = d\sigma dh$ (Sobolev 1975) 12

3.1 Definition of spherical coordinate system. 19

4.1 Geometry of the plane–parallel approximation and local angular reference frame. 27

4.2 The interaction principle. 29

4.3 Combining two layers. Layers a and b can together be combined in a single layer c. 30

4.4 Reflection (R), transmission (T) and source (Σ) matrices in an atmospheric layer[1]. 33

4.5 Polarization reference frame. 34

4.6 Schematic representation of the atmospheric layers, for a plane parallel model, indicating the optical depths and interfaces of the multi-layered atmosphere. 38

4.7 Schematic representation of a pseudo–spherical atmosphere. 41

4.8 Path-lengths between spherical shells. 42

4.9 Rayleigh polarized phase matrix. 46

4.10 Stokes I, Q, U and V % difference comparison between our model and Evans & Stephens (1991) model (RT3) for a Rayleigh type atmosphere. . 46

4.11 Polarized phase matrix for Mie type particles. 47

4.12 Stokes I, Q, U and V % difference comparison between our model and Evans & Stephens (1991) model (RT3) for a Mie type atmosphere. 47

4.13 Pseudo–spherical vs. plane–parallel % differences for a Mie atmosphere for I, Q, U and V Stokes components, Solar angle = 78°. azimuth = 0° . . 48

4.14 Pseudo–spherical vs. plane–parallel % differences for a Mie atmosphere for I, Q, U and V Stokes components, Solar angle = 78°, azimuth = 90° . 48

4.15 Pseudo–spherical vs. plane–parallel % differences for a Mie atmosphere for I, Q, U and V Stokes components, Solar angle = 78°. azimuth = 180° 49

4.16 Pseudo–spherical vs. plane–parallel % differences for a Mie atmosphere for I, Q, U and V Stokes components, Solar angle = 0°. 49
4.17 Pseudo–spherical vs. plane–parallel % differences for Titan's atmosphere at 450km. and solar zenith angle = 50° 50
4.18 Pseudo–spherical vs. plane–parallel % differences for Titan's atmosphere at ground level and solar zenith angle = 50° 50

5.1 Characteristic integration along the line of sight for a spherical atmosphere. 59
5.2 The icosahedron–based pixelization scheme. Each dot represents an integration node which are used to pixelize the unit sphere. 60
5.3 Relative difference between global iterations, i.e. $(I_{dif}^{(n+1)}/I_{dif}^{(n)} - 1) * 100\%$ as function of zenith angle and azimuth angle at 100 km. altitude and solar zenith angle 50^o. 63
5.4 Radiance variation with solar angle for a set of line of sight view at a fixed azimuth angle. 64
5.5 Plane–parallel calculation for Titan's atmosphere at solar zenith angle = 56°. 68
5.6 Spherical calculation with large radius ($r = 1000 * R_{titan}$) for Titan's atmosphere at solar zenith angle = 56°. 68
5.7 The diffuse downward intensity I as seen from the Martian surface for two wavelengths 69
5.8 The diffuse intensity I for 443.6 nm as seen from the top of Mars atmosphere 70
5.9 Diffuse intensity I as seen from the Martian surface at 443.6 nm 71

6.1 Vertical temperature profile of Titan's atmosphere 77
6.2 This figure illustrates Chassefière & Cabane (1995) model of Titan haze formation. (Source: Cassini INMS.) 79
6.3 The *Voyager 1* spacecraft's historic tour 82
6.4 The geometric albedo of Titan from International Ultraviolet Explorer $0.2 - 0.3\mu$m and ground based observations. 82

7.1 The cumulative optical depth and single scattering albedo of the model atmosphere as a function of altitude for the two wavelengths of the *SA*. . . 90
7.2 Phase functions example at 100 km for the two wavelengths of the *SA*. . . 91
7.3 Intensities: Plane–parallel (left) vs. spherical (right) model at 500 nm . . 92
7.4 Linear polarization: Plane–parallel (left) vs. spherical (right) model at 500 nm 93
7.5 Variation of the Intensity field for several azimuth angles 94
7.6 Variation of the Intensity field for several azimuth angles 94
7.7 Internal radiation at solar zenith angles 90^o at several altitudes 95

List of Tables

4.1 Sample pivots and weights for Gaussian quadrature of order eight 37

5.1 The optical depth and single scattering properties derived from Sol 56 data (Markiewicz et al. 1999, 2002) 66

6.1 Titan physical data from *Voyager 1* obsevations 74
6.2 Chemical composition of Titan's atmosphere (adapted from Gautier, 1992 and Raulin et al., 1995) 75
6.3 Fractal dimension for different aggregation models (adapted from Cabane & Chassefiere (1993)) 84

Chapter 1

Introduction

This thesis deals with multiple scattering of polarized radiation in planetary atmospheres, specifically in the atmosphere of Titan. Apart from this introductory chapter, 6 chapters are dedicated to the topic, starting from general concepts on which the later chapters depend. Detailed introductions to the basic concepts in each chapter have been avoided. Such introductions can be found in many books (Chandrasekhar 1965, Van de Hulst 1957, Sobolev 1975, Lenoble 1985, Goody & Yung 1989). In addition, we refer to Coustenis & Taylor (1999) for a modern view on Titan and to several publications and articles with an up–to–date of on going research on Titan's atmosphere.

Titan, Saturn's biggest moon and (by a narrow margin) the second in size among the satellites of our solar system had been known for a long time to have a substantial atmosphere. The Catalan astronomer José Comas Solá claimed in 1908 to have observed limb darkening on Titan. This is the effect whereby the solar light reflected back to Earth by Titan's limb shows an attenuation that is stronger than from it's centre, this usually implies an atmosphere. Confirmation of an atmosphere comes from spectroscopic observations by Kuiper in the 1940's but it was not known until the *Voyager I* spacecraft was re–directed to visit Titan in 1980 that the composition and surface pressure where similar to those on Earth. Furthermore, complex organic chemistry is active there and is probably responsible for the presence of haze, and possibly clouds, at various levels. In the optical range of wavelengths Titan is hidden under a thick orange veil of organic fog so that among many other things we do not know today what is the exact structure of the lower atmosphere nor what makes up its surface, except that the crust below the surface must be mainly ice (Coustenis & Taylor 1999).

To unveil all of these mysteries, an international space mission called *Cassini/Huygens* has been launched to the Saturnian system, its arrival is expected for July 2004 and *Huygens* descent into Titan's atmosphere for early 2005. Several experiments will be carried out by *Cassini/Huygens* mission instruments. One of them, the Descent Imager / Spectral Radiometer (DISR) on board *Huygens* is of special interest in the context of this thesis work. DISR will perform upward and downward looking measurements of the radiation field at various spectral ranges and and spatial resolutions. DISR data analysis requires the development of sophisticated radiative transfer models. These models will allow us

to retrieve the composition of the atmosphere and the optical properties of Titan's haze. Haze properties such as aerosol shape and abundance, absorption coefficients, single scattering albedo, phase functions, degree of polarization etc., will be inferred from radiative transfer computations and inverse retrieval algorithms.

Several computational methods exist for the treatment of polarized radiation scattered in planetary atmospheres. Most methods are however one–dimensional and only able to treat plane–parallel atmospheres. Among these one–dimensional methods, the so–called doubling & adding method has proved to be very efficient for polarized radiative transfer. The method has been studied in detail by Hansen & Travis (1974), Van de Hulst (1957), Lenoble (1985). With this method, not only the radiation reflected and transmitted in a vertically inhomogeneous atmosphere with uni–directional radiation incident at the top can be calculated, but also the internal radiation. The doubling & adding scheme is started with and optically thin homogenous layer whose reflection and transmission properties are accurately given by the first order of scattering (an analytical single scattering approximation). Using this method we can study polarized radiation in a vertically inhomogeneous atmosphere illuminated by **(a)** an unidirectional beam of light incident on the top, **(b)** isotropically radiating internal thermal sources and **(c)** an isotropically radiating surface. As a starting point, we consider the algorithmic structure of the method and build a scheme able to compute polarized radiation in vertically inhomogeneous plane–parallel atmospheres for the same three types of illumination.

These one–dimensional methods are not longer valid when the Sun is close or below the horizon or when measurements are taken from inside the atmosphere at almost horizontal viewing directions. In this situation, it is necessary to take the spherical nature of the atmosphere into account. At the present, the theory of light scattering in a spherical atmosphere is still under continuous development. This is understandable because of the difficulty and complexity of the problem, but with the ever larger computing capabilities of today's computers this problem is more tractable. Therefore, adequate models coupled with efficient algorithms are necessary to approach and solve the problem. One of our goals is to contribute on the solution to this problem for Titan's case.

To successfully analyze and evaluate observations obtained from *Huygens* descent on Titan, a model able to handle spatial variations in spherical atmospheres is required. Radiative transfer models able to handle multi–dimensional geometries are available in the scientific community, such as the moment method, discrete ordinates, characteristics, Monte Carlo, etc. Unfortunately, several of these algorithms are developed for Cartesian geometry only, do not include polarization or are computationally expensive. Approximations to simplify the problem are often used such as the pseudo–spherical approximation. However, this approximation fails to account for global angular variation along the line of sight and variations of the solar zenith angle. Furthermore, this method cannot handle solar angles near or below the horizon and includes surface views that otherwise dot not appear in a real spherical atmosphere.

In this thesis work, we present a combined approach for radiation transport in a three–

dimensional spherical planetary atmosphere. The method is based on a combination of one–dimensional polarized doubling and adding algorithm, the Picard–iterative approximation and the long characteristics method to construct an algorithm able to handle polarized radiation in Titan's atmosphere. The method is however general and could, in principle, be adapted to other planetary atmospheres with minor changes.

In the remainder of this introductory chapter, we give a brief outline of this thesis. Apart from this introduction, in chapter 2 we give the basic necessary theory needed for understanding polarized radiation transfer. The polarized radiative transfer equation is introduced and the process of polarization is explained. In chapter 3 we introduce the necessary mathematics for the treatment of polarized radiation in general curvilinear geometries. Chapter 4 analyses the plane–parallel problem and develops an approach for its solution via the doubling & adding method. The *Interaction Principle* is introduced as a fundamental part of the solution method. Chapter 5 gives a general overview of the numerical methods available for multi–dimensional radiative transfer and introduces the characteristic method as our method of choice. The mathematics from chapter 3 are applied to the development of a multi–dimensional radiation model in spherical geometry. Chapters 6 is largely dedicated to the atmospheric properties of Titan. An overview of the *Cassini/Huygens* mission and its proposed goals are discussed. Chapter 7 builds upon the knowledge of the previous chapters and presents simulated results for polarized radiation in Titan's atmosphere in the context of *Huygens/DISR* prescribed experiments. A new microphysical model for Titan's haze is introduced and used in these simulations. These results are reported in two submitted papers (one main authored and one co–authored) which are included in the bibliography.

The multi–dimensional radiative transfer method presented in this thesis involves long and tedious computations in which errors might easily occur. Therefore, tabulated benchmark results are included where available. Suitable tests are performed for plane–parallel and pseudo–spherical geometries. Accurate numerical solutions are hardly available in the literature for the spherical solution, specially for the polarized case. Therefore, we present some numerical results based on limiting cases and include a comparison case with measured radiances inside Mars atmosphere. Computational benchmarks such as timing and iterative convergency are also presented.

Finally, our goal in pursuing this research was to bring together the theoretical aspects of planetary physics, radiation transfer and scientific computing to give a preview of the immense possibilities of inter–disciplinary research. This goal is not only applicable for our specific case but for all scientific ventures. We hope to have met our goal.

Chapter 2

Polarized radiative transfer theory

In the following sections, we review the concept of polarized light in the context of radiation transfer for planetary atmospheres. Since all scattering processes leads to polarization, scattering problems that can be solved without explicit reference to the state of polarization of the incident and scattered light are exceptional. To describe polarization, we have to turn our attention to Maxwell's theory of electrodynamics and the central ideas that underly all electromagnetic waves. To understand the many facets of light polarization one must understand the fundaments of the classic theory of electromagnetic radiation and its interaction with matter. The interaction of this radiation field (monochromatic plane waves) with matter is the domain of radiative transfer theory.

2.1 Radiative transfer and polarization

2.1.1 Polarization ellipse

As a starting point, this section introduces the topic of polarization. To discuss this some background in electromagnetic theory is necessary (Jackson 1962, Cheng 1989). Only a few basic ideas will be discussed therein. Consider Fig.(2.1) which depicts a planar transverse electromagnetic wave (it has only x– and y– components) propagating through some medium. This plane wave is characterized by orthogonal electric and magnetic vector **E** and **H**, each perpendicular to the direction of propagation. The flow of energy and wave propagation is described by the Poynting vector,

$$\mathbf{S} = \mathbf{E} \times \mathbf{H}. \tag{2.1}$$

Because **E** and **H** are related to each other, the following discussion applies to both of them. However, it is customary to use vector **E** for this purpose. Fig.(2.1) shows how **E** is decomposed into its orthogonal components $\mathbf{E}_v$ and $\mathbf{E}_h$, the subscript v stands for "vertical" referring to the axes parallel to the plane of reference through the direction of propagation and subscript h stands for "horizontal" representing the axes perpendicular to this same reference plane. The selection of the plane of reference is arbitrary but

for scattering problems is usually assumed to be the plane containing the incident and scattered beam and thus referred to as the scattering plane.

The term polarization refers to the time–varying behaviour of **E** at a given point in space as shown in Fig.(2.1) where the tip of **E**, over time, is a path that lies in the plane perpendicular to the direction of propagation. In general, the components $\mathbf{E}_v$ and $\mathbf{E}_h$ may be expressed as

$$\mathbf{E}_v = a_v e^{[-i(\eta+\delta_v)]}, \tag{2.2}$$

$$\mathbf{E}_h = a_h e^{[-i(\eta+\delta_h)]}, \tag{2.3}$$

where a_v and a_h are amplitudes, δ_v and δ_h are phases, $\eta = kz - \omega t$, $k = 2\pi/\lambda$ is the propagation constant (or wavenumber) at wavelength λ, and $\omega(= kc_0)$ is the circular frequency with the speed of light in vacuum c_0.

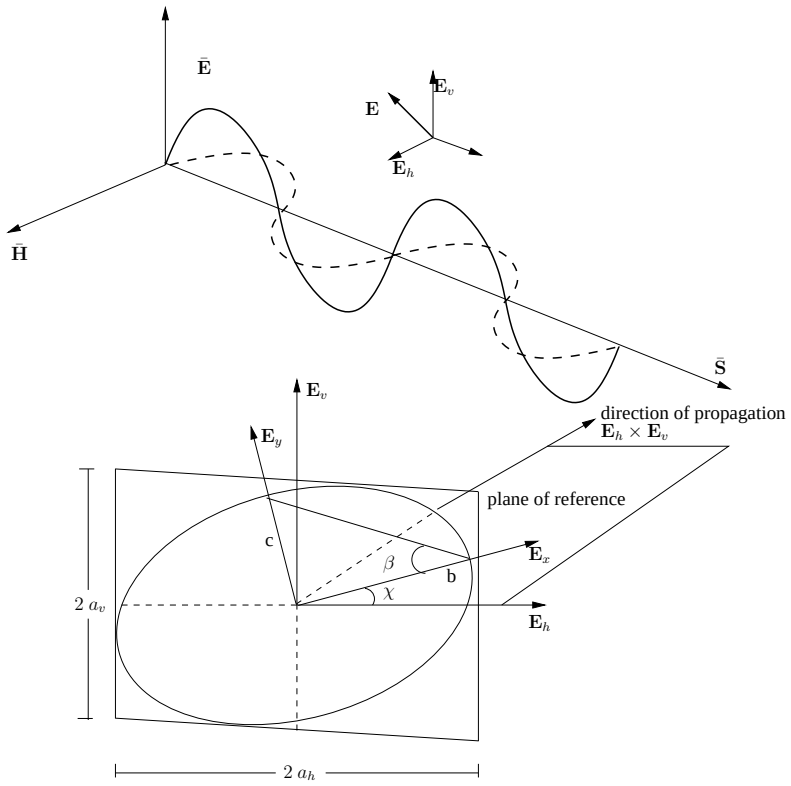

FIGURE 2.1: Elliptical polarization. Top: Decomposition of the electric wave vector **E** into two sinusoidal components $\mathbf{E}_v$ and $\mathbf{E}_h$. Bottom: Polarization ellipse, the tip of **E** describes an ellipse in the (x, y) plane.

Using these equations it may be shown (Liou 1980) that in general the path of the tip of the electric field vector is defined by the equation of an ellipse. Some of the parameters used to describe the polarization ellipse in Fig.(2.1) are the orientation angle χ, the

ellipticity β, the semi–major and –minor axes length b and c and the electric field amplitudes a_v and a_h. The polarization is called right handed for $\tan\beta > 0$ and left handed for $\tan\beta < 0$ and corresponds to a helix traced in space by the tip of the electric field vector. Notice that two sets of basis vectors are shown for the electric field: $\mathbf{E}_x$ and $\mathbf{E}_y$ are defined by a plane referred to as the meridional plane (y– axis and the direction of travel), while $\mathbf{E}_v$ and $\mathbf{E}_h$ are defined by the scattering plane (defined by the the v– axis and the direction of travel. This topic is further discussed when polarization treatment is included in our radiative transfer model development.

2.1.2 Stokes parameters

The rate of flow of radiant energy across a unit area perpendicular to the direction of travel per unit solid angle and per unit wavelength interval is known as the radiant intensity. Because of the transverse nature of electromagnetic waves (time–varying behaviour of the electric and magnetic fields), intensity alone is insufficient to completely characterize radiant energy. However, for the complex electric field vector described by the vertical and horizontal components $\mathbf{E}_v$ and $\mathbf{E}_h$ with phase differences $\delta(=\delta_h - \delta_v)$ the radiant energy may be fully described by the stokes vector:

$$\mathbf{I} = (I, Q, U, V)^{\mathrm{T}}. \tag{2.4}$$

The Stokes parameters are defined for the plane wave $\mathbf{E}$ propagating through a differential solid angle $d\Omega$ in a medium with intrinsic impedances η and defined by

$$\begin{pmatrix} I \\ Q \\ U \\ V \end{pmatrix} d\Omega = \frac{1}{2\eta} \begin{pmatrix} \langle E_v E_v^\dagger + E_h E_h^\dagger \rangle \\ \langle E_v E_v^\dagger - E_h E_h^\dagger \rangle \\ \langle E_v E_h^\dagger + E_h E_v^\dagger \rangle \\ i\langle E_v E_h^\dagger - E_h E_v^\dagger \rangle \end{pmatrix} = \frac{1}{2\eta} \begin{pmatrix} \langle |E_v|^2 + |E_h|^2 \rangle \\ \langle |E_v|^2 - |E_h|^2 \rangle \\ \langle 2|E_v||E_h| \cos\delta \rangle \\ \langle 2|E_v||E_h| \sin\delta \rangle \end{pmatrix}. \tag{2.5}$$

The angular brackets in Eq.(2.5) indicate a time–average over an interval greater than 10^{-13}s and the superscript $(^\dagger)$ denotes complex conjugate. The Stokes parameters represent respectively, the radiant intensity, the amount or degree of polarization, the plane of polarization and the ellipticity of the energy beam as a function of the incoming and outgoing directions and position. These parameters are useful because they can be measured using optical elements such as polarizers and quarter wave plates.

The reason that time–averaging is used in Eq.(2.5) is that in general electromagnetic waves are never strictly monochromatic. They are usually pseudo–monochromatic with a bandwidth $\delta\omega$, and thus a_v, a_h and δ are all slowly varying functions of time. In such a wave, if the electric amplitudes fluctuate in time independent of each other they are then completely uncorrelated and the wave is said to be unpolarized. If a_v and a_h are partially correlated, the wave is say to be partially polarized, if they are completely correlated the wave is say to be fully polarized. Coulson (1988) defines unpolarized energy as energy that shows complete symmetry around the direction of propagation and partial polarization as a mixture of streams of both unpolarized and polarized energy.

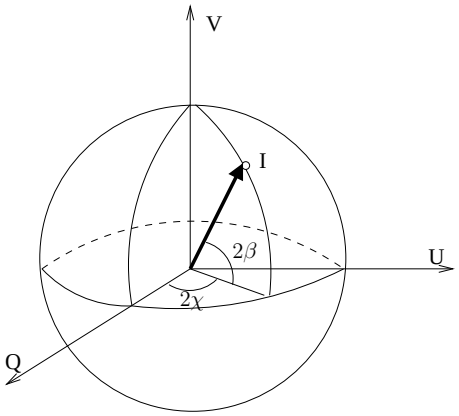

FIGURE 2.2: Polarization representation in a Poincaré sphere. The point shown has coordinates (Q, U, V) and radius I.

For a quasi–monochromatic wave it ca be shown that

$$I^2 \geq Q^2 + U^2 + V^2. \tag{2.6}$$

This condition becomes a strict equality when radiation is completely polarized, if $Q = U = V = 0$ then the beam is said to be unpolarized. This observation leads to the notion of "degree of polarization" defined as

$$Z = \frac{\sqrt{Q^2 + U^2 + V^2}}{I}. \tag{2.7}$$

For complete polarization $Z = 1$ and for unpolarized energy $Z = 0$ and in general $0 \leq Z \leq 1$. Two other quantities that are defined in terms of the Stokes parameters are used in polarized studies of planetary radiation, these are, the degree of linear polarization defined as

$$LP = \frac{\sqrt{Q^2 + U^2}}{I}, \tag{2.8}$$

and the circular polarization ratio,

$$CP = \frac{V}{I}. \tag{2.9}$$

The Stokes parameters may also be written in terms of the ellipso–metric parameters as

$$\begin{pmatrix} I \\ Q \\ U \\ V \end{pmatrix} = \begin{pmatrix} b^2 + c^2 \\ I\cos(2\beta)\cos(2\chi) \\ I\cos(2\beta)\sin(2\chi) \\ I\sin(2\beta) \end{pmatrix}, \tag{2.10}$$

this expression can be visualized using the Poincaré sphere as shown in Fig.(2.2). On this sphere, the radius is given by I and the triad (Q, U, V) represent Cartesian coordinates

of a point either on or inside the sphere. If the point is inside the sphere, partially polarized light is represented and if the point lies on the surface of the sphere, completely polarized light is represented. A point in the origin represents unpolarized energy. The northern and southern hemispheres represent right–handed and left–handed elliptic polarizations respectively and the equatorial plane represents linear polarization. The zenith and azimuthal angles are given by $\pi/2 - 2\beta$ and 2χ respectively.

2.1.3 Mueller matrix

For an electromagnetic wave with electric field components (E_{vi}, E_{hi}) incident on a particle of arbitrary shape and size, the scattered electric field (E_{vs}, E_{hs}) at a distance r from the particle is given by the far–field $(k\, r \gg 1)$ expression,

$$\begin{pmatrix} E_{vs} \\ E_{hs} \end{pmatrix} = \frac{e^{i\ k(r-y)}}{-i\ k\ r} \begin{pmatrix} S_2 & S_3 \\ S_4 & S_1 \end{pmatrix} \begin{pmatrix} E_{vi} \\ E_{hi} \end{pmatrix}, \tag{2.11}$$

where y is the vertical direction in Cartesian coordinates and S_j $(j = 1, \cdots, 4)$ are the complex amplitude functions that depend on the scattering angle and particle size and shape. Eq.(2.11) states that the amplitude of the scattered electric field is a linear function of the amplitude of the incident field. Computation of S_j is of primary importance because, as it will be shown later, the radiative properties used in the radiative transfer equation are obtained from this amplitudes.

In terms of the Stokes vector $\mathbf{I} = (I, Q, U, V)^T$, the relationship between incident and scattered radiation may be expressed mathematically as

$$\mathbf{I}_s = \frac{1}{k^2 r^2} \mathbb{M}\ \mathbf{I}_i, \tag{2.12}$$

where the scattering transformation matrix $\mathbb{M}$ is the 4×4 Mueller matrix also commonly referred to as the Stokes scattering matrix whose elements can be written in partitioned matrix form as

$$\mathbb{M} = \begin{pmatrix} M_{11} & M_{12} \\ M_{21} & M_{22} \end{pmatrix}, \tag{2.13}$$

where, the sub-matrices M_{ij} are written in terms of the scattering amplitude function as

$$M_{11} = \frac{1}{2} \begin{pmatrix} (|S_1|^2 + |S_2|^2 + |S_3|^2 + |S_4|^2) & (|S_2|^2 - |S_1|^2 + |S_4|^2 - |S_3|^2) \\ (|S_2|^2 - |S_1|^2 - |S_4|^2 + |S_3|^2) & (|S_2|^2 - |S_1|^2 - |S_3|^2 - |S_4|^2) \end{pmatrix}, \tag{2.14}$$

$$M_{12} = \frac{1}{2} \begin{pmatrix} \Re\{S_2 S_3^\dagger + S_1 S_4^\dagger\} & \Im\{S_2 S_3^\dagger - S_1 S_4^\dagger\} \\ \Re\{S_2 S_3^\dagger - S_1 S_4^\dagger\} & \Im\{S_2 S_3^\dagger + S_1 S_4^\dagger\} \end{pmatrix}, \tag{2.15}$$

$$M_{21} = \frac{1}{2} \begin{pmatrix} \Re\{S_2 S_4^\dagger + S_1 S_3^\dagger\} & \Im\{S_2 S_4^\dagger - S_1 S_3^\dagger\} \\ \Re\{S_2 S_4^\dagger + S_1 S_3^\dagger\} & \Im\{S_2 S_4^\dagger - S_1 S_3^\dagger\} \end{pmatrix}, \tag{2.16}$$

$$M_{22} = \frac{1}{2} \begin{pmatrix} \Re\{S_1 S_2^\dagger + S_3 S_4^\dagger\} & \Im\{S_1 S_2^\dagger + S_3 S_4^\dagger\} \\ \Re\{S_1 S_2^\dagger - S_3 S_4^\dagger\} & \Im\{S_1 S_2^\dagger - S_3 S_4^\dagger\} \end{pmatrix}, \tag{2.17}$$

where $\Re$ and $\Im$ denote the real and imaginary parts respectively. The elements of the Mueller matrix are determined using single particle scattering theory which is discussed in section 4.4.1. Because there are sixteen elements in the Mueller matrix that are constructed from four amplitudes and three phase differences, there must be nine independent relationships between these elements (Van de Hulst 1957). These relationships are presented explicitly by Fry & Katawar (1981) and are shown to be equalities for scattering by a single particle in a fixed orientation and inequalities for a poly–dispersion of particles.

If an incident beam passes through a succession of n particles whose Mueller matrices are given by $\mathbb{M}_1, \mathbb{M}_2, ..., \mathbb{M}_n$, then the effective Mueller matrix is obtained by multiplying together the Mueller matrices associated with each element, that is

$$\mathbb{M} = \mathbb{M}_n, \mathbb{M}_{n-1}...\mathbb{M}_1 = \prod_{i=1}^{n} \mathbb{M}_{n-i+1}, \tag{2.18}$$

as matrix multiplication is not commutative the matrices must be multiplied as shown.

2.2 The radiative transfer equation

Intensity is the basic quantity characterizing the radiation field. In astrophysical usage the word *intensity* denotes *specific intensity of radiation* i.e., the flux of energy in a given direction per second per unit wavelength range per unit solid angle per unit area perpendicular to the given direction (Goody & Yung 1989).

According to Sobolev (1975), the intensity at a given place in space in a particular direction is defined in the following manner. Let $d\sigma$ be an elementary area which is perpendicular to a chosen direction $\mathbf{\Omega}$ and the radiation falls in the frequency interval from ν to $\nu + d\nu$ in the solid angle $d\omega$ in the time dt, then the amount of radiant energy ξ falling on the area from the given direction $\mathbf{\Omega}$ will be proportional to $d\sigma d\nu d\omega dt$ i.e.,

$$\xi = I \; d\sigma \; d\nu \; d\omega \; dt. \tag{2.19}$$

The proportionality coefficient I is called the intensity of radiation. Generally speaking, the quantity I depends on the coordinates of the given point, on direction, on the frequency and on time. Time dependent radiative transfer will not be considered in this work i.e., the radiation field will always be considered to be stationary. For simplicity in our formulation neither polarization dependence on the intensity nor medium characteristics dependencies on frequency will be indicated in the following discussion.

An important characteristic of radiation intensity is the fact that in empty space it does not change along any ray at a certain distance from its source. The interactions between radiation and medium can be classed as either *extinction* or *emission*. The two processes are distinguished by the sign of the change of radiation intensity as a result of the interaction.

Extinction refers to *any process which reduces the intensity in the direction under consideration* and thus includes both scattering from the direction $\mathbf{\Omega}$ into another directions as well as absorption. The fraction of the energy incident on a layer of infinitesimal thickness ds which is removed from the original beam of radiation is defined as the *extinction*

coefficient

$$\xi_{\text{ext}} = \kappa \; ds \; \xi. \tag{2.20}$$

The *extinction coefficient* depends on the frequency of the radiation at a given point in a prescribed coordinate system. Thus, the energy removed in a volume element $dV = dsd\sigma$ from the ray falling on this volume element from the given direction in the solid angle $d\omega$ in the frequency interval from ν to $\nu + d\nu$ in the time period dt is given by

$$\xi_{\text{ext}} = \kappa \; ds \; I \; d\sigma \; d\nu \; d\omega \; dt. \tag{2.21}$$

Emission refers to any process which increases the intensity in the direction under consideration and thus includes both scattering into the beam from other directions as well as thermal or other emission processes within the volume element dV. The energy emitted by the volume element dV within the solid angle $d\omega$ in the frequency interval from ν to $\nu + d\nu$ in the time period dt can be written as a formal statement defining the source function S in the following manner:

$$\xi_{\text{emit}} = \kappa \; S \; ds \; d\sigma \; d\nu \; d\omega \; dt. \tag{2.22}$$

Considering the radiation entering and leaving the volume element dV within a solid angle $d\omega$ in the frequency interval from ν to $\nu + d\nu$ in the time period dt, the following relation for the difference between energy leaving and entering the volume element is obtained:

$$d\xi = dI \; d\sigma \; d\nu \; d\omega \; dt, \tag{2.23}$$

here, I and $I + dI$ are assumed to be the intensity where the ray enters the volume element and the intensity leaving the volume element respectively. Employing the energy conservation law the difference between the energy leaving and entering the volume element can then be written as,

$$d\xi = -\xi_{\text{ext}} + \xi_{\text{emit}}. \tag{2.24}$$

Substituting Eqs.(2.21),(2.23) into Eq.(2.24) results in,

$$dI \; d\sigma \; d\nu \; d\omega \; dt = -\kappa \; I \; ds \; d\sigma \; d\nu \; d\omega \; dt + \kappa \; ds \; S \; d\sigma \; d\nu \; d\omega \; dt. \tag{2.25}$$

It follows that,

$$\frac{dI}{ds} = -\kappa(I - S). \tag{2.26}$$

Equation (2.26) is the *radiative transfer equation* which determines the changes in the intensity of a radiation beam as it passes through an absorbing and emitting medium.

In UV–Visible–near IR spectral region the contribution of thermal emission processes to the source function is negligible and thus, the source function comprises only scattering processes. However, in the case of a medium which scatters radiation the quantity S depends on the intensity falling on the elementary volume from all directions.

Let an intensity I fall on an elementary volume with a cross section $d\sigma$ and a height dh within the solid angle $d\tilde{\omega}$ in the direction forming an angle $\tilde{\theta}$ with the normal to the base (see Fig. 2.3). It is apparent, from Eq.(2.19) that the energy falling on the volume per unit frequency interval per unit time is given by

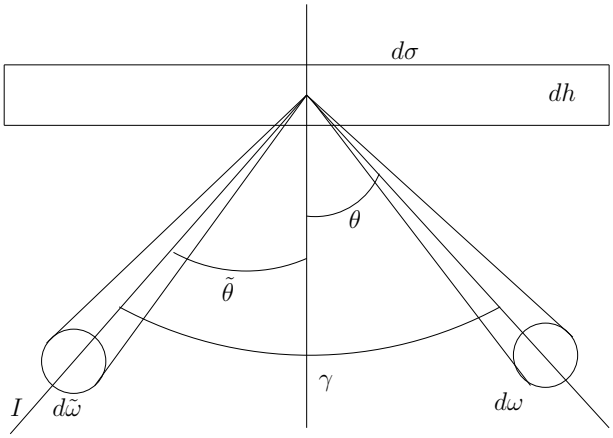

FIGURE 2.3: Interaction of a beam of light with an element $dV = d\sigma dh$ (Sobolev 1975)

$$\frac{\xi}{d\nu dt} = \mathbb{E} = I\ d\tilde{\omega}\ d\sigma\ \cos\tilde{\theta}. \tag{2.27}$$

Since the path traveled by the radiation in the volume is $dh \sec\tilde{\theta}$, a fraction $\kappa dh \sec\tilde{\theta}$ of the energy falling on the volume is absorbed by it i.e., removed from the incident beam so that the following relation for the absorbed energy holds:

$$\mathbb{E}_{\rm abs} = \kappa\ dh\ d\sigma\ I\ d\tilde{\omega}. \tag{2.28}$$

The energy scattered by the volume within the solid angle $d\omega$ in a given direction is found by multiplying the absorbed energy by the quantity $\varpi P(\gamma)d\omega/4\pi$ where γ is the angle between the directions of the incident and scattered radiation (*scattering angle*). The quantity ϖ represents the probability that a photon which interacts with an element of volume will be scattered rather than absorbed. It is called the *single scattering albedo*. The term $P(\gamma)d\omega/4\pi$ denotes the probability that the radiation is scattered into a solid angle $d\omega$ about a direction forming an angle γ with the direction of the incident radiation. The quantity $P(\gamma)$ is called the *phase function*. Clearly,

$$\int_{4\pi} P(\gamma)\frac{d\omega}{4\pi} = 1, \tag{2.29}$$

where the integration is carried out over all directions (unit sphere). Taking into account that $d\omega = 2\pi\sin\gamma d\gamma$, Eq.(2.29) can be rewritten as follows:

$$\frac{1}{2}\int_0^\pi P(\gamma)\sin\gamma d\gamma = 1. \tag{2.30}$$

The quantities ϖ and $P(\gamma)$ depend on the frequency of the radiation and coordinates of the given point. As a result, the following expression for the energy scattered within the solid angle $d\omega$ in a given direction θ is obtained from

$$\mathbb{E}_{\rm scatt} = \varpi P(\gamma)\kappa\frac{d\omega}{4\pi}dhd\sigma\ I\ d\tilde{\omega}. \tag{2.31}$$

Since the radiation falls on the elementary volume from all sides this expression has to be integrated over all directions of the incident radiation. It is evident that the result of this integration has to be equal to the total energy emitted within the solid angle $d\omega$ in the direction under consideration per unit frequency per unit time,

$$\varpi\kappa\frac{d\omega}{4\pi}dhd\sigma\int_{4\pi}P(\gamma)I(\tilde{\omega})d\tilde{\omega}=\frac{\xi_{\rm emit}}{d\nu dt}, \tag{2.32}$$

where $\xi_{\rm emit}$ is given by Eq.(2.22). Thus, combining Eqs.(2.22) and (2.32) the following equation for the scattering source function can be obtained:

$$S=\frac{\varpi}{4\pi}\int_{4\pi}P(\gamma)I(\tilde{\omega})d\tilde{\omega}. \tag{2.33}$$

Substituting Eq.(2.33) for the scattering source function into Eq.(2.26) leads to the integro–differential radiative transfer equation in a medium that absorbs and scatters radiant energy:

$$\frac{dI(\omega)}{ds}=-\kappa I(\omega)+\kappa\frac{\varpi}{4\pi}\int P(\gamma)I(\tilde{\omega})\,d\tilde{\omega}. \tag{2.34}$$

Here the thermal emission processes as well as the inelastic scattering were neglected.

In any planetary atmosphere, the radiation field I can be split into two components: the direct radiation which is never scattered in the atmosphere or reflected from the planetary surface and the diffuse radiation, which is scattered or reflected at least once,

$$I=I_{\rm dir}+I_{\rm dif}. \tag{2.35}$$

Since there is no process in the atmosphere which increases the intensity of the direct solar radiation, the radiative transfer equation for the direct radiation leads to the homogeneous differential equation,

$$\frac{dI_{\rm dir}(\mathbf{r},\mathbf{\Omega})}{ds}=-\kappa(\mathbf{r})I_{\rm dir}(\mathbf{r},\mathbf{\Omega}), \tag{2.36}$$

having the formal homogeneous solution,

$$I_{\rm dir}(\mathbf{r},\mathbf{\Omega_0})=C_0\exp\left(-\int_0^s\kappa(\hat{s})d\hat{s}\right). \tag{2.37}$$

The integration is performed from point $\mathbf{r}$ to the top of the atmosphere along the direction $\mathbf{\Omega_0}$ i.e., along the direct solar beam, s is the full path-length along the integration line and C_0 is an arbitrary constant. This constant can be determined using the following boundary condition at the top of the atmosphere (TOA),

$$I_{\rm dir}(\mathbf{r}^{\rm TOA},\Omega_0)=I_{\rm irr}, \tag{2.38}$$

where $I_{\rm irr}$ is the solar irradiance at the top of the atmosphere traveling in direction $\mathbf{\Omega_0}$. Substituting Eq.(2.38) into Eq.(2.37) the following general expression for the direct radiation, which is known as Lambert-Beer law, can be obtained:

$$I_{\rm dir}(\mathbf{r},\mathbf{\Omega_s}) = I_{\rm irr}\exp\left(-\int_0^s \kappa(\hat{s})d\hat{s}\right). \tag{2.39}$$

If the Sun, as a light source, is assumed to have an infinitesimal size so that there is no direct radiation traveling in directions different from $\mathbf{\Omega_0}$,

$$I_{\rm dir}(\mathbf{r},\mathbf{\Omega_s}) = F_0\delta(\mathbf{\Omega_s}-\mathbf{\Omega_0})\exp\left(-\int_0^s \kappa(\hat{s})d\hat{s}\right), \tag{2.40}$$

where F_0 is the incident solar flux and $\delta(\mathbf{\Omega_s}-\mathbf{\Omega_0})$ is the Dirac-delta function.

Substituting Eq.(2.35) into Eq.(2.33) the following relation for the total source function $S(\mathbf{r},\mathbf{\Omega_s})$ can be obtained:

$$S(\mathbf{r},\mathbf{\Omega_s}) = \frac{\varpi}{4\pi}\int_{4\pi} P(\mathbf{r},\gamma)I_{\rm dif}(\mathbf{r},\mathbf{\Omega_s})d\tilde{\omega} + \frac{\varpi}{4\pi}F_0P(\mathbf{r},\gamma_0)\exp\left(-\int_0^s \kappa(\hat{s})d\hat{s}\right), \tag{2.41}$$

here γ_0 is the angle between the direction $\mathbf{\Omega_0}$ of the incident direct solar beam and direction $\mathbf{\Omega_s}$ of the scattered radiation. In Eq.(2.41) we can recognize two different terms: the first term of the right hand side is the the multiple scattering term and the other is due to single scattering processes,

$$S_{\rm ms}(\mathbf{r},\mathbf{\Omega_s}) = \frac{\varpi}{4\pi}\int_{4\pi} P(\mathbf{r},\gamma)I_{\rm dif}(\mathbf{r},\mathbf{\Omega_s})d\tilde{\omega}, \tag{2.42}$$

$$S_{\rm ss}(\mathbf{r},\mathbf{\Omega_s}) = \frac{\varpi}{4\pi}F_0P(\mathbf{r},\gamma_0)\exp\left(-\int_0^s \kappa(\hat{s})d\hat{s}\right). \tag{2.43}$$

In compact form, Eq(2.41) can be written as,

$$S(\mathbf{r},\mathbf{\Omega_s}) = S_{\rm ss}(\mathbf{r},\mathbf{\Omega_s}) + S_{\rm ms}(\mathbf{r},\mathbf{\Omega_s}). \tag{2.44}$$

Therefore, the total source function can be split into two terms the multiple scattering and the single scattering source function respectively.

Since direct radiance contains a delta function, its more convenient to solve the radiative transfer equation Eq.(2.26) or Eq.(2.34) only for diffuse radiance to avoid the discontinuity, i.e., the following equation has to be solved to obtain the diffuse radiation inside the atmosphere,

$$\frac{dI_{\rm dif}(\mathbf{r},\mathbf{\Omega})}{ds} = -\kappa(\mathbf{r})\left[I_{\rm dif} - S_{\rm ms}(\mathbf{r},\mathbf{\Omega_s}) - S_{\rm ss}(\mathbf{r},\mathbf{\Omega_s})\right]. \tag{2.45}$$

So far, all of our treatment has been developed for the scalar case of radiation transfer. We now include polarization into our theory (see section 2.1) our previous development still compleatly valid but the intensity now becomes a vector field in the form of the so called four–vector of Stokes parameters $\mathbf{I}(I,Q,U,V)$. Furthermore, the phase matrix P is now the four–by–four scattering or Mueller matrix $\mathbb{M}$ and all sources of single and multiple scattering are four–vectors as well. Rewriting Eq.(2.42) and Eq.(2.43) we obtain

$$\mathbf{S}_{\rm ms}(\mathbf{r},\mathbf{\Omega_s}) = \frac{\varpi}{4\pi}\int_{4\pi} \mathbb{M}(\mathbf{r},\gamma)\mathbf{I}_{\rm dif}(\mathbf{r},\mathbf{\Omega_s})d\tilde{\omega}, \tag{2.46}$$

$$\mathbf{S}_{\rm ss}(\mathbf{r},\mathbf{\Omega_s}) = \frac{\varpi}{4\pi} F_0 \mathbb{M}(\mathbf{r},\gamma_0) \exp\left(-\int_0^s \kappa(\hat{s}) d\hat{s}\right) \begin{pmatrix} 1 \\ 0 \\ 0 \\ 0 \end{pmatrix}. \tag{2.47}$$

Eq.(2.44) then becomes

$$\mathbf{S}(\mathbf{r},\mathbf{\Omega_s}) = \mathbf{S}_{\rm ss}(\mathbf{r},\mathbf{\Omega_s}) + \mathbf{S}_{\rm ms}(\mathbf{r},\mathbf{\Omega_s}). \tag{2.48}$$

Finally, we can generalize Eq.(2.26) or Eq.(2.34) to include polarized radiation applicable to an arbitrary geometry,

$$\mathbf{\Omega_s} \cdot \nabla\, \mathbf{I}(\mathbf{r},\mathbf{\Omega_s}) = -\kappa(\mathbf{r})\Big[\mathbf{I}(\mathbf{r},\mathbf{\Omega_s}) - \mathbf{S}(\mathbf{r},\mathbf{\Omega})\Big]. \tag{2.49}$$

Here $\mathbf{I}(\mathbf{r},\mathbf{\Omega_s})$ represents the total radiance vector of (I,Q,U,V) Stokes parameters in direction $\mathbf{\Omega_s}$ at point $\mathbf{r}$. $\mathbf{S}(\mathbf{r},\mathbf{\Omega})$ the source function and $\kappa(\mathbf{r})$ the global extinction coefficient. The choice of an appropriate geometry, the inclusion of polarization (as stated by the inclusion of the Mueller matrix) as well as developing a numerical solution for Eq.(2.49) will be the main task of this work. Special emphasis will be payed to polarization treatment in plane–parallel geometry and its extension to multi–dimensional spherical atmospheres.

Chapter 3

Multi–dimensional polarized radiative transfer

Two assumptions are usually made in the study of radiative transfer in planetary atmospheres: (a) that the atmosphere consists of plane–parallel layers and (b) that these layers are illuminated by parallel solar radiation over their entire extend. This assumptions are valid however for those portions of the atmosphere for which the Sun is sufficiently hight above the horizon. If the Sun is close to the horizon or below the horizon, it is necessary to take the spherical nature of the atmosphere into account. Therefore, a multi–dimensional treatment for radiation transport is necessary. We first introduce the general mathematical framework for general curvilinear coordinates and then reduce the problem to the spherical geometry reference system. Under this assumption we are able to treat the problem of light scattering in spherical planetary atmospheres.

3.1 Radiative transfer in curvilinear coordinates

An analytical or numerical solution of the radiative transfer equation Eq.(2.49) is only possible if a coordinate system is specified. The choice of the coordinate system depends on the medium curvature, the medium and the radiation field symmetry and eventually several other conditions (Jones & Bayazittoglu 1992). In any coordinate system each point $\mathbf{r}$ is defined by three position coordinates (x_1, x_2, x_3) and each direction $\mathbf{\Omega_s}$ by two polar angles θ and ϕ in the local coordinate system. Thus, the intensity in Eq.(2.49) is a function of five variables. We notice that one fixed direction $\mathbf{\Omega_s}$ will be seen under varying angles at different locations if the orientation of the local system varies with position. In that case, θ and ϕ depend on he position coordinates of point $\mathbf{r}$ (Vaillon et al. 1996).

The general expression for the path–length derivative part of the radiative transfer equation (2.49) along any arbitrary direction $\mathbf{\Omega_s}$ is,

$$\frac{d}{ds} = \mathbf{\Omega_s} \cdot \nabla. \tag{3.1}$$

The following analysis is adopted from Vaillon et al. (1996).

In curvilinear coordinates the basis vector rotate with respect to a straight–line path determined by the fixed propagation vector $\mathbf{\Omega_s}$. Therefore we must allow for changes in the components of vector $\mathbf{\Omega_s}$ measured relative to the basis vector ∇_n . Thus,

$$\frac{d}{ds} \rightarrow \mathbf{\Omega_s} \cdot \nabla + \left(\frac{d\mathbf{\Omega_s}}{ds} \right) \cdot \nabla_n. \tag{3.2}$$

The nabla operator ∇ and the unit vector $\mathbf{\Omega_s}$ are written in orthogonal curvilinear coordinates as follows:

$$\nabla = \sum_{i=1}^{3} \frac{1}{h_i} \mathbf{\Omega_i} \frac{\partial}{\partial x_i}, \tag{3.3}$$

and

$$\mathbf{\Omega_s} = \sum_{i=1}^{3} \xi_i \mathbf{\Omega}_i, \tag{3.4}$$

where $\mathbf{\Omega_i}$ are unit vectors tangential to the coordinate lines x_i, ξ_i are the direction cosines of the unit vector $\mathbf{\Omega_s}$ in the selected curvilinear coordinate system and h_i are metric coefficients given by

$$h_i = \sqrt{(\frac{\partial x}{\partial x_i})^2 + (\frac{\partial y}{\partial x_i})^2 + (\frac{\partial z}{\partial x_i})^2}. \tag{3.5}$$

Here x, y, and z are the associated Cartesian coordinates. Thus, Eq.(3.2) for the path–length derivative along an arbitrary direction $\mathbf{\Omega}_s$ in orthogonal curvilinear coordinates is written as follows:

$$\frac{d}{ds} = \sum_{i=1}^{3} \frac{\xi_i}{h_i} \frac{\partial}{\partial x_i}. \tag{3.6}$$

Taking into account that the intensity is a function of five variables, we write

$$\mathbf{I} = \mathbf{I}(x_1, x_2, x_3, \theta(x_1, x_2, x_3), \phi(x_1, x_2, x_3)), \tag{3.7}$$

each derivative in Eq. (3.6) may be split into

$$\frac{\partial}{\partial x_i} \equiv \frac{\partial}{\partial x_i^p} + \frac{\partial \theta}{\partial x_i} \frac{\partial}{\partial \theta} + \frac{\partial \phi}{\partial x_i} \frac{\partial}{\partial \phi}, \tag{3.8}$$

where superscript p denotes a variation of x_i at θ and ϕ constant. As a consequence, by rewriting Eq.(3.6), the following general expression for the path-length derivative of the intensity $\mathbf{I}$ in an orthogonal curvilinear coordinate can be obtained:

$$\frac{d\mathbf{I}}{ds} = \sum_{i=1}^{3} \frac{\xi_i}{h_i} \frac{\partial \mathbf{I}}{\partial x_i} + \sum_{i=1}^{3} \frac{\xi_i}{h_i} \left(\frac{\partial \theta}{\partial x_i} \frac{\partial \mathbf{I}}{\partial \theta} + \frac{\partial \phi}{\partial x_i} \frac{\partial \mathbf{I}}{\partial \phi} \right). \tag{3.9}$$

The second two terms in Eq.(3.9) are commonly referred to as the angular redistribution terms.

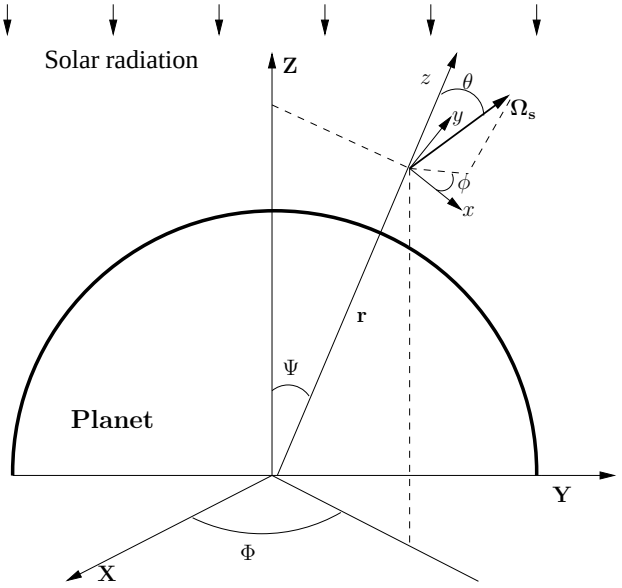

FIGURE 3.1: Definition of spherical coordinate system.

3.2 Radiative transfer in spherical coordinates

In most of the available literature on radiative transfer for spherical atmospheres a spherical body–centred coordinate system is used as the most natural and suitable coordinate system (Sobolev 1975, Sen & Wilson 1990). Such a coordinate system is pictured in Fig. (3.1). In this coordinate system each point **r** is defined by the coordinates $x_1 = \Psi$, $x_2 = \Phi$ and $x_3 = r$ in the global (spatial) coordinate system (**XYZ**) and each direction $\mathbf{\Omega_s}$ is defined by the angles θ and ϕ in the local (directional) coordinate system (**xyz**). In spherical geometry the direction cosines of the unit vector $\mathbf{\Omega_s}$ in the directional coordinate system are given by

$$\xi_\Psi \equiv \eta \equiv \sin\theta\cos\phi, \tag{3.10}$$

$$\xi_\Phi \equiv \xi \equiv \sin\theta\sin\phi, \tag{3.11}$$

$$\xi_r \equiv \zeta \equiv \cos\theta. \tag{3.12}$$

As described in Rozanov et al. (2001) (from whom the notation was adopted) if the direction cosines of the unit vector $\mathbf{\Omega_s}$ in the global coordinate system (η_0, ξ_0, ζ_0) are known the local direction cosines can then be obtained as follows:

$$\eta = \cos\Psi\cos\Phi\ \eta_0 + \cos\Psi\sin\Phi\ \xi_0 - \sin\Psi\ \zeta_0, \tag{3.13}$$

$$\xi = -\sin\Phi\ \eta_0 + \cos\Phi\ \xi_0, \tag{3.14}$$

$$\zeta = \sin\Psi\cos\Phi\ \eta_0 + \sin\Psi\sin\Phi\ \xi_0 + \cos\Psi\ \zeta_0. \tag{3.15}$$

The derivatives of the local coordinates (θ, ϕ) with respect to the global coordinates x_i in Eq.(3.9) i.e., $\partial\theta/\partial x_i$ and $\partial\phi/\partial x_i$ can be obtained by partial differentiation of Eqs.(3.13)–(3.15) with respect to global coordinates Ψ and Φ. Starting with Ψ we obtain,

$$\frac{\partial \eta}{\partial \Psi} = -\sin\Psi\cos\Phi\eta_0 - \sin\Psi\sin\Phi\xi_0 - \cos\Psi\zeta_0, \tag{3.16}$$

$$\frac{\partial \zeta}{\partial \Psi} = \cos\Psi\cos\Phi\eta_0 + \cos\Psi\sin\Phi\xi_0 - \sin\Psi\zeta_0. \tag{3.17}$$

Here we have taken into account the fact that the direction cosines η_0, ξ_0 and ζ_0 do not depend on spatial coordinates. Comparing Eqs.(3.13) and (3.17) with Eqs.(3.15) and (3.16) respectively and taking into account Eqs.(3.10) and (3.12) yields,

$$\frac{\partial \eta}{\partial \Psi} = -\zeta = -\cos\theta, \tag{3.18}$$

$$\frac{\partial \zeta}{\partial \Psi} = \eta = \sin\theta\cos\phi, \tag{3.19}$$

further, if we differentiate Eq.(3.10) and Eq.(3.12) with respect to Ψ we obtain,

$$\frac{\partial \eta}{\partial \Psi} = \cos\theta\cos\phi\frac{\partial \theta}{\partial \psi} - \sin\theta\sin\phi\frac{\partial \phi}{\partial \psi}, \tag{3.20}$$

$$\frac{\partial \zeta}{\partial \Psi} = -\sin\theta\frac{\partial \theta}{\partial \psi}. \tag{3.21}$$

Comparing Eq.(3.18) with Eq.(3.20) and Eq.(3.19) with Eq.(3.21) we finally obtain,

$$\frac{\partial \theta}{\partial \psi} = -\cos\phi, \tag{3.22}$$

$$\frac{\partial \phi}{\partial \psi} = \frac{\cos\theta\sin\phi}{\sin\theta}. \tag{3.23}$$

Following the same procedure as before we can obtain the partial derivatives of (θ, ϕ) with respect to Φ i.e.,

$$\frac{\partial \theta}{\partial \Phi} = -\sin\phi\sin\Psi, \tag{3.24}$$

$$\frac{\partial \phi}{\partial \Phi} = \frac{-\cos\theta\sin\phi\sin\Psi + \sin\theta\cos\Psi}{\sin\theta}. \tag{3.25}$$

Notice here that we have not derivated (θ, ϕ) with respect to r since the local angles do not vary along the radial direction i.e.,

$$\frac{\partial \theta}{\partial r} = 0 \qquad \text{and} \qquad \frac{\partial \phi}{\partial r} = 0. \tag{3.26}$$

The transformation between spherical coordinates to Cartesian coordinates can be expressed by

$$X = r\sin\Psi\cos\Phi, \tag{3.27}$$
$$Y = r\sin\Psi\sin\Phi, \tag{3.28}$$
$$Z = r\cos\Psi. \tag{3.29}$$

Therefore, using Eq. (3.5) the metric coefficients can be readily obtained,

$$h_r = \sqrt{(\sin\Psi\cos\Phi)^2+(\sin\Psi\sin\Phi)^2+(\cos\Psi)^2} = 1, \tag{3.30}$$
$$h_\Psi = \sqrt{(r\cos\Psi\cos\Phi)^2+(r\cos\Psi\sin\Phi)^2+(-r\sin\Psi)^2} = r, \tag{3.31}$$
$$h_\Phi = \sqrt{(-r\sin\Psi\sin\Phi)^2+(r\sin\Psi\cos\Phi)^2} = r\sin\Psi. \tag{3.32}$$

Substituting Eqs.(3.10)–(3.12), (3.20), (3.21), (3.22), (3.23) and (3.30)–(3.32) into Eq.(3.9), we obtain the full expression for the path–length derivative of the polarized radiation intensity in spherical coordinates,

$$\begin{aligned}\frac{d}{ds} = {} & \cos\theta\frac{\partial}{\partial r}+\frac{\sin\theta\cos\phi}{r}\frac{\partial}{\partial\Psi}+\frac{\sin\theta\sin\phi}{r\sin\Psi}\frac{\partial}{\partial\Phi}+\frac{\sin\theta\cos\phi}{r}(-\cos\phi)\frac{\partial}{\partial\theta}+\\ & \frac{\sin\theta\cos\phi}{r}\frac{\cos\theta\sin\phi}{\sin\theta}\frac{\partial}{\partial\phi}+\frac{\sin\theta\sin\phi}{r\sin\Psi}(-\sin\phi\sin\Psi)\frac{\partial}{\partial\theta}+\\ & \frac{\sin\theta\sin\phi}{r\sin\Psi}\left(-\frac{\cos\theta\cos\phi\sin\Psi+\sin\theta\cos\Psi}{\sin\theta}\right)\frac{\partial}{\partial\phi}.\end{aligned} \tag{3.33}$$

Finally the general form of the polarized radiative transfer equation in spherical coordinates is given by

$$\begin{aligned}\Bigg(\cos\theta\frac{\partial}{\partial r}+\frac{\sin\theta\cos\phi}{r}\frac{\partial}{\partial\Psi}+\frac{\sin\theta\sin\phi}{r\sin\Psi}\frac{\partial}{\partial\Phi}\\ -\frac{\sin\theta}{r}\frac{\partial}{\partial\theta}-\frac{\sin\theta\cos\phi\cot\Psi}{r}\frac{\partial}{\partial\phi}\Bigg)\mathbf{I}_{\rm dif} = -\kappa\left(\mathbf{I}_{\rm dif}-\mathbf{S}\right),\end{aligned} \tag{3.34}$$

where,

$$\begin{aligned}\mathbf{I}_{\rm dif} &= \mathbf{I}_{\rm dif}(r,\Psi,\Phi,\theta,\phi),\\ \mathbf{S} &= \mathbf{S}_{\rm ss}(r,\Psi,\Phi,\theta,\phi)+\mathbf{S}_{\rm ms}(r,\Psi,\Phi,\theta,\phi),\\ \kappa &= \kappa(r,\Psi,\Phi).\end{aligned}$$

In the spherical coordinate system, the multiple scattering source function and the single scattering source function from Eq. (2.42) and Eq.(2.43) can now be expressed as,

$$\mathbf{S}_{\rm ms}(r,\Psi,\Phi,\theta,\phi)=\frac{\varpi(r,\Psi,\Phi)}{4\pi}\int_0^{2\pi}d\hat{\phi}\int_0^{\pi}\mathbb{M}(r,\Psi,\Phi,\gamma)\mathbf{I}_{\rm dif}(r,\Psi,\Phi,\hat{\theta},\hat{\phi})\sin\hat{\theta}d\hat{\theta}, \tag{3.35}$$

and

$$\mathbf{S}_{\rm ss}(r,\Psi,\Phi,\theta,\phi)=\frac{\varpi(r,\Psi,\Phi)}{4\pi}F_0\mathbb{M}(r,\Psi,\Phi,\gamma_0)e^{\left(-\int_0^s\kappa(\hat{s})d\hat{s}\right)}\begin{pmatrix}1\\0\\0\\0\end{pmatrix}. \tag{3.36}$$

The scattering angles γ and γ_0 are defined by Sobolev (1975) as

$$\gamma=f(\theta,\phi;\hat{\theta},\hat{\phi})=\cos\theta\cos\hat{\theta}+\sin\theta\sin\hat{\theta}\cos(\phi-\hat{\phi}), \tag{3.37}$$

and

$$\gamma_0=f(\Psi;\theta,\phi)=-\cos\theta\cos\Psi+\sin\theta\sin\Psi\cos\phi, \tag{3.38}$$

respectively. The integration in Eq.(3.36) is performed along the direct solar beam path starting from the top of the atmosphere with s denoting the beam path–length.

3.3 Spherical atmospheres: Special cases

If the atmospheric medium has some symmetries then the differential operator (Eq. 3.33) can be simplified substantially. Lets assume that the intensity field do not depend of the global azimuth angle Φ (spherical shell medium). The third term of Eq.(3.34) containing $\partial/\partial\Phi$ vanishes and Eq.(3.34) leads to the following form of the differential radiative transfer equation,

$$\begin{aligned}[\cos\theta\frac{\partial}{\partial r}+\frac{\sin\theta\cos\phi}{r}\frac{\partial}{\partial\Psi}-\frac{\sin\theta}{r}\frac{\partial}{\partial\theta}&\\ -\frac{\sin\theta\cos\phi\cot\Psi}{r}\frac{\partial}{\partial\phi}]\mathbf{I}_{\rm dif}&=-\kappa\left(\mathbf{I}_{\rm dif}-\mathbf{S}\right).\end{aligned} \tag{3.39}$$

This form of the radiative transfer equation is discussed in Sen & Wilson (1990).

Considering each spherical shell layer to be horizontal and homogeneously illuminated by the direct solar radiance i.e., the intensity of the direct solar radiation given by Eq.(2.39) is independent of the position of point $\mathbf{r}$ with respect to the Sun. Mathematically speaking, $I_{\rm dir}(\mathbf{r},\mathbf{\Omega_s})=I_{\rm dir}(r,\mathbf{\Omega_s})$ and derivative $\partial/\partial\Psi=0$, then the following form of the spherical operator takes place,

$$\frac{d}{ds}=\cos\theta\frac{\partial}{\partial r}-\frac{\sin\theta}{r}\frac{\partial}{\partial\theta}-\frac{\sin\theta\cos\phi\cot\Psi}{r}\frac{\partial}{\partial\phi}. \tag{3.40}$$

The radiative transfer equation employing this approximate differential operator has been used by Balluch (1996) to calculate photolysis rates and solar heating in a spherical

planetary atmosphere. If an atmosphere is isotropically illuminated the diffuse radiation field becomes azimuthally independent and the following approximation for the differential operator is obtained,

$$\frac{d}{ds} = \cos\theta \frac{\partial}{\partial r} - \frac{\sin\theta}{r} \frac{\partial}{\partial \theta}. \tag{3.41}$$

In this case the radiance is a function of two variables only r and θ. This form of the radiative transfer equation Eq.(3.41) was used to solve the radiative transfer problem in stellar atmospheres as well as neutron transport and heat transfer problems (Sen & Wilson 1990).

In this thesis, we consider the full radiative transfer equation as given by Eq.(3.34). Therefore, a first–order partial differential equation for the full Stokes vector $\mathbf{I}$ as a function of five variables r, Ψ, Φ, θ and ϕ has to be solved numerically. Chapter (4) discusses a solution method for the plane–parallel problem and chapter (5) discusses the full spherical problem and presents a method for solving the radiation problem for a spherical planetary atmosphere.

Chapter 4

Polarized radiation in plane–parallel atmospheres

In this section we present a computational method for computing polarized radiation in vertically inhomogeneous atmospheres. We consider not only the well–known case of illumination by a uni–directional solar beam at the top of the atmosphere but also illumination by isotropically radiating internal sources and illumination by an isotropically radiating surface below the atmosphere. Our computational method uses an extension of a scheme based on the doubling & adding algorithm for polarized radiation. This extension includes a spherical treatment for the direct solar beam generating effectively a pseudo–spherical solution. Our numerical scheme is checked against a closely related existing method for all relevant Stokes parameters. Comparison results for the pseudo–spherical solution is also presented using a prescribed Titan atmosphere.

4.1 The plane–parallel problem

A substantial simplification of the radiative transfer equation (Eq.2.49) can be achieved by considering an atmosphere consisting of plane–parallel layers (plane–parallel atmosphere) instead of a spherical atmosphere. The simplest way to obtain a solution to the radiative transfer equation is for plane–parallel geometry, see for example Hansen & Travis (1974), Chandrasekhar (1965), Sobolev (1975), Lenoble (1985). In such models, the spatial position of a point in the atmosphere is defined only by one coordinate, its altitude; whereas in three–dimensional plane–parallel radiative transfer models (Evans 1998), the position of a point in the atmosphere is commonly defined by three coordinates, usually Cartesian coordinates. The coordinates which are commonly used in a plane–parallel atmosphere are shown in Fig.(4.1). The z–axis points upwards and z–coordinate corresponds to altitude h, $z_0 = R_p$ refers to the bottom of the atmosphere, hence $z = R_p + h$ where R_p is the radius of the planet. The x–axis is commonly selected to set the azimuth angle of the direct solar beam to zero i.e., $\phi_0 = 0$. Since the variables θ and ϕ in a plane–parallel atmosphere do not depend on the position in the atmosphere, the angular

redistribution terms in Eq.(3.9) disappear. Thus, the following expression for the path–length derivative of diffuse radiation in a plane–parallel atmosphere is obtained (when the Cartesian coordinates are used):

$$\frac{d\mathbf{I}_{\rm dif}}{ds} = \sin\theta\cos\phi\frac{\partial\mathbf{I}_{\rm dif}}{\partial x} + \sin\theta\sin\phi\frac{\partial\mathbf{I}_{\rm dif}}{\partial y} + \cos\theta\frac{\partial\mathbf{I}_{\rm dif}}{\partial z}. \tag{4.1}$$

Considering a horizontally homogeneous atmosphere all atmospheric characteristics and therefore, the intensity and sources of diffuse radiation become independent of position inside the atmosphere. This leads to a simplification of Eq.(2.45) and Eq.(2.49) for the plane–parallel case. Therefore, for this geometry the following form of the radiative transfer equation is suitable,

$$\cos\theta\frac{d\mathbf{I}_{\rm dif}(z,\theta,\phi)}{dz} = -\kappa(z)\left[\mathbf{I}_{\rm dif}(z,\theta,\phi) - \mathbf{S}_{\rm ms}(z,\theta,\phi) - \mathbf{S}_{\rm ss}(z,\theta,\phi)\right]. \tag{4.2}$$

Here, the multiple scattering source function, $\mathbf{S}_{\rm ms}$ and the single scattering source function $\mathbf{S}_{\rm ss}$ are given by

$$\mathbf{S}_{\rm ms}(z,\theta,\phi) = \frac{\varpi(z)}{4\pi}\int_0^{2\pi}\int_0^{\pi}\mathbb{M}(z,\theta,\phi;\tilde{\theta},\tilde{\phi})\,\mathbf{I}_{\rm dif}(\theta,\phi;\tilde{\theta},\tilde{\phi})\,d\tilde{\theta}\,d\tilde{\phi}\,\sin\tilde{\theta}, \tag{4.3}$$

and

$$\mathbf{S}_{\rm ss}(z,\theta,\phi) = \frac{\varpi(z)}{4\pi}F_0\mathbb{M}(z,\theta,\phi;\theta_0,\phi_0)e^{-\tau(\hat{z})/\cos\theta_0}\begin{pmatrix}1\\0\\0\\0\end{pmatrix}, \tag{4.4}$$

respectively. Here, z_t refers to the top of the atmosphere, (θ_0,ϕ_0) is the direction of the collimated solar beam and $\tau(\hat{z})$ is the optical depth defined as,

$$\tau(\hat{z}) = \int_0^{z_t}\kappa(\hat{z})d\hat{z}. \tag{4.5}$$

4.2 The plane–parallel model

In this section, we give a description of the method used to compute the internal polarized radiation field for a plane–parallel scattering atmosphere. The plane–parallel solution is sufficient to cover most applications for light scattering in planetary atmospheres, except when the Sun or the viewing direction is close or below the horizon.

To compute polarized radiation in a plane–parallel scattering atmosphere, we have used the well known and widely used doubling & adding algorithm. We have adopted the standard doubling & adding scheme as described in Lenoble (1985), Goody & Yung (1989), Evans & Stephens (1991). A description of the method is as follows: The polarization and angular aspects of the radiance field are expressed vectorialy and the scattering source integral in the radiative transfer equation is represented by matrix multiplication. The matrix differential equation is then integrated with the doubling & adding method

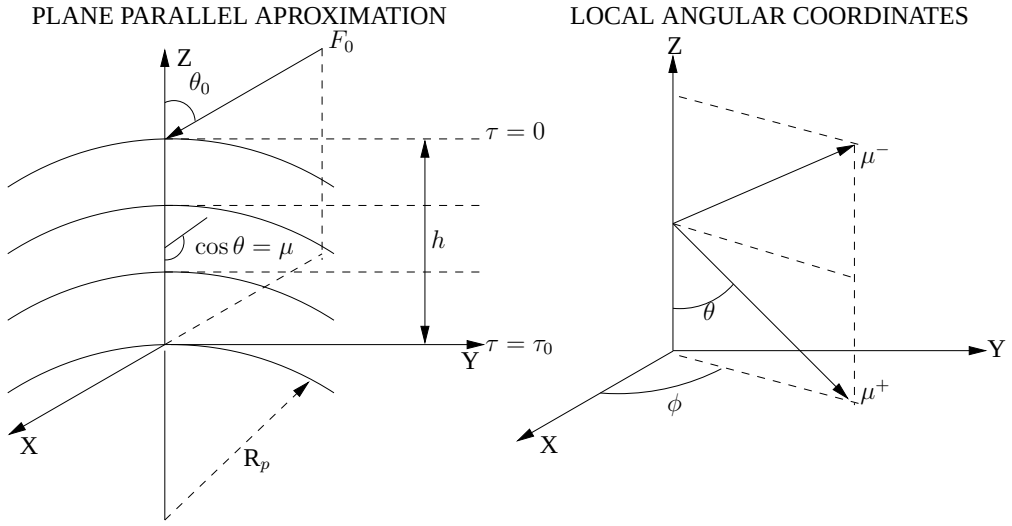

FIGURE 4.1: Geometry of the plane–parallel approximation and local angular reference frame.

starting from infinitesimal layers. Since this formulation applies to the radiative properties of the medium (via the *interaction principle*, see next section) rather than to the radiation itself, the boundary conditions are then easily incorporated afterwards and apart from the integration. The scattering is assumed to be coherent in the sense that no change of frequency occurs (thus Raman scattering is excluded). Our implementation incorporates the polarized phase matrix input in two forms: as Legendre series expansion or as generalized spherical functions. Single scattering initialization functions were adapted from Goody & Yung (1989) analytical functions. Furthermore a spherical treatment for the direct solar beam was developed and included into the model rendering effectively a pseudo–spherical solution.

Following, the standard formulation (Lenoble 1985) the monochromatic plane–parallel polarized radiative transfer equation for randomly–oriented particles is written as,

$$\mu \frac{d\mathbf{I}(\tau,\mu,\phi)}{d\tau} = -\mathbf{I}(\tau,\mu,\phi) + \frac{\varpi}{4\pi}\int_0^{2\pi}\int_{-1}^{1} \mathbb{M}(\mu,\phi;\tilde{\mu},\tilde{\phi})\mathbf{I}(\tau,\mu,\phi;\tilde{\mu},\tilde{\phi})\, d\tilde{\mu}\, d\tilde{\phi} + \mathbf{S}(\tau,\mu,\phi). \tag{4.6}$$

Here **I** is the diffuse radiance field expressed as the four–vector of Stokes parameters (I,Q,U,V), $\mathbb{M}$ is the four–by–four scattering (or Mueller) matrix, **S** the Stokes vector of radiation sources, ϖ the single scattering albedo, τ the optical depth, μ the cosine of the zenith angle θ and ϕ the azimuth angle. The coordinate system is that τ increases downward and μ is positive for downward directions. The sources of diffuse radiation are unpolarized thermal emission and a "pseudo–source" of single scattered solar radiation:

$$\mathbf{S}(\mu,\phi) = (1-\varpi)B(t)\begin{pmatrix}1\\0\\0\\0\end{pmatrix} + \frac{\varpi}{4\pi}\frac{F_0}{\mu_0}\mathbb{M}(\mu,\phi;\mu_0,\phi_0)e^{(-\tau/\mu_0)}\begin{pmatrix}1\\0\\0\\0\end{pmatrix}. \tag{4.7}$$

Here $B(t)$ is the Planck blackbody function, F_0 the unpolarized solar flux at the top of the atmosphere and (μ_0, ϕ_0) is the direction of the collimated direct solar beam.

The angular variation of radiation is written as Fourier series in azimuth (Lenoble 1985) and by discretization in zenith angle using numerical quadrature (Chandrasekhar 1965). The model has two types of numerical quadrature available i.e. Gaussian and Double–Gaussian. The radiance at any position inside the atmosphere is formed by three vector components: Stokes parameters, quadrature zenith angles and Fourier azimuth modes. The radiance is separated accordingly to hemisphere with $\mathbf{I}^+$ representing downward radiance $(\mu \geq 0)$ and $\mathbf{I}^-$ representing upward radiance $(\mu \leq 0)$ (see Fig.4.1). The number of quadrature angles and azimuth modes is managed by the user depending on the desired accuracy and the number of Legendre terms representing the polarized phase matrix. The radiance field is computed via the doubling & adding algorithm.

The underlying concept behind the doubling & adding method is the *interaction principle*. This principle expresses the linear interaction of radiation with the physical medium. We introduce next the interaction principle and focus in its relation with the doubling & adding algorithm.

4.3 Interaction principle

The *interaction principle* is fully described in Goody & Yung (1989). We reproduce below an extract of this topic (adapted to our geometry) for completeness on the subject.

The integro–differential equation (Eq. 4.6) described above may be regarded as a "microscopic" approach to radiative transfer. This one–dimensional equation (Eq. 4.6) relates the radiation field at τ to that of $\tau + d\tau$ where $d\tau$ is infinitesimally small. There is however an alternative approach to radiative transfer that can be regarded as the "macroscopic" approach. The key concept is the *interaction principle*. This principle, which is a conservation principle, relates the radiation emerging from an arbritrary layer of the atmosphere to the incident fluxes on the boundary and the source distribution within the layer. If we are interested in the overall transfer properties of the layer, we can show that these two different approaches are in fact equivalent.

According to Goody & Yung (1989) in a plane–parallel atmosphere the physical properties of the atmosphere depend upon a single variable τ. At any level, we may define the upward and downward directed specific intensities $I^-(\tau)$ and $I^+(\tau)$ as above. Let's us consider a layer of optical depth τ_a bounded by surfaces $\tau = \tau_1$ and $\tau = \tau_2$ ($\tau_a = \tau_2 - \tau_1$, Fig. 4.2). The *interaction principle* states that there is a linear conservation principle that relates the radiation emerging from the layer $I^-(\tau_1)$ and $I^+(\tau_2)$ to the incident radiation $I^+(\tau_1)$ and $I^-(\tau_2)$ and to the source Σ. In mathematical terms this translates to,

$$I^-(\tau_1) = R_a I^+(\tau_1) + T_a^* I^-(\tau_2) + \Sigma_a^-, \tag{4.8}$$

$$I^+(\tau_2) = T_a I^+(\tau_1) + R_a^* I^-(\tau_2) + \Sigma_a^+, \tag{4.9}$$

where R_a and T_a are the reflection and transmission matrix operators for the downward directed incident stream of radiation, R_a^* and T_a^* are the corresponding operators for the

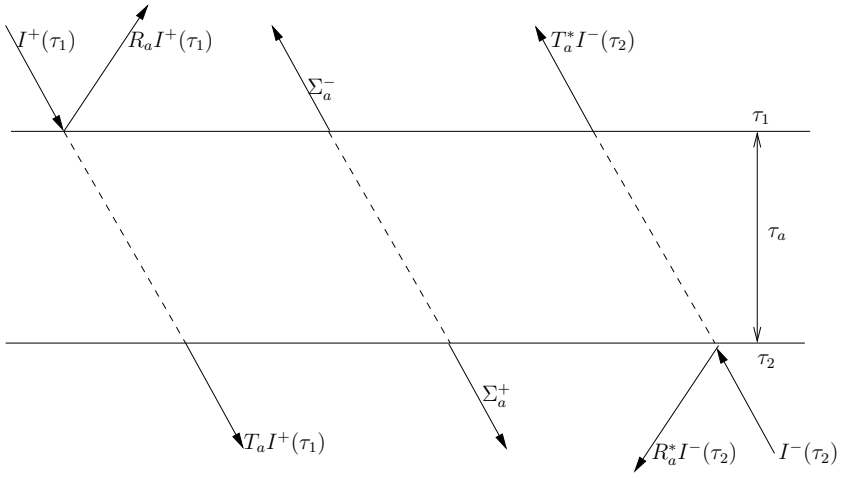

FIGURE 4.2: The interaction principle.

upward directed incident stream and $\Sigma_a^{\pm}$ represent the sources of direct and multiple scattered radiation (including internal sources if available). The discrete representation of the reflection and transmission operators remains to be specified.

In general, $R_a \neq R_a^*$ and $T_a \neq T_a^*$, then Eq.(4.8) and Eq.(4.9) can be written as,

$$\begin{vmatrix} I^-(\tau_1) \\ I^+(\tau_2) \end{vmatrix} = \mathbb{O}(a) \begin{vmatrix} I^+(\tau_1) \\ I^-(\tau_2) \end{vmatrix} + \begin{vmatrix} \Sigma_a^- \\ \Sigma_a^+ \end{vmatrix}, \tag{4.10}$$

where,

$$\mathbb{O}(a) = \begin{vmatrix} R_a & T_a^* \\ T_a & R_a^* \end{vmatrix}. \tag{4.11}$$

The linear operators $T_a,\ T_a^*$, and $R_a,\ R_a^*$ describe diffuse transmission and diffuse reflection respectively. For example, R_a can be understood as

$$R_a^* I^-(\tau_2) = \int_0^1 R(-\mu') I(\tau_2, -\mu') d\mu', \quad 0 < \mu < 1. \tag{4.12}$$

4.3.1 Adding two layers

Repeated application of the *interaction principle* enables us to find the rule for adding two layers. Fig.(4.3) shows a schematic of two adjacent layers of optical depth τ_a and τ_b respectively, bounded by the planes $\tau = \tau_1, \tau_2$ and τ_3. For the first layer the *interaction principle* gives Eq.(4.10). Then a similar relation can obtained for the second layer,

$$\begin{vmatrix} I^-(\tau_2) \\ I^+(\tau_3) \end{vmatrix} = \mathbb{O}(b) \begin{vmatrix} I^+(\tau_2) \\ I^-(\tau_3) \end{vmatrix} + \begin{vmatrix} \Sigma_b^- \\ \Sigma_b^+ \end{vmatrix}, \tag{4.13}$$

where,

$$\mathbb{O}(b) = \begin{vmatrix} R_b & T_b^* \\ T_b & R_b^* \end{vmatrix}. \tag{4.14}$$

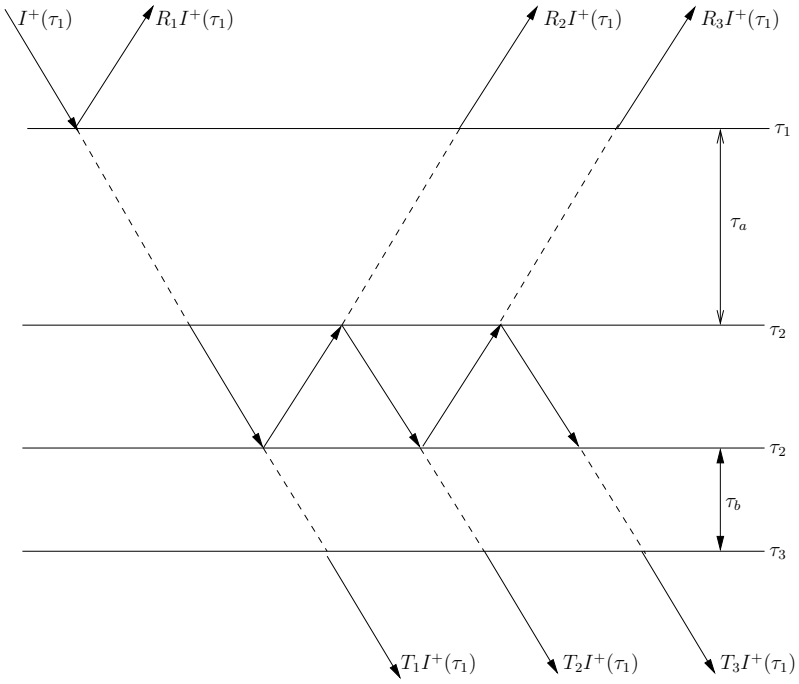

FIGURE 4.3: Combining two layers. Layers a and b can together be combined in a single layer c.

If we eliminate $I^{\pm}(\tau_2)$ from Eq.(4.10) and Eq.(4.13) we obtain a relation for a combined layer of optical depth $\tau_a + \tau_b$ i.e.,

$$\left| \begin{array}{c} I^-(\tau_1) \\ I^+(\tau_3) \end{array} \right| = \mathbb{O}(a+b) \left| \begin{array}{c} I^+(\tau_1) \\ I^-(\tau_3) \end{array} \right| + \left| \begin{array}{c} \Sigma^-_{a+b} \\ \Sigma^+_{a+b} \end{array} \right|, \tag{4.15}$$

with $\mathbb{O}(a+b)$ written as,

$$\mathbb{O}(a+b) = \left| \begin{array}{cc} R_a + T^*_a (E - R_b R^*_a)^{-1} R_b T_a & T^*_a (E - R_b R^*_a)^{-1} T^*_b \\ T_b (E - R^*_a R_b)^{-1} T_a & R_b + T_b (E - R^*_a R_b)^{-1} R^*_a T^*_b \end{array} \right|, \tag{4.16}$$

and

$$\left| \begin{array}{c} \Sigma^-_{a+b} \\ \Sigma^+_{a+b} \end{array} \right| = \left| \begin{array}{c} \Sigma^-_a \\ \Sigma^+_b \end{array} \right| + \left| \begin{array}{cc} T^*_a (E - R_b R^*_a)^{-1} R_b & T^*_a (E - R_b R^*_a)^{-1} \\ T_b (E - R^*_a R_b)^{-1} & T_b (E - R^*_a R_b)^{-1} R^*_a \end{array} \right|. \tag{4.17}$$

Here E represents the identity operator.

The *interaction principle* is completely general and we can apply it to the combined layer $\tau_c = \tau_a + \tau_b = \tau_3 - \tau_1$ to obtain,

$$\left| \begin{array}{c} I^-(\tau_1) \\ I^+(\tau_3) \end{array} \right| = \mathbb{O}(c) \left| \begin{array}{c} I^+(\tau_1) \\ I^-(\tau_3) \end{array} \right| + \left| \begin{array}{c} \Sigma^-_c \\ \Sigma^+_c \end{array} \right|, \tag{4.18}$$

where,

$$\mathbb{O}(c) = \begin{vmatrix} R_c & T_c^* \\ T_c & R_c^* \end{vmatrix}. \tag{4.19}$$

It follows that Eq.(4.15) and Eq.(4.18) must be identical that is,

$$\mathbb{O}(c) = \mathbb{O}(a+b), \tag{4.20}$$

$$\Sigma_c^{\mp} = \Sigma_{a+b}^{\mp}. \tag{4.21}$$

From Eq.(4.20) we can clearly obtain a rule for combining the reflection and transmission operators,

$$R_c = R_a + T_a^*(E - R_b R_a^*)^{-1} R_b T_a, \tag{4.22}$$

$$T_c = T_b(E - R_a^* R_b)^{-1} T_a, \tag{4.23}$$

$$R_c^* = R_b + T_b(E - R_a^* R_b)^{-1} R_a^* T_b^*, \tag{4.24}$$

$$T_c^* = T_a^*(E - R_b R_a^*)^{-1} T_b^*. \tag{4.25}$$

The physical meaning of Eqs.(4.22)–(4.25) becomes clear from Fig.(4.3). Consider the downward incident stream $I^+(\tau_1)$. The reflected stream can be written as a superposition of streams that have undergone single and multiple reflexions. By inspection we then write,

$$R_1 = R_a, \tag{4.26}$$

$$R_2 = T_a^* R_b T_a, \tag{4.27}$$

and in general,

$$R_n = T_a^*(R_b R_a^*)^{n-1} R_b T_a, \quad (n = 2, 3, ...). \tag{4.28}$$

Therefore, the total reflected intensity is,

$$\begin{aligned} I^-(\tau_1) &= \left[R_a + T_a^* \sum_{n=1}^{\infty} (R_b R_a^*)^{n-1} R_b T_a \right] I^+(\tau_1), \\ &= [R_a + T_a^*(E - R_b R_a^*)^{-1} R_b T_a] I^+(\tau_1), \\ &= R_c I^+(\tau_1). \end{aligned} \tag{4.29}$$

This explains the meaning of Eq.(4.22). Similarly, inspection of Fig.(4.3) yields,

$$T_c = \sum_{n=1}^{\infty} T_n, \tag{4.30}$$

where,

$$\begin{aligned} T_1 &= T_b T_a, \\ T_2 &= T_b R_a^* R_b T_a, \\ \ldots &= \ldots, \\ T_n &= T_b (R_a^* R_b)^{n-1} T_a \qquad (n = 3, 4, \ldots). \end{aligned} \tag{4.31}$$

Substituting Eq.(4.31) into Eq.(4.30) leads to Eq.(4.23). A straightforward extension of the above reasoning to the upward directed stream $I^-(\tau_3)$ provides a similar physical interpretation of Eq.(4.24) and Eq.(4.25).

4.3.2 Building the radiation field

We need to find out the response of a combination or addition of layers which are placed side by side. Given the operator, $\mathbb{O}(a)$ for a layer a as defined by Eq.(4.11) and $\mathbb{O}(b)$ for layer b as defined by Eq.(4.14), Eq.(4.16) states a rule for computing $\mathbb{O}(a+b)$ for the combined layer $a+b$. This simple binary composition rule may be formally defined as a *Star Product*,

$$\mathbb{O}(a+b) = \mathbb{O}(a) * \mathbb{O}(b), \tag{4.32}$$

where the order of adding the layers is important. In general, $\mathbb{O}(a+b) \neq \mathbb{O}(b+a)$ and the star multiplication is non–commutative except for the special case in which the combined layer is homogeneous. It can be shown that the star product is associative for the combination of three layers $a,\ b$ and c,

$$\mathbb{O}(a+b+c) = \mathbb{O}(a) * [\mathbb{O}(b) * \mathbb{O}(c)] = [\mathbb{O}(a) * \mathbb{O}(b)] * \mathbb{O}(c). \tag{4.33}$$

For a layer of zero optical thickness we can define,

$$\mathbb{O}(0) = \begin{pmatrix} 0 & E \\ E & 0 \end{pmatrix}. \tag{4.34}$$

It is clear from Eq.(4.16) that,

$$\mathbb{O}(0+a) = \mathbb{O}(0) * \mathbb{O}(a) = \mathbb{O}(a) * \mathbb{O}(0) = \mathbb{O}(a+0) = \mathbb{O}(a), \tag{4.35}$$

for any layer a. Here $\mathbb{O}(0)$ plays the role of the an identity operator for star multiplication.

Let A be an arbitrary collection of plane–parallel slabs, then the set of operators $\mathbb{O}(a) : a \in A$ forms a semigroup with respect to star multiplication. The essential elements of the semigroup structure are the binary superposition rule Eq.(4.32), the associative law Eq.(4.33) and the existence of an identity operator. The semigroup differs from the group in that the inverse of $\mathbb{O}(a)$ generally does not exist i.e. for and arbitrary operator $\mathbb{O}(a)$ we cannot find an $\mathbb{O}(b)$ such that,

$$\mathbb{O}(a) * \mathbb{O}(b) = \mathbb{O}(0). \tag{4.36}$$

The physical reason is obvious. In multiple scattering the entropy of radiation always increases except in the trivial case of scattering by a layer of zero optical thickness which conserves entropy. Hence, no combination of nontrivial layers can simulate the net effect of a trivial layer.

4.4 The solution method: Doubling and adding

The formulation of the *interaction principle* allows us to express the interaction of radiation with the atmospheric medium i.e. how the radiation emerging from a layer is related to the radiation incident upon the layer together with the radiation generated within the layer (Fig.4.4). As pointed out by Evans & Stephens (1991), when the layer is the whole atmosphere (including its surface) computing the reflection (R), transmission (T) and source (Σ) matrices amounts to solve the radiative transfer equation.

As we will see further on, there are three parts to the solution method: **(a)** the conversion of single–scattering information to a suitable form in order to apply the *interaction principle* (Legendre expansion of phase matrices for aerosol scattering, internal sources within layers and polarization rotation), **(b)** spatial and angular grid discretization (Fourier series expansion in azimuth, Gaussian integration in zenith) and **(c)** application of the *interaction principle* in the form of the doubling & adding algorithm with suitable boundary conditions.

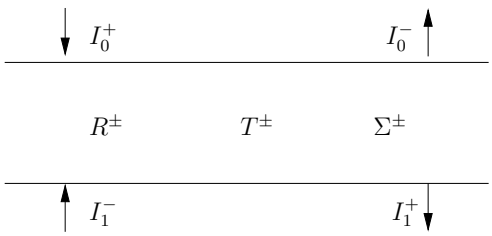

FIGURE 4.4: Reflection (R), transmission (T) and source (Σ) matrices in an atmospheric layer[1].

4.4.1 The polarized scattering matrix

The transformation of single–scattering information from a convenient input format (like Legendre series or generalized spherical functions in scattering angle) to a form suitable for a radiative transfer model is complicated because of the dependence of the Stokes parameters Q and U on a reference plane. In Eq.(4.6) $\mathbb{M}$ is the four–by–four polarized Mueller or scattering matrix for the incoming (θ, ϕ) and outgoing $(\tilde{\theta}, \tilde{\phi})$ ray directions. For unpolarized monochromatic radiation the scattering process is compleatly described by the phase function P (phase matrix $\mathbb{P}$ for polarized case) which gives the probability of photon scattering from an incoming direction. This probability is a function of the scattering angle between the incoming and outgoing direction and its natural reference

[1] In this representation, $^+$ represents downward direction and $^-$ represents upward direction.

frame is the scattering plane. However, for polarized radiation, the scattering process has its own reference frame which is the meridional plane (defined by the z–axis and the direction of travel in the local coordinate system, Fig. 4.5). Therefore a rotation of the reference frame has to be performed. The rotation from the polarized phase matrix $\mathbb{P}$ to the rotated polarized scattering matrix $\mathbb{M}$ is expressed mathematically by

$$\mathbb{M}(\theta,\phi;\tilde{\theta},\tilde{\phi}) = \overline{\mathbb{L}}_{\rm rot}(i_2-\pi)\ \mathbb{P}(\cos\Theta)\ \overline{\mathbb{L}}_{\rm rot}(i_1), \tag{4.37}$$

where,

$$\Theta = \cos(\theta)\cos(\tilde{\theta}) + \sin(\theta)\sin(\tilde{\theta})\cos(\phi-\tilde{\phi}). \tag{4.38}$$

$\overline{\mathbb{L}}_{\rm rot}$ is the polarization rotation matrix for the Stoke basis (I,Q,U,V),

$$\overline{\mathbb{L}}_{\rm rot}(i) \;=\; \begin{pmatrix} 1 & 0 & 0 & 0 \\ 0 & \cos(2i) & -\sin(2i) & 0 \\ 0 & \sin(2i) & \cos(2i) & 0 \\ 0 & 0 & 0 & 1 \end{pmatrix}. \tag{4.39}$$

The rotation angle i_1 in Fig.(4.5) is the angle between the scattering plane and the local meridional plane containing the incoming ray (θ,ϕ) and i_2 is the angle between the scattering plane and the local meridional plane containing the outgoing ray $(\tilde{\theta},\tilde{\phi})$. The scattering angle Θ is given by Eq.(4.38), the rotation angles i_1 and i_2 may be found from spherical trigonometry.

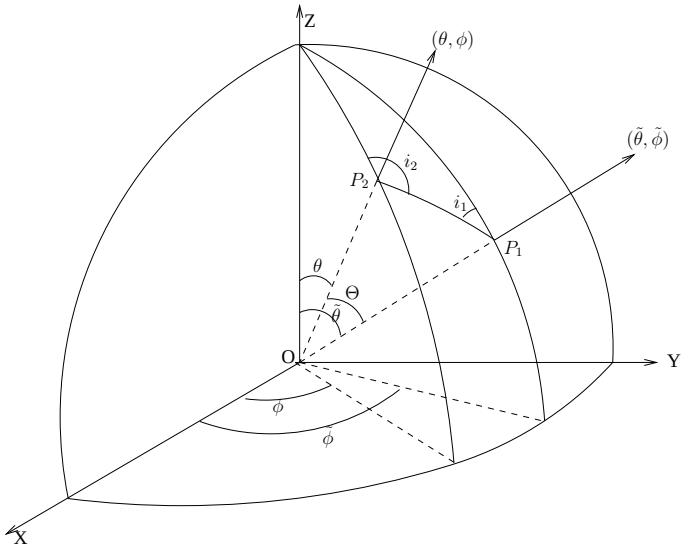

FIGURE 4.5: Polarization reference frame.

For randomly oriented particles with a plane of symmetry, the 16–element phase matrix has only the following six non–zero elements (for spheres $F_{22} = F_{11}$ and $F_{44} = F_{33}$),

$$\mathbb{P}(\cos\Theta) = \begin{pmatrix} F_{11} & F_{12} & 0 & 0 \\ F_{12} & F_{22} & 0 & 0 \\ 0 & 0 & F_{33} & F_{34} \\ 0 & 0 & -F_{34} & F_{44} \end{pmatrix}. \tag{4.40}$$

The elements of the phase matrix F_{ij} are input to the model as Legendre series of $\cos\Theta$, namely

$$F_{ij}(\cos\Theta) = \sum_{l=0}^{N_l} \chi_l^{(ij)} C_l(\cos\Theta), \tag{4.41}$$

where C_l are the normalized Legendre polynomials for argument $(\cos\Theta)$, $\chi_l^{(ij)}$ are the Legendre coefficients for entry F_{ij} and N_l the number of terms of the expansion.

As a consequence of the orthogonality of the Legendre polynomials, the $N_l + 1$ coefficients $\chi_l^{(ij)}$ may formally be obtained from,

$$\chi_l^{(ij)} = \frac{(2l+1)}{2} \int_{-1}^{1} F_{ij}(\cos\Theta) C_l(\cos\Theta) d(\cos\Theta). \tag{4.42}$$

With these definitions, the entry F_{11} of the phase matrix satisfies the normalization condition,

$$\frac{1}{2} \int_{-1}^{1} F_{11}(\cos\Theta) d(\cos\Theta) = 1. \tag{4.43}$$

4.4.2 Fourier expansion of the Stokes vector and Scattering matrix

Fourier series expansion of the Stokes vector and Scattering matrix is useful to reduce the number of variables treated at one time. The scattering matrix $\mathbb{M}$ and therefore the Stokes vector, is written in terms of the Fourier series in ϕ and $\tilde{\phi}$ at discrete quadrature angles μ_j and $\tilde{\mu}_j$ i.e.

$$\begin{aligned} \mathbb{M}(\mu_j, \phi; \mu_{\tilde{j}}, \tilde{\phi}) &= \sum_{m=0}^{M} \sum_{\tilde{m}=0}^{M} \Big[\mathbb{M}^{cc}_{m\tilde{m}} \cos(m\phi)\cos(\tilde{m}\tilde{\phi}) + \mathbb{M}^{cs}_{m\tilde{m}} \cos(m\phi)\sin(\tilde{m}\tilde{\phi}) \\ &+ \mathbb{M}^{sc}_{m\tilde{m}} \sin(m\phi)\cos(\tilde{m}\tilde{\phi}) + \mathbb{M}^{ss}_{m\tilde{m}} \sin(m\phi)\sin(\tilde{m}\tilde{\phi}) \Big], \end{aligned} \tag{4.44}$$

where ss and cc represent sine and cosine modes and sc and cs mixed modes respectively. Here, a method is needed to convert from the $\chi_l^{(i)}$ representation to the $\mathbb{M}_{m\tilde{m}}$ representation of single scattering information. In the scalar (unpolarized) radiative transfer case, this conversion is accomplished by using the addition theorem of associated Legendre functions. The rotation of the reference frame when considering polarization precludes the use of that method for finding the Fourier modes of the scattering matrix (Evans & Stephens 1991).

We use a simple method which is proposed by Evans & Stephens (1991). The method performs the polarization rotation explicitly in azimuth space and then Fourier transform the results (via a FFT) to get the scattering matrix for each Fourier azimuth mode. The method proceeds as follows: For each pair of quadrature angles $(\mu_j, \tilde{\mu}_j)$ and for a number of azimuth angle differences $\Delta\phi_k = \phi - \tilde{\phi}$, the scattering angle Θ is found and the Legendre series are summed for the unique elements of the scattering matrix. In most general cases six series must be summed, but depending in the number of Stokes parameters used and the type of scattering (Rayleigh, Mie, others) less series may be added. The scattering matrix $\mathbb{M}$ is computed for each of the evenly spaced $\Delta\phi_k$. The number of $\Delta\phi_k$ is chosen so that the highest frequency, which depends on the number of terms of the Legendre series, is completely sampled (Evans & Stephens 1991). For each pair of quadrature angles, $\mathbb{M}$ is Fourier– transformed with an FFT to find the coefficients of $\mathbb{M}^c_m$ and $\mathbb{M}^s_m$ for the Fourier series in $\tilde{\phi} - \phi$, viz.

$$\mathbb{M}^c_m + i\,\mathbb{M}^s_m = \frac{(2-\delta_{m0})}{N_\phi} \sum_{k=0}^{N_\phi - 1} e^{2\pi i/N_\phi km}\, \mathbb{M}(\mu_j, \mu_{\tilde{j}}, \Delta\phi_k). \tag{4.45}$$

Since the scattering matrix only depends on the difference in azimuth between the incoming and outgoing angles, the Fourier modes separate ($\mathbb{M}$ depends only on m, rather than m and $\tilde{m}$) and

$$\begin{aligned} \mathbb{M}^{cc}_{m\tilde{m}} &= \mathbb{M}^{ss}_{m\tilde{m}} = \mathbb{M}^c_m \delta_{m\tilde{m}}, \\ \mathbb{M}^{cs}_{m\tilde{m}} &= -\mathbb{M}^{sc}_{m\tilde{m}} = \mathbb{M}^s_m \delta_{m\tilde{m}}. \end{aligned} \tag{4.46}$$

The sine and cosine modes do mix however, for a particular m. The decoupling of azimuth modes allows the modes to be solved separately. Using Fourier decomposition, the radiative transfer equation (Eq. 4.6) is effectively decomposed into $2M + 1$ azimuthally independent differential equations for each Fourier mode i.e.

$$\mu \frac{\mathrm{d}\mathbf{I}^m(\tau,\mu)}{\mathrm{d}\tau} = -\mathbf{I}^m(\tau,\mu) + \frac{\tilde{\omega}}{4\pi} \int_{-1}^{1} \mathbb{M}^m(\mu;\tilde{\mu})\mathbf{I}^m(\tau,\mu;\tilde{\mu})\mathrm{d}\tilde{\mu} + \mathbf{S}^m(\tau,\mu). \tag{4.47}$$

This form of the radiative transfer equation is efficiently solved by applying the *interaction principle* (Sec.4.3). The integral on the right side of Eq.(4.47) is integrated numerically using Gaussian quadrature (see Sec. 4.4.3) for a discrete set of μ_j values. It is important to note that it is necessary to exactly integrate the integral on the right hand side of Eq.(4.47) so that energy is conserved. This means that for a given number of quadrature zenith angles there is a limit on the number of the Legendre series representing the scattering matrix.

A truncation scheme for the number of Legendre series according to the type of quadrature, e.g. for Gaussian quadrature was implemented. As pointed out by King (1983), Gaussian quadrature is exact for polynomials of degree less that $2G_\mu$ (G_μ is the number of quadrature angles per hemisphere). Thus, it is essential that the order of the quadrature formula exceed the number of significant Legendre terms $L_{\max}$ in the phase

function. This implies that if a large number of Legendre terms are necessary to fully describe the phase matrix then we need a very large number of Gaussian integration points G_μ to resolve the scattering pattern which in turn implies larger computational resources. To avoid this pitfall, a truncation procedure that provide accurate intensities when G_μ is kept relatively small is necessary.

We have used the simple scheme $L_{\max} = 4G_\mu - 3$ since at most, our phase matrix is described by $L_{\max} \approx 64$ Legendre terms. Still, achieving phase function normalization (Eq. 4.43) by the use of this method can be difficult for highly peaked phase functions because of the large number of quadrature angles required as it was pointed out above but other techniques e.g. the Delta–M method (Wiscombe 1977) are more appropriate for such a case. This technique has not yet been implemented in the present model.

4.4.3 The discretized angular grid

Integration of the integral over μ in Eq.(4.47) is done numerically. Gaussian quadrature is chosen as it has been proven to be superior to other quadrature integration techniques used in plane–parallel problems. In Gaussian quadrature, the discrete values of μ are determined by the roots of the Legendre polynomial of order $2G_j$. The weights w_j are always normalized such that,

$$\sum_{j=-G_j}^{G_j} w_j = 2 \tag{4.48}$$

where $j \neq 0$. The integral is replaced with a summation as follows:

$$\int_{-1}^{1} f(\mu) d\mu \longrightarrow \sum_{j=-G_j}^{G_j} f(\mu_j)\, w_j \tag{4.49}$$

In the calculation of irradiance, the integration is only performed over one hemisphere. This presents no real problem as the summation can run from 1 to G_j. However care must be taken to ensure that the sum of the weights is exactly unity. To ensure this a renormalization is performed.

G_j	$\pm\mu_j(=\cos\ \Theta)$	w_j
4	0.18343	0.36268
	0.52553	0.31370
	0.79667	0.22238
	0.96028	0.10123

TABLE 4.1: Sample pivots and weights for Gaussian quadrature of order eight

One draw back of using Gaussian quadrature is that since the pivots are prescribed they rarely corresponds to the desired user viewing angles. One way to avoid this is to add extra pivots at any desired angles. These pivots will have zero weighting associated with them as they should not influence the integration.

4.4.4 The discretized spatial grid

Discretizing the spatial grid is accomplished by dividing the model atmosphere into N_i layers. This is done by specifying N_{i+1} altitudes, not necessarily equally spaced, at which the solution will be determined. Each layer between two altitude levels or grid points are assigned a value for all relevant quantities of the model atmosphere i.e. single scattering albedo, absorption and scattering coefficients, phase functions, temperatures, gas absorption etc.

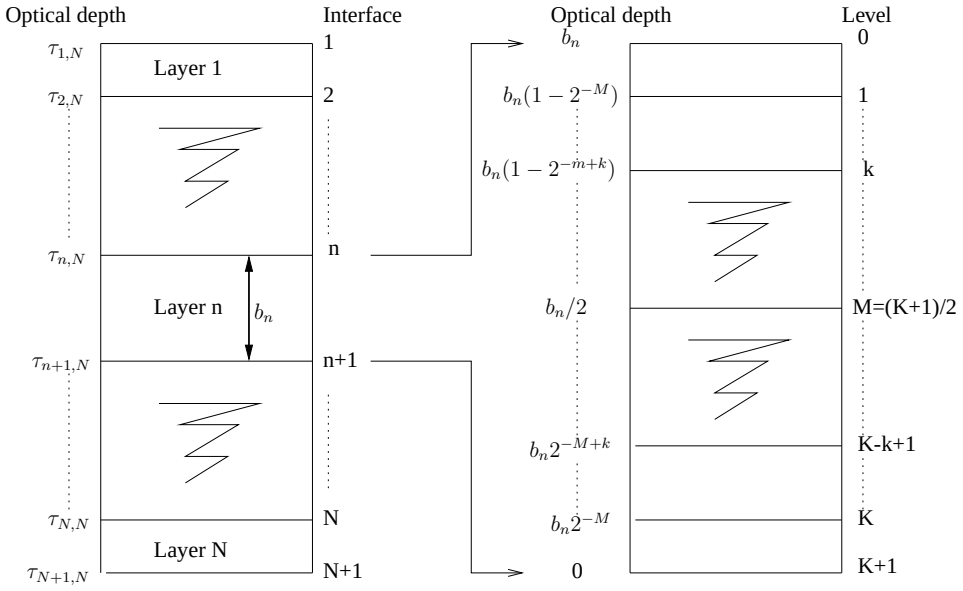

FIGURE 4.6: Schematic representation of the atmospheric layers, for a plane parallel model, indicating the optical depths and interfaces of the multi-layered atmosphere.

The optical depth at the bottom of layer n, in a multi–layered atmosphere with N layers is denoted by $\tau_{n+1,N}$ (Fig. 4.6). A homogenous layer n with optical thickness b_n has K internal levels. The bottom of the layer is denoted by $k = K + 1$, the top by $k = 0$ and the middle layer by $M = (K+1)/2$. An inhomogeneous atmosphere is simulated by the superposition of N homogenous layers with $K + 1$ thin sub–layers. The solution is found by first considering the level at the top of the atmosphere and adding layer by layer using the *interaction principle*.

4.4.5 Boundary conditions

To solve Eq.(4.6), two boundary conditions must be specified: the incident radiation at the top of the atmosphere $\mathbf{I}(0, \mu, \phi)$ and surface reflection at the bottom of the atmosphere $\mathbf{I}(\tau, -\mu, \phi)$. For near–UV to near–IR, there is no source other than direct sunlight at the top of the atmosphere so that,

$$\mathbf{I}(\tau = 0, \mu, \phi) \;=\; \mathbf{0} \;=\; [0,\; 0,\; 0,\; 0]^{\mathrm{T}}. \tag{4.50}$$

There is, in general, a source at the bottom of the atmosphere from reflection of the surface. The surface reflected Stokes vector is a function of the downward Stokes vector incident upon it. They are related via,

$$\mathbf{I}(\tau_N, -\mu, \phi) = \int_0^{2\pi} \int_0^1 \mathbf{R}(-\mu, \phi; \tilde{\mu}, \tilde{\phi}) \mathbf{I}(\tau_N, \mu, \phi; \tilde{\mu}, \tilde{\phi})\; \tilde{\mu}\; d\tilde{\mu}\; d\tilde{\phi}, \tag{4.51}$$

where, $\mathbf{R}$ is a 4×4 reflection matrix relating each reflected Stokes parameter component to each reflected component. This expression is analogous to the scattering source function vector. We must note here that $\mathbf{QRQ}$ (where $\mathbf{Q}$ is a diagonal matrix of elements $[1, 1, -1, 1]$) is used instead of only $\mathbf{R}$ to account for the change in symmetry when the surface the atmosphere is illuminated from the bottom (Hovenier 1970).

If the surface is a pure specular reflector, then the full reflection matrix can be written in terms of Fresnel equations. Generally however, it is assumed that the surface is depolarizing so that all matrix elements other than R_1 are zero. This reduces the matrix to a single element which is commonly referred as bidirectional reflectance distribution function (BDRF). A further approximation is to take, the surface reflected Stokes vector as isotropic and independent of the downward Stoke vector. In this case, the surface is said to be Lambertian and it is convenient to express the reflectivity of the surface in terms of the surface albedo ϖ_s. The surface albedo represents the fraction of energy incident on a plane surface which is reflected back to the atmosphere,

$$\varpi_s = \frac{E^{\uparrow}}{E^{\downarrow}}, \tag{4.52}$$

where $E^{\uparrow}$ and $E^{\downarrow}$ represent the upwelling and downwelling irradiance at the surface respectively. Albedo might vary with wavelength or other parameters such as solar zenith angle or wind–speed depending on the surface it represents. For a Lambertian surface, the azimuthally independent boundary conditions can be written as,

$$\mathbf{I}_m^{cs}(\tau = 0;\; \mu_j) = [0,\; 0,\; 0,\; 0]^{\mathrm{T}}, \tag{4.53}$$

$$\mathbf{I}_m^{c}(\tau_{N+1}; -\mu_j) = \begin{cases} \left[\frac{\varpi_s E^{\downarrow}(\tau_{N+1})}{\pi}, 0, 0, 0\right] & m = 0, \\ [0,\; 0,\; 0,\; 0] & m > 0, \end{cases} \tag{4.54}$$

$$\mathbf{I}_m^{s}(\tau_{N+1}; -\mu_j) = [0,\; 0,\; 0,\; 0]^{\mathrm{T}}, \tag{4.55}$$

so that only the $m = 0$ order of the Fourier expansion is non–zero which necessarily means that all odd coefficients are zero.

4.4.6 Application of the doubling and adding method

As discussed on section (4.4.2), the doubling & adding sequences are performed as matrix and vector operations on the radiance vector. The form of the radiance vector can now be made explicit since the Fourier azimuth modes are treated separately. The radiance vector consists of the Stokes parameters at the quadrature zenith angles in a hemisphere. The structure of the radiance vectors is,

$$\mathbf{I} = \begin{pmatrix} \hat{\mathbf{I}}(\mu_1) \\ \hat{\mathbf{I}}(\mu_2) \\ . \\ \hat{\mathbf{I}}(\mu_j) \\ . \\ \hat{\mathbf{I}}(\mu_N) \end{pmatrix}, \qquad \hat{\mathbf{I}}(\mu_j) = \begin{pmatrix} I^c \\ Q^c \\ U^s \\ V^s \end{pmatrix}. \tag{4.56}$$

Here the μ_j are the quadrature points of the cosine of zenith angle and the c and s subscripts refer to the cosine and sine azimuth modes. The length of the radiance vector is thus $N_{Stokes} \times N_\mu$ where N_{Stokes} represents the number of Stokes parameters used.

The scattering matrix defined before (see Sec. 4.4.1) may now be related to the local reflection and transmission matrices for an infinitesimal layer. This process is called initialization (Evans & Stephens 1991). The model described here uses analytical functions (Goody & Yung 1989) for the initialization. The elements of the reflection and transmission matrices and source vectors for the m–th azimuth mode are then,

$$\begin{aligned} |T^{\pm}|_{ij\tilde{i}\tilde{j}} &= \left[\delta_{i\tilde{i}}\delta_{j\tilde{j}} - \mathbb{F}(\Delta\tau,\mu_j)\left(\delta_{i\tilde{i}}\delta_{j\tilde{j}} - \varpi\frac{1+\delta_{0m}}{4}w_{\tilde{j}}|\mathbb{M}_m(\pm\mu_j,\pm\mu_{\tilde{j}})|_{i\tilde{i}}\right)\right], \\ |R^{\pm}|_{ij\tilde{i}\tilde{j}} &= \mathbb{F}(\Delta\tau,\mu_j)\varpi\frac{1+\delta_{0m}}{4}w_{\tilde{j}}|\mathbb{M}_m(\pm\mu_j,\pm\mu_{\tilde{j}})|_{i\tilde{i}}, \\ |\Sigma^{\pm}|_{ij} &= \mathbb{G}^{\pm}(\Delta\tau,\mu_j,\mu_0)|\mathbf{S}_m(\pm\mu_j)|_i, \end{aligned} \tag{4.57}$$

with

$$\mathbb{F}(\Delta\tau,\mu_j) = 1 - e^{-\frac{\Delta\tau}{\mu_j}}. \tag{4.58}$$

and

$$\mathbb{G}^{+}(\Delta\tau,\mu_j,\mu_0) = \begin{cases} \frac{e^{\frac{-\Delta\tau}{\mu_j}} - e^{\frac{-\Delta\tau}{\mu_0}}}{\mu_j-\mu_0} & \text{if} \quad \mu_j \neq \mu_0, \\ \frac{-\Delta\tau}{\mu_0^2}e^{\frac{-\Delta\tau}{\mu_0}} & \text{if} \quad \mu_j = \mu_0, \end{cases} \tag{4.59}$$

$$\mathbb{G}^{-}(\Delta\tau,\mu_j,\mu_0) = \frac{1-e^{\frac{1}{\mu_0}+\frac{1}{\mu_j}}}{\mu_j+\mu_0} \quad \forall\ \mu_j \tag{4.60}$$

In Eq.(4.57) i is the Stokes parameter index and j is the quadrature angle index. The barred ($\tilde{}$) indexes are the ones summed when carrying out matrix multiplication. w_j's are the integration weights corresponding to quadrature angles μ_j. The initial layer optical depth $\Delta\tau$ is chosen according to the desired accuracy (e.g. $\Delta\tau = 10^{-5}$ will give about five digits accuracy when using double precision). $\mathbf{S}_m(\mu_j)$ is the source term of the radiative transfer equation evaluated at μ_j quadrature angle for the m–th Fourier azimuth mode. The thermal radiation source term is isotropic so only the $m = 0$ term contributes.

Based on the *interaction principle* i.e Eqs.(4.8)–(4.9) the transmission, reflection and source matrices can be calculated for each individual layer. Combining them at the common interfaces (and effectively eliminating the radiances at the common interface) leads to the algorithm to combine two layers. Using the operator $\mathbb{O}$, of section (4.3.2), we compute the internal radiation field for a single homogenous layer starting with a layer of thickness $\Delta\tau$. Each step doubles the optical depth until after N steps the thickness is $2^N\Delta\tau$. The doubling method described so far requires the finite layer to be uniform as stated by Eqs. 4.57–4.60.

The doubling algorithm computes the reflection and transmission matrices and the source vectors for the homogeneous layers which are then successively combined from the top down with the adding method. The surface boundary is treated as a layer with a transmission of unity, the appropriate reflection and no source term. The radiation emitted by the surface is then the incident radiation on the lower boundary. The up–welling and down–welling radiation is then computed from the internal radiance algorithm which was derived from the *interaction principle.*

4.5 The pseudo–spherical approximation

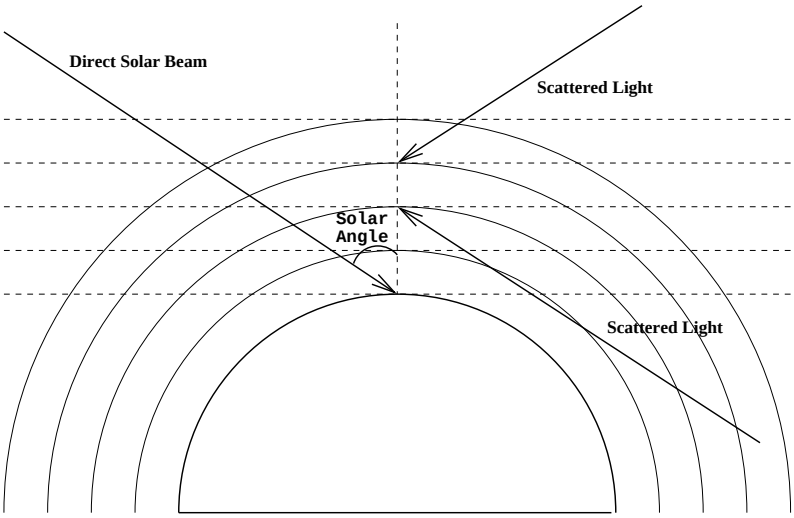

FIGURE 4.7: Schematic representation of a pseudo–spherical atmosphere.

For many applications calculation using plane–parallel geometry is adequate. However, for solar zenith angles larger than 75°, the attenuation of the direct solar beam is considerably overestimated in plane–parallel atmospheres. This is because as the μ angle tends towards zero and the plane–parallel pathlength enhancement $1/\mu$ becomes infinite (see Fig. 4.7). Also for solar zenith angles larger than 90° some parts of the atmosphere will still be illuminated, a situation which is not possible to describe using plane geometry. Similar problems arise in the calculation of scattered light near the limb or horizon.

Path–length can be both, overestimated and underestimated depending whether the streams are upward or downward. In a plane–parallel atmosphere, any viewing angle

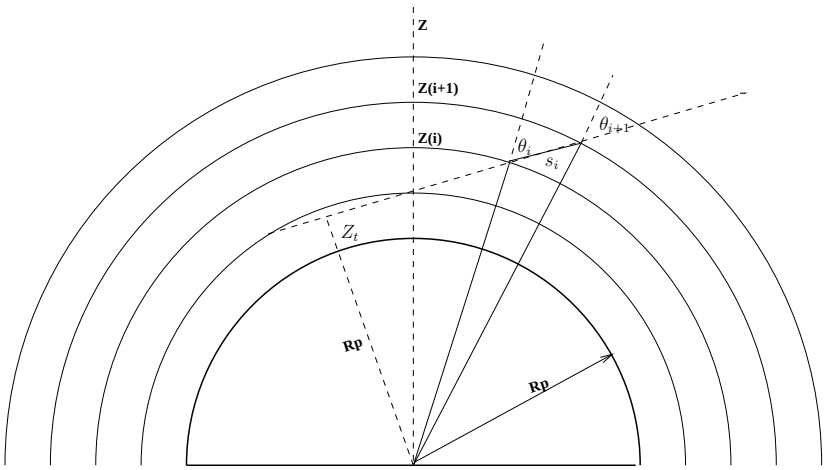

FIGURE 4.8: Path-lengths between spherical shells.

below the horizon will have a direct surface component. In a spherical atmosphere this surface component is not real for streams that do not reach the surface. To remedy this inadequacies a number of options are available, one of them being to solve the radiative transfer equation in three–dimensional spherical coordinates. As will be seen in Chapter 5 (where we implement a method to solve the radiative transfer equation for a spherical planetary atmosphere) to solve the full problem in three–dimensional spherical coordinates an initial guess solution is necessary to start an iterative scheme.

We construct this initial guess solution using a plane–parallel solution but with the inclusion of a spherical geometry correction for the direct solar beam. Thus, in a pseudo–spherical atmosphere the multiple scattering terms of Eq.(4.3) remain unchanged whereas the single scattering source term is calculated as in a spherical atmosphere i.e.,

$$\mathbf{S}_{\rm ss}(z,\theta,\phi) \;=\; \frac{\varpi}{4\pi}F_0\mathbb{M}(z,\theta,\phi;\theta_0,\phi_0)\exp\left(-\int_0^{s_t}\kappa(\hat{s})d\hat{s}\right)\begin{pmatrix}1\\0\\0\\0\end{pmatrix}. \quad (4.61)$$

Here the integration is to be performed along the direct solar beam and s_t denotes the full length of the integration line from a selected point to the top of the atmosphere along the beam. In practice Eqs.(4.3)–(4.4) are still used but using Eq.(4.61) instead of Eq.(4.4) implies that the optical depth has to be calculated as,

$$\Delta\tau_{i,i+1} = \kappa_{i,i+1}\;\; S_{i,i+1}, \quad (4.62)$$

where $S_{i,i+1}$ is the physical path–length between shell layers i and $i+1$. This is shown in Fig.(4.8) and it is calculated as follow. Consider two levels at heights z_i and z_{i+1}, the local zenith angle at height z_{i+1} is θ_{i+1} and it has a tangent height given by

$$z_{t,i+1} = (R_p + z_{i+1})\sin\theta_{i+1} - R_p, \quad (4.63)$$

where $z_{t,i+1}$ is the tangent height for the zenith angle θ_{i+1} at height z_{i+1} and R_p is the planet's radius and taken as a constant through the calculation. From this the path–length can be determined:

$$s_{i,i+1} = \left| \sqrt{(R_p + z_{i+1})^2 - (R_p + z_{t,i+1})^2} - \sqrt{(R_p + z_i)^2 - (R_p + z_{t,i+1})^2} \right|. \quad (4.64)$$

Here the absolute values ensure a positive length if $z_{i+1} > z_i$. The local zenith angle at height z_{i+1} will differ from that at z_i, they are related via,

$$\sin\theta_{i+1} = \frac{(R_p + z_i)}{(R_p + z_{i+1})} \sin\theta_i. \quad (4.65)$$

Similar to a plane–parallel atmosphere, the radiative transfer equation in a pseudo–spherical atmosphere is solved for a fixed solar zenith angle.

4.6 Numerical results

In order to verify the accuracy of our implementation, we perform some numerical runs for sample atmospheres and compare it with other similar runs done with other numerical codes. Since our implementation is based in the doubling & adding method we compare it with the freely available plane–parallel radiative transfer code (RT3) from Evans & Stephens (1991). We also include a limiting test scenario for the pseudo–spherical case. For the plane–parallel test we use relative percent differences between models i.e. $(1 - I_a/I_b) \times 100\%$ where I_a is either I, Q, U or V Stokes components generated by our model and I_b is generated by RT3. In the pseudo–spherical test, I_a is the plane–parallel solution and I_b is the pseudo–spherical solution.

4.6.1 Plane parallel tests

In this tests we compare our current pseudo–spherical model, running in plane–parallel mode, with Evans & Stephens (1991) model (RT3).

Rayleigh atmosphere

Evans & Stephens (1991) compare a Rayleigh atmosphere with the book of tables of Coulson (1959) for three cases of varying optical depth and solar angle. In this work, we run our model for a similar atmosphere and compare with the results obtained from RT3. The run was performed for a Rayleigh atmosphere as described in Evans & Stephens (1991) with optical depth $\tau = 1.0$, single scattering albedo $\varpi = 1.0$, solar flux normalized to π, cosine of solar zenith angle 0.8 and a ground albedo of 0.25. The polarized phase matrix used is shown in Fig.(4.9). The radiative transfer model was run with 8 quadrature points. Upwelling and downwelling radiance were calculated for Stokes I, Q and U at $\phi = 0, 90,$ and $180°$. Results are plotted for $\phi = 90°$ only since, U is zero at 0 and $180°$ and V is zero everywhere (see Fig. 4.9). In Fig.(4.10) we compare downwelling

radiation for the parameters specified above. Differences between both models are plotted as percentage differences for Stokes I, Q, U and V. Our model shows a very close agreement with RT3. The maximum differences are of the order of 10^{-3} % which means a full agreement of three significant digits.

Mie atmosphere

Evans & Stephens (1991) includes a Mie test case for their polarized plane parallel model. The test is done for a Mie scattering phase function for a wavelength of 0.951μm from a gamma distribution of particles with 0.2μm radius, 0.07 effective variance and index of refraction $n = 1.44$. The Legendre series coefficients were taken from Evans & Stephens (1991) and the entries of the phase matrix plotted in Fig.(4.11) for its four unique elements. In this test case, an atmosphere of $\tau = 1.0$ was used with a single scattering albedo $\varpi = 0.99$, the atmosphere is illuminated by a collimated solar beam at a solar zenith angle of $\mu_0 = 0.2(\theta_0 = 78.46^\circ)$ and solar flux $\mu_0\pi$. The ground surface is taken to be Lambertian with an albedo of 0.1. Upwelling and downwelling radiance were computed with eight Gauss–Legendre quadrature angles. The current model and Evans & Stephens (1991) computations for Stokes I, Q, U and V are plotted in Fig.(4.12) as percent differences. The plots shows an average difference between 10^{-3} % to 10^{-4} %. This translates to an agreement up to the 4–th decimal place. The maximum differences are from the lowest μ angles which is much less accurate than the other values in both Rayleigh and Mie tests. Typically, discrete– angle formulations give poorer results for lower μ. The sources of error in this comparison are the approximation inherent in the angular discretization scheme we have used.

In our tests, we have observed that Mie atmospheres seems to have slightly better agreement than Rayleigh. This is due to the fact that, in Mie atmospheres, the energy is distributed over a greater number of Fourier harmonics frequencies.

4.6.2 Pseudo–spherical tests

Mie test

In this section, we run our code in two modes: plane–parallel and pseudo–spherical for two solar angles 78° and 0° for a Mie type atmosphere as described above (sec.4.6.1). In order to setup the pseudo–spherical calculation, we have used a ratio of total atmospheric height against planet radius of $1 : 5$ (similar ratio occurs for the case of Titan's atmosphere).

We plot % differences for both geometries for the full Stokes vector. We expect some differences specially at large solar angles e.g. 78° since sphericity will play a role because the direct solar beam is calculated for this type of geometry. For a high Sun i.e. 0° we expect full agreement with the plane case since in this special case both geometries are in fact, equivalent.

The test shows a difference of about 2.5% at top of the atmosphere. The differences seen in Fig.(4.13) can be directly attributed to the sphericity of the planet. In the same plot, for low zenith angles, the differences are less marked due to the influence of multiple scattering which is calculated as in a plane–parallel atmosphere. In the second plot

Fig.(4.16) we can clearly see that for a high enough Sun the atmosphere fully behaves as it was plane–parallel therefore, both solutions, pseudo–spherical and plane–parallel should agree.

Titan atmosphere test

In this section we run our code in plane–parallel and pseudo–spherical mode for a standard Titan atmosphere as prescribed in Grieger et al. (2003) and Salinas et al. (2003). This is for the purpose only of evaluating differences between both methods. The computations where performed for an atmosphere of 500km. altitude with a planetary radius $R_p = 2575$km. under the conditions mentioned in the above papers. Fig.(4.17) shows percent differences at 450km., the highest percent differences are found for the upwelling radiances ($\mu < 0$) this difference is not bigger than 1.4%. In Fig.(4.18) we find a maximum difference of less than 2.6% for the downwelling radiances. The biggest differences are concentrated in the direction of the direct beam this is expected since the direct beam has traveled a shorter distance in a pseudo–spherical atmosphere than in a plane–parallel atmosphere.

As we have shown here, the inclusion of a spherical geometry correction for the direct solar beam shows that the spherical nature of the atmosphere has to be taken into account. Further, in a fully spherical scenario we need not only to correct for the direct solar beam but for all angular variations of the scattered radiation streams.

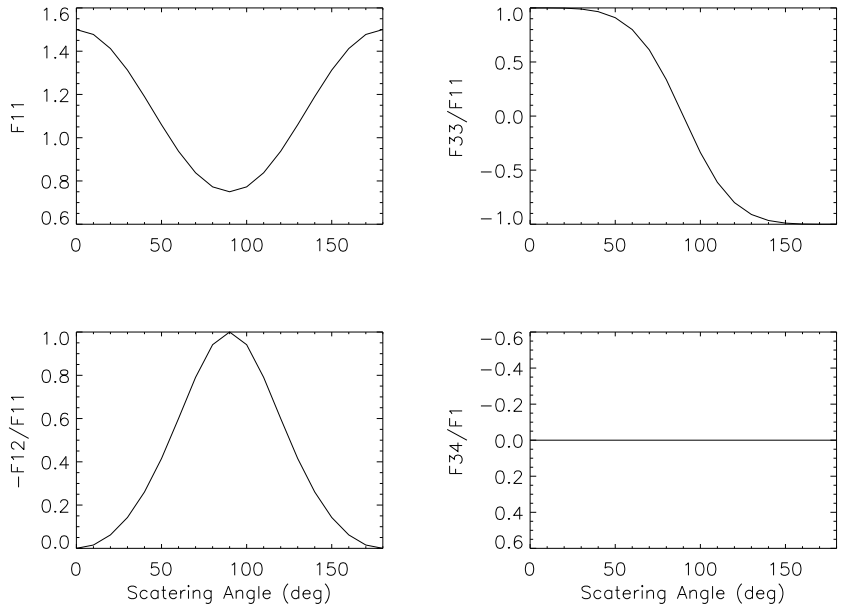

FIGURE 4.9: Rayleigh polarized phase matrix.

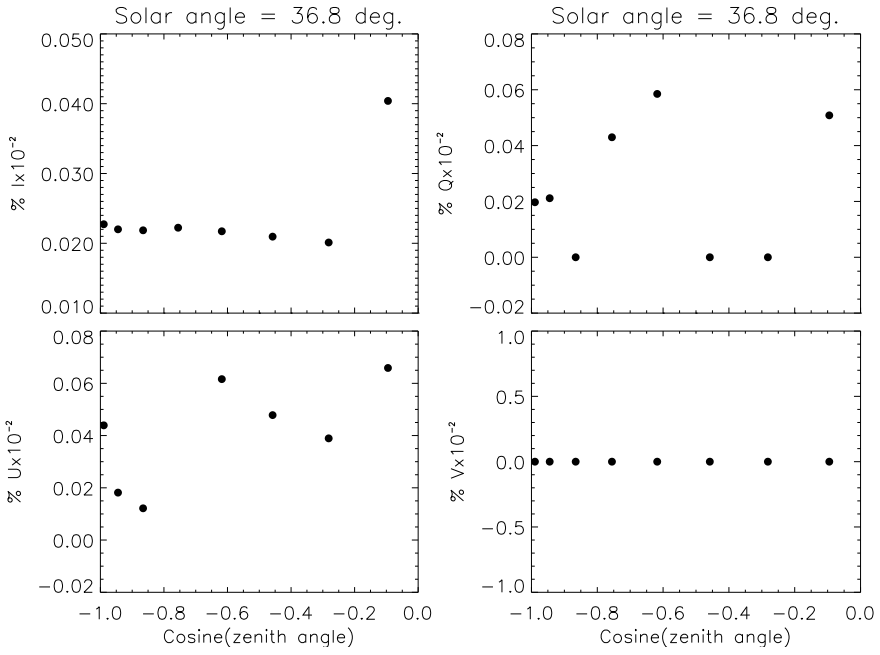

FIGURE 4.10: Stokes I, Q, U and V % difference comparison between our model and Evans & Stephens (1991) model (RT3) for a Rayleigh type atmosphere.

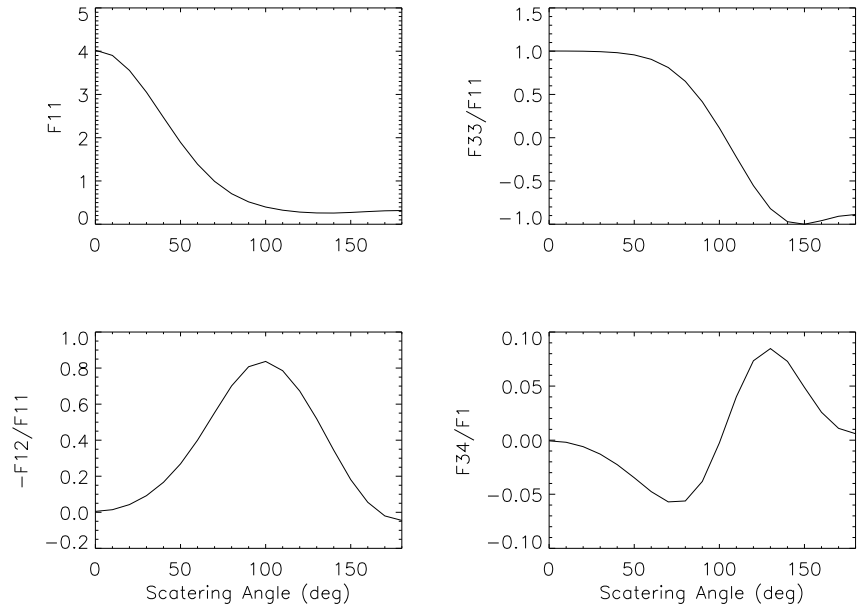

FIGURE 4.11: Polarized phase matrix for Mie type particles.

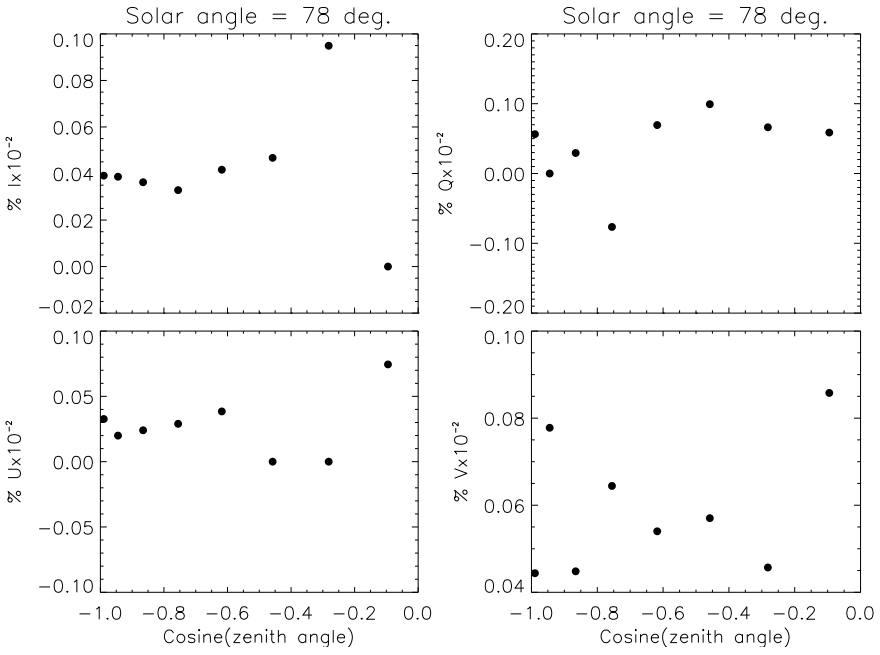

FIGURE 4.12: Stokes I, Q, U and V % difference comparison between our model and Evans & Stephens (1991) model (RT3) for a Mie type atmosphere.

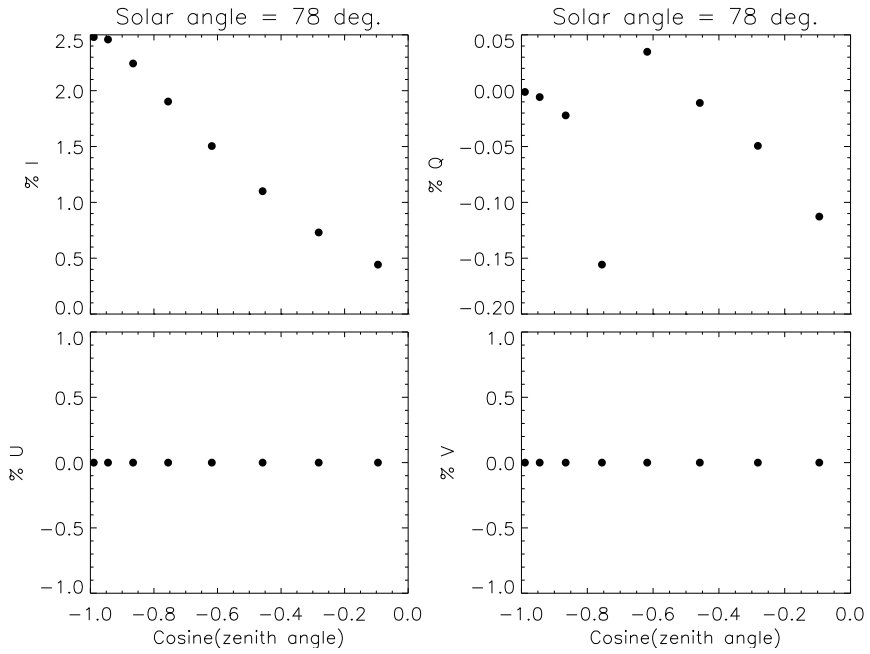

FIGURE 4.13: Pseudo–spherical vs. plane–parallel % differences for a Mie atmosphere for I, Q, U and V Stokes components, Solar angle = 78°. azimuth = 0°

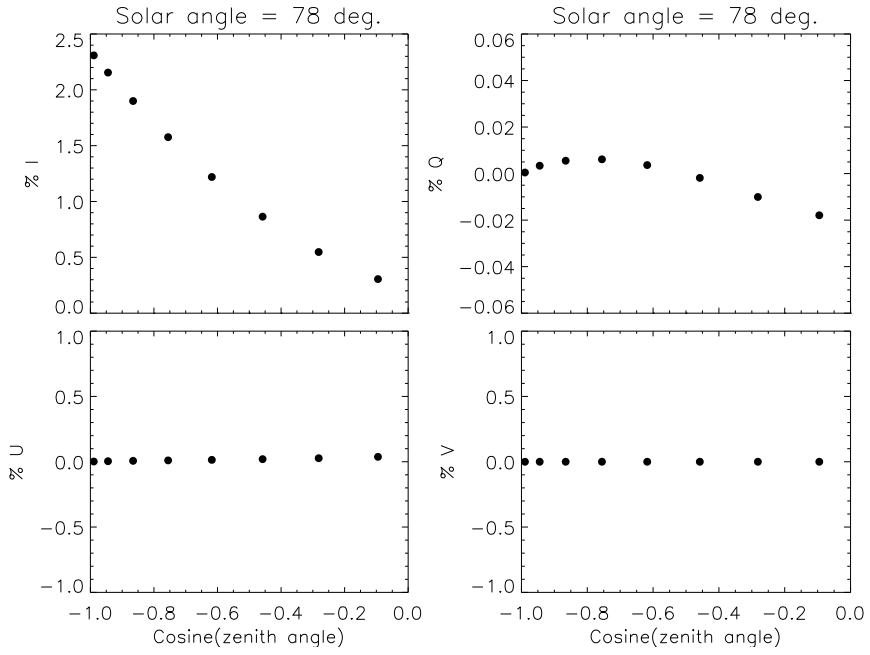

FIGURE 4.14: Pseudo–spherical vs. plane–parallel % differences for a Mie atmosphere for I, Q, U and V Stokes components, Solar angle = 78°, azimuth = 90°

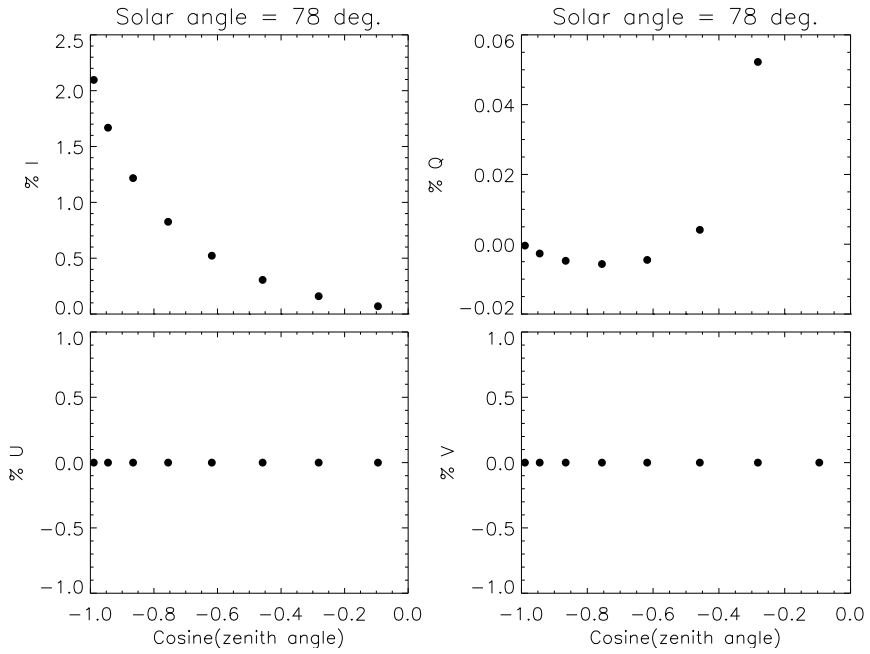

FIGURE 4.15: Pseudo–spherical vs. plane–parallel % differences for a Mie atmosphere for I, Q, U and V Stokes components, Solar angle = 78°. azimuth = 180°

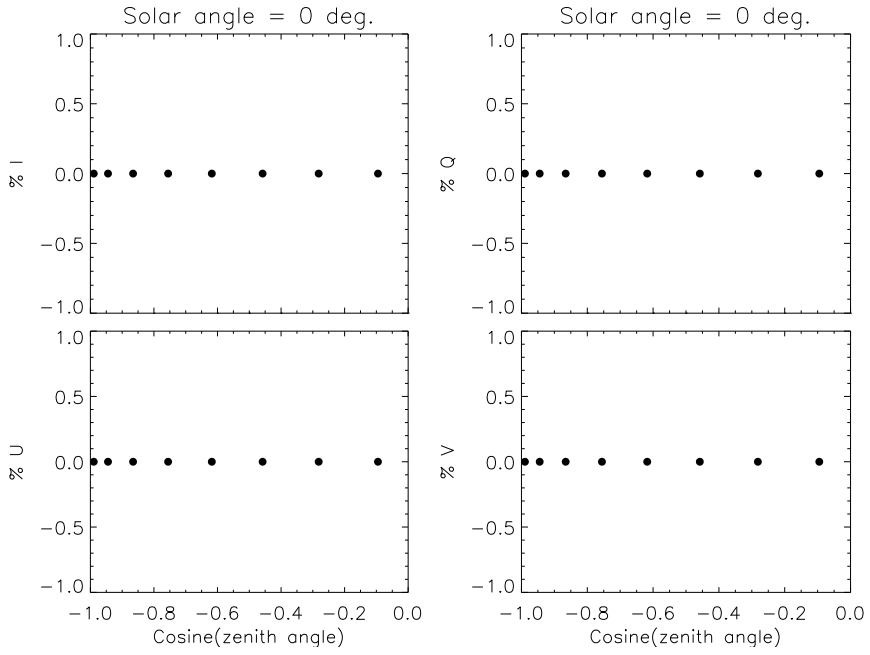

FIGURE 4.16: Pseudo–spherical vs. plane–parallel % differences for a Mie atmosphere for I, Q, U and V Stokes components, Solar angle = 0°.

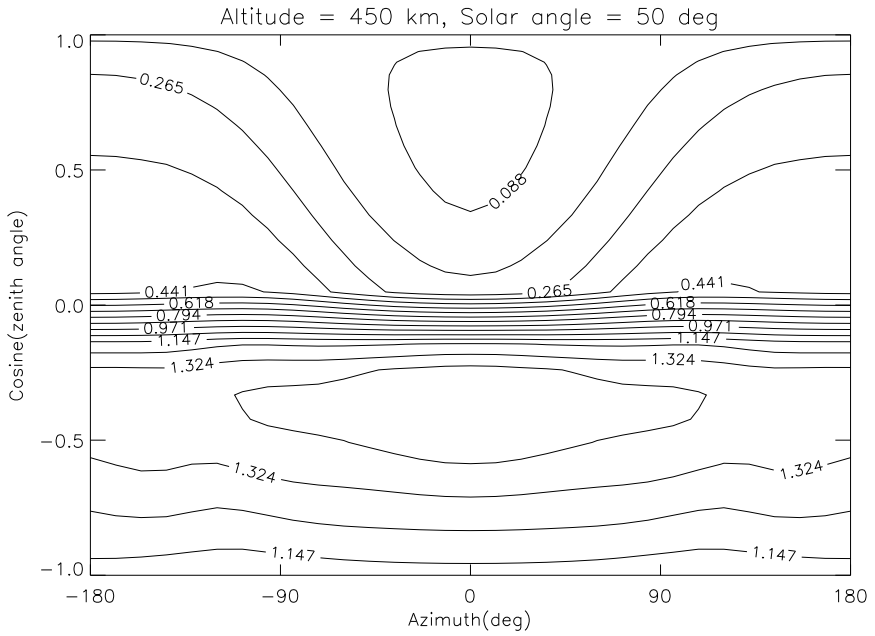

FIGURE 4.17: Pseudo–spherical vs. plane–parallel % differences for Titan's atmosphere at 450km. and solar zenith angle = 50°

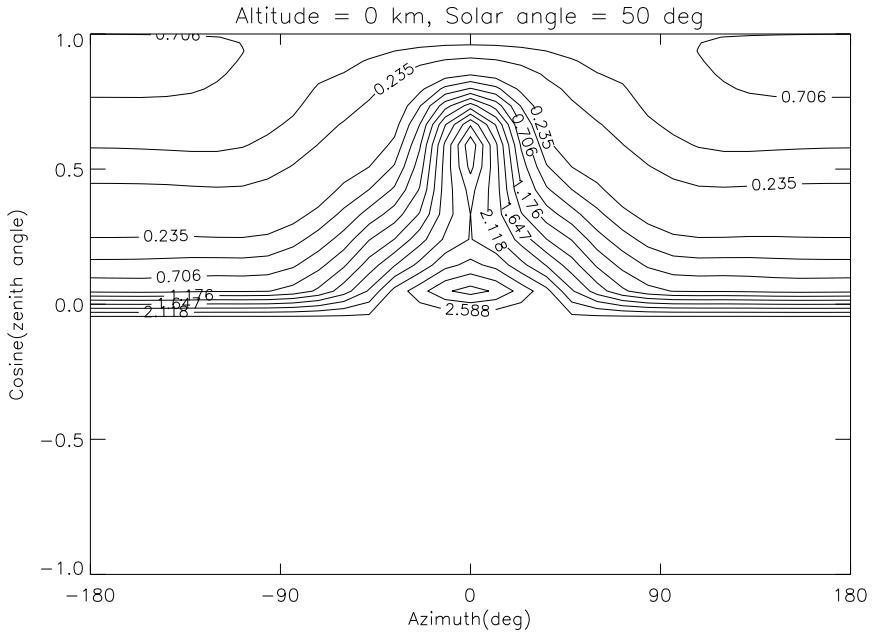

FIGURE 4.18: Pseudo–spherical vs. plane–parallel % differences for Titan's atmosphere at ground level and solar zenith angle = 50°

Chapter 5

Polarized radiation in spherical atmospheres

The subject of radiative transfer or transport deals with the interaction of radiation and matter. Mathematically, one is confronted with the task of seeking a solution to boundary value problems through integro–differential and integral equations for transfer or transport processes. Exact solutions are rarely available in most cases. Consequently, a wide variety of methods have been developed which give approximate solutions to such problems.

For plane–parallel participating media, the methods for solving the radiative transfer equation are in an advanced state of development. However, there exist a number of problems in radiative transfer where the curvature of the medium cannot be ignored. To solve these problems, innovative techniques are often required to extend the methods for a plane medium to a spherical or general curvilinear medium. In this section we introduce methods that have been used to solve transfer problems in spherical media and propose a method able to solve the problem of scattering of polarized radiation in spherical planetary atmospheres.

5.1 Methods of computational radiative transfer

Given the ubiquitous nature of radiative transfer problems, many methods have been developed to solve such a problem numerically dating back to the origin of modern scientific computing. However, due to the great complexity of the problem these methods quite often do not treat the most general case of solving the multi–frequency, three–dimensional, time dependent, polarized radiative transfer equation in a medium in which non–local thermodynamical equilibrium conditions apply but some simplified version applicable to a specific problem. Each of these methods has both its advantages and disadvantages. Herein, we discuss the most common methods used in the solution of multi–dimensional problems. However, in this discussion, we do not include the topic of polarization.

5.1.1 Monte Carlo method

A well-known method which complies with most of the requirements formulated above is the Monte Carlo technique (Marchuk et al. 1980). In a Monte Carlo computation a photon at a time is followed its three–dimensional path through a scattering medium. The various events which the photon might go through are defined by a suitable probability distributions. A set of random numbers is then used to make a particular choice for the interpretation of each event. The intensity of radiation is then determined statistically by following a large number of individual photon trajectories through the atmosphere. There are three different useful Monte Carlo methods. In two of these the photons are followed in the forward direction and the collisions occur in the same order as they do in a real atmosphere. The other method is the backward Monte Carlo method. In this method the photons are started from the detector and their path is followed backward to the point where they leave the atmosphere toward the Sun. This technique is very effective when the receiver has a narrow field of view because all simulated photons contribute to the signal, whereas in a forward simulation only a small fraction of the photons coming from the Sun reach the instrument. According to Lenoble (1985), the advantages of the Monte Carlo method are:

- Any phase matrix might be used. Any phase function or experimental tabulated phase functions can be easily incorporated.
- Calculations for polarization take only slightly more than twice the computing time as the scalar calculation.
- Any reasonable number of 'detectors' may be used without appreciably increasing computing time.
- The atmosphere can be divided in to a large number of sub–layers, each of them with different properties.
- Problems involving spherical geometry have been solved.
- "Truly" multi–dimensional problems have been solved (variation of the medium properties with position in the atmosphere).

The disadvantages of the method are:

- There is a statistical fluctuation in the results. It is not practical to increase accuracy appreciably since computer times increases four fold for a two fold increase in accuracy.
- The accuracy of the backward Monte Carlo method is poor when the medium is optically thick or has a weak absorption
- Using the quasi Monte Carlo technique (O'Brien 1992), the calculation time can be significantly reduced, but the difficulty of the backward Monte Carlo integration in an optically thick or week absorbing atmosphere is not eliminated.

- It is impractical for extremely large optical depths ($\tau > 100$).

Applications of the Monte Carlo method for radiation calculations in a spherical atmosphere can be found in Collins et al. (1972), Oikarinen et al. (1999).

5.1.2 Methods involving Fourier series

There are several methods that have been successfully applied to plane–parallel geometry, among them, the "Spherical Harmonics", "Discrete Ordinates", "Finite Differences" , "Doubling and adding", etc. (several of these methods are discussed in Lenoble (1985)). The common approach used in these methods is the expansion of the intensity and scattering phase function in Fourier series in azimuth rendering effectively an azimuth independent radiative transfer equation. The method is widely used for polarized radiation in plane–parallel atmospheres (see section 4.4.2). Using this approach the radiative transfer equation as given by Eq.(2.45) for an arbitrary selected solar zenith angle can be split into a system of independent equations for each Fourier coefficient,

$$\cos(\theta)\frac{d\mathbf{I}_{\rm dif}^{(m)}(z,\theta)}{dz} = -\kappa(z)\left(\mathbf{I}_{\rm dif}^{(m)}(z,\theta) - \mathbf{S}_{\rm ms}^{(m)}(z,\theta) - \mathbf{S}_{\rm ss}^{(m)}(z,\theta)\right). \tag{5.1}$$

For unpolarized radiation in a spherical atmosphere, the Fourier expansion in azimuth can be used only if the dependence of the intensity of the diffuse radiation on global azimuth angle Φ is neglected. In this case, the radiative transfer equation given by Eq.(3.39) is appropriate. Combining the Fourier expansion with Eq.(3.39) we obtain,

$$\begin{aligned}\cos\theta\frac{\partial I_{\rm dif}^{(m)}}{\partial r} + \frac{\sin\theta}{r}\left[\frac{1}{2}\frac{\partial I_{\rm dif}^{(m-1)}}{\partial\Psi} + \frac{1}{2-\delta_{0,m}}\frac{\partial I_{\rm dif}^{(m+1)}}{\partial\Psi}\right] - \frac{\sin\theta}{r}\frac{\partial I_{\rm dif}^{(m)}}{\partial\theta} \\ -\frac{\sin\theta\cot\Psi}{r}\left[\frac{m-1}{2}I_{\rm dif}^{(m-1)} + \frac{m+1}{2-\delta_{0,m}}I_{\rm dif}^{(m+1)}\right], \\ = -\kappa\left(I_{\rm dif}^{(m)} - S_{\rm ms}^{(m)} - S_{\rm ss}^{(m)}\right) \quad m = 0,1,\cdots,M. \end{aligned} \tag{5.2}$$

Here, $S_{\rm ms}^{(m)}$ and $S_{\rm ss}^{(m)}$ are the Fourier expansion coefficients for multiple scattering and single scattering source functions in a spherical atmosphere. In the case of polarized radiation in a spherical atmosphere, the equations are much more involved since the sine and cosine modes of the Fourier expansion do mix. The spherical Fourier expansion is obtained analogously to the plane–parallel case. As clearly seen, the equation for the m–th Fourier coefficients contains also the $(m-1)$–th and the $(m+1)$–th coefficients of the Fourier expansion for the intensity. This means that each equation has to be solved in combination with two neighboring equations i.e. the system cannot be split into independent equations anymore. Since the possibility to solve the radiative transfer equation for each Fourier mode is the main advantage of the Fourier method, it is only reasonable to use it for spherical atmospheres if an azimuthal independent radiation field and no external anisotropic illumination is considered. Thus, this method is not suitable for our purposes since we consider azimuthal dependence of the radiation field.

5.1.3 Method of moments

The "Moment approach" (Sobolev 1975) was first introduced for a plane– parallel atmosphere and further extended by Sobolev and Minin (1962) for a spherical shell atmosphere. The moment method builds on the idea of solving the radiative transfer equation for the moments of the intensity instead of the intensity itself; if we consider unpolarized radiation, the moments are defined by (Sobolev 1975)

$$M_0(r,\psi) = \frac{1}{4\pi}\int_0^{2\pi} d\phi \int_0^{\pi} \sin\theta I(r,\Psi,\theta,\phi)d\theta, \tag{5.3}$$

$$M_1(r,\psi) = \frac{1}{4\pi}\int_0^{2\pi} d\phi \int_0^{\pi} \sin\theta\cos\theta I(r,\Psi,\theta,\phi)d\theta, \tag{5.4}$$

$$M_0(r,\psi) = \frac{1}{4\pi}\int_0^{2\pi} d\phi \int_0^{\pi} \sin^2\theta\cos\phi I(r,\Psi,\theta,\phi)d\theta. \tag{5.5}$$

The zero–th moment, M_0 is the mean intensity of the diffuse radiation, the first moment M_1 is proportional to the vertical flux of the diffuse radiation and the second moment M_2 is proportional to the flux of the diffuse radiation in the direction $\phi = 0$ in a horizontal plane.

The moment method consist of calculating the first–order scattering exactly and the higher order scattering by approximating the phase function with only two terms of the Legendre expansion of the phase function, more precisely,

$$P(\gamma) = 1 + \chi_1\cos\gamma. \tag{5.6}$$

Combining Eqs.(3.35)–(3.38) and Eqs.(5.3)–(5.5) the total source function becomes,

$$B = \varpi(M_0 + \chi_1 M_1\cos\theta + \chi_1 M_2\sin\theta\cos\phi) + \\ + \frac{\varpi(r)}{4\pi}F_0(1 - \chi_1\cos\theta + \chi_1\sin\theta\sin\Psi\cos\phi)e^{(-T(r,\psi))}, \tag{5.7}$$

where $-T(r,\psi)$ is the optical depth along a ray from the Sun to a given point in the atmosphere, i.e.,

$$T(r,\psi) = \int_z^{\infty}\kappa(\hat{r})d\hat{z}., \quad z = r\cos\psi \quad \text{and} \quad r^2 = r^2\sin^2\psi + \hat{z}^2. \tag{5.8}$$

According to Sobolev (1975), the quantity B (and therefore also I) may be expressed as a combination of the moments M_0, M_1 and M_2 each of which depends only on the two variables r and Ψ by the system of equations,

$$\frac{\partial M_1}{\partial r} + \frac{2}{r}M_1 + \frac{1}{r}\frac{\partial M_2}{\partial\Psi} + \frac{\cot\Psi}{r}M_2 = -\kappa(1-\varpi)M_0 + \kappa\frac{\varpi}{4\pi}F_0e^{(-\tau)}, \tag{5.9}$$

$$(3 - \varpi\chi_1)M_1 = -\frac{1}{\kappa}\frac{\partial M_0}{\partial r} - \frac{\varpi}{4\pi}F_0\chi_1\cos\Psi e^{(-\tau)}, \tag{5.10}$$

$$(3 - \varpi\chi_1)M_2 = -\frac{1}{(\kappa\, r)}\frac{\partial M_0}{\partial \Psi} - \frac{\varpi}{4\pi}F_0\chi_1 \sin\Psi e^{(-\tau)}. \tag{5.11}$$

These equations where obtained after multiplying Eq.(3.39) by $d\omega/4\pi$, $\cos\theta d\omega/4\pi$ and $\sin\theta\cos\phi d\omega/4\pi$ with $d\omega = d\theta\ d\phi$ and integrating over all directions.

Solving the system of differential equations Eqs.(5.9)–(5.11) all three moments can be found and the source function, as given by Eq.(5.7), can be calculated. Once the source function is known, the integro–differential radiative transfer equation Eq.(3.39) becomes a partial differential equation that can be solved by any standard numerical technique.

The main disadvantages of the method are the simplified consideration of the azimuthal dependence of the diffuse radiation. The actual phase function is truncated and only the first two terms of the Legendre expansion are retained and as a consequence only first–order scattering is maintained.

5.1.4 Other methods

Other methods are available for solving the radiative transfer equation in multi–dimensional spherical or Cartesian coordinates, methods such as the Gauss–Seidel iteration scheme reported by Herman et al. (1994) which calculates the radiation field throughout the entire hemisphere by employing a conical boundary surrounding the zenith direction along which the solution is desired.

There are also radiative transfer models which use some approximations enabling the mean intensity in a spherical atmosphere to be calculated efficiently. For example in Dahlback & Stamnes (1991), the azimuthally averaged radiative transfer equation was solved iteratively considering the spherical terms as a perturbation. Such models however, can not reproduce the angular dependence of the radiance accurately.

Recently Rozanov et al. (2001) has proposed a method for solving the unpolarized radiative transfer equation in its integral form for a spherical planetary atmosphere (initially developed for Earth's atmosphere) using the method of *characteristics* (Courant & Hilbert 1962). This method is combined with the Picard iterative approximation starting from an initial guess based on a 1–D finite differences solution.

5.2 Characteristics method

The arrival of the *Cassini/Huygens* mission to Titan in early 2005 (Grieger et al. 2002, 2003) makes the development of accurate and efficient radiative transfer models for the interpretation of direct and diffuse radiation scattered in the atmosphere of Titan or reflected from its surface necessary. To address the radiation problem in an optically thick atmosphere such as Titan's and to take into account its spherical nature, we have implemented a multi–dimensional method able to solve the full problem. The method builds upon existing knowledge of light scattering in plane–parallel atmospheres (Hansen & Travis 1974, Evans & Stephens 1991, Caudill et al. 1997, Rozanov et al. 2000) and recent methods developed for spherical atmospheres (Balluch 1996, Evans 1998, Herman et al. 1994, Dahlback & Stamnes 1991, Rozanov et al. 2001). Several of these methods

are described in Chandrasekhar (1965), Sobolev (1975), Sen & Wilson (1990), Lenoble (1985).

In our view such a model has to incorporate the following characteristics:

- Accurately determine multiple scattered radiation in a spherical atmosphere for all relevant solar angles and viewing geometries.
- Be able to incorporate a wide range of phase functions.
- Allow optical properties and phase functions of the medium to vary spatially.
- Readily include polarization and be moderate in required computational resources.

Methods to solve the radiative transfer equation for a spherical atmosphere have been discussed above. Taking into consideration the requirements formulated at the beginning only the full differential spherical operator as in Eqs.(3.33)–(3.34) is suitable to solve the radiative transfer equation for a spherical planetary atmosphere with the required accuracy. As discussed in section (3.2) the full differential spherical operator is given by

$$\begin{aligned}\frac{d\mathbf{I}}{ds} &= \left(\cos\theta\frac{\partial}{\partial r}+\frac{\sin\theta\cos\phi}{r}\frac{\partial}{\partial\Psi}+\frac{\sin\theta\sin\phi}{r\sin\Psi}\frac{\partial}{\partial\Phi}\right.\\ &\qquad\left.-\frac{\sin\theta}{r}\frac{\partial}{\partial\theta}-\frac{\sin\theta\cos\phi\cot\Psi}{r}\frac{\partial}{\partial\phi}\right)\mathbf{I}. \qquad (5.12)\end{aligned}$$

As it can be seen, a first order partial differential equation for the Stokes vector $\mathbf{I}$ as a function of five variables $(r,\Psi,\Phi,\theta,\phi)$ has to be solved.

One of the well known methods to solve this equation is the *characteristics* method. Rozanov et al. (2001) describes the method for the case of a spherical planetary atmosphere for the scalar problem (without polarization). Herein, we have adopted this method and have combined it with the one–dimensional pseudo–spherical method described in Chapter (4) to develop a radiative transfer code able to solve the fully polarized integro–differential radiative transfer equation for a spherical planetary atmosphere. The main differences of our approach besides the full treatment of polarization are the ability to handle any kind of phase functions via Legendre polynomials and/or generalized spherical functions, a fast initial guess approximation using the doubling & adding algorithm as described in Section (4.4), the inclusion of internal sources of radiation and the inclusion of Lambertian and Fresnel surface reflection.

As pointed out by Rozanov et al. (2001), the *characteristics* method performs the conversion of the first order partial differential equation into an integral equation by integrating its both sides along a *characteristic*. Further, if we do not take refraction effects into account the *characteristics* are straight lines, therefore the direction cosines are then simply given by $\eta_1=\cos\phi\ \sin\theta$, $\eta_2=\sin\phi\ \sin\theta$ and $\eta_2=\cos\theta$. The angle variables θ and ϕ are assumed to be functions of the global angles Ψ and Φ.

In the remainder of this section we adopt the mathematical formulation of Rozanov et al. (2001) for all computations and include polarization implicitly via de Stokes parameters (I,U,V,Q) for all radiances ($\mathbf{I}$) and sources ($\mathbf{S}$).

In general, the radiation field $\mathbf{I}(r, \Psi, \Phi, \theta, \phi)$ can be split into two components: diffuse and direct radiance,

$$\mathbf{I}(r, \Psi, \Phi, \theta, \phi) = \mathbf{I}_{\text{dir}}(r, \Psi, \Phi, \theta, \phi) + \mathbf{I}_{\text{dif}}(r, \Psi, \Phi, \theta, \phi). \tag{5.13}$$

The direct radiance can be calculated as follow :

$$\mathbf{I}_{\text{dir}}(r, \Psi, \Phi, \theta, \phi) = \pi \mathbf{F}_0 \delta(\cos\theta + \cos\Psi, \phi) e^{-\int_0^{s_0} \kappa(\hat{s}) d\hat{s}}, \tag{5.14}$$

where $\pi\mathbf{F}_0$ is the incident solar flux vector, δ is the Dirac delta– function and s_0 denotes the full path–length along the direct solar beam from the top of the atmosphere to point r. The general solution for the diffuse radiance for any direction $(\mathbf{r}, \mathbf{\Omega})$ can be written as:

$$\mathbf{I}_{\text{dif}}(\mathbf{r}, \mathbf{\Omega}) = \mathbf{I}_{\text{dif}}(\mathbf{r}_0, \mathbf{\Omega}) e^{-\tau(s_c)} + \int_0^{s_c} \mathbf{S}(\tilde{\mathbf{r}}, \tilde{\mathbf{\Omega}}) \kappa(\tilde{\mathbf{r}}) e^{-\tau(s)} ds, \tag{5.15}$$

here $\mathbf{I}_{\text{dif}}(\mathbf{r}_0, \mathbf{\Omega})$ is the diffuse radiance and the end of the characteristic (line of sight) i.e. at the boundary (the top or the bottom) of the atmosphere in direction $\mathbf{\Omega}$, s_c is the full length of the characteristic and $\tau(s)$ is the optical depth.

If we start at any boundary and integrate along a given *characteristic* then the following integral form of the radiative transfer equation is obtained:

$$\mathbf{I}_{\text{dif}}(r, \Psi, \Phi, \theta, \phi) = \mathbf{I}_0(r, \Psi, \Phi, \theta, \phi) + \mathbb{L}_{\text{s}}^{\text{sp}} \mathbf{S}(\tilde{r}, \tilde{\Psi}, \tilde{\Phi}, \tilde{\theta}, \tilde{\phi}). \tag{5.16}$$

Here $\mathbf{I}_0(r, \Psi, \Phi, \theta, \phi)$ is defined by the boundary conditions. The integral operator $\mathbb{L}_s^{\text{sp}}$ (Rozanov et al. 2001) is given by,

$$\mathbb{L}_s^{\text{sp}} = \int_0^{s_c} \kappa(s) e^{(-\int_0^s \kappa(\tilde{s}) d\tilde{s})} ds, \tag{5.17}$$

where κ is the extinction coefficient, s the pathlength along the *characteristic* and s_c the full length of the *characteristic*. Variables $\tilde{r}, \tilde{\Psi}, \tilde{\Phi}, \tilde{\theta}$,and $\tilde{\phi}$ are functions of s. Eq.(5.16) is only a formal solution of the differential equation Eq.(3.34), because the source function $\mathbf{S}(\tilde{r}, \tilde{\Psi}, \tilde{\Phi}, \tilde{\theta}, \tilde{\phi})$ is a functional of the diffuse radiance $\mathbf{I}_{\text{dif}}(\tilde{r}, \tilde{\Psi}, \tilde{\Phi}, \hat{\theta}, \hat{\phi})$:

$$\mathbf{S}(\tilde{r}, \tilde{\Psi}, \tilde{\Phi}, \tilde{\theta}, \tilde{\phi}) = \mathbb{L}_{\text{a}}\, \mathbf{I}_{\text{dif}}(\tilde{r}, \tilde{\Psi}, \tilde{\Phi}, \hat{\theta}, \hat{\phi}) + \mathbf{S}_{\text{ss}}(\tilde{r}, \tilde{\Psi}, \tilde{\Phi}, \tilde{\theta}, \tilde{\phi}). \tag{5.18}$$

$\mathbb{L}_{\text{a}}$ is an angular integration operator (Rozanov et al. 2001) given by

$$\mathbb{L}_{\text{a}} = \frac{\varpi(\tilde{r})}{4\pi} \int_0^{2\pi} d\hat{\phi} \int_0^{\pi} \mathbb{M}(\tilde{r}, \tilde{\Psi}, \tilde{\Phi}, \hat{\theta}, \hat{\phi}) \sin\hat{\theta} d\hat{\theta}, \tag{5.19}$$

where $\omega(\tilde{r})$ is the single scattering albedo and $\mathbb{M}(\tilde{r}, \tilde{\Psi}, \tilde{\Phi}, \hat{\theta}, \hat{\phi})$ is the polarized scattering or Mueller matrix. Further details will be given below.

Using the above defined operators, we rewrite Eq.(5.16) as follow:

$$\mathbf{I}_{\text{dif}}(r, \Psi, \Phi, \theta, \phi) = \mathbf{J}(r, \Psi, \Phi, \theta, \phi) + \mathbb{L}_s^{\text{sp}} \mathbb{L}_{\text{a}} \mathbf{I}_{\text{dif}}(\tilde{r}, \tilde{\Psi}, \tilde{\Phi}, \hat{\theta}, \hat{\phi}), \tag{5.20}$$

with

$$\mathbf{J}(r, \Psi, \Phi, \theta, \phi) = \mathbf{I}_0(r, \Psi, \Phi, \theta, \phi) + \mathbb{L}_s^{\text{sp}} \mathbf{S}_{\text{ss}}(\tilde{r}, \tilde{\Psi}, \tilde{\Phi}, \tilde{\theta}, \tilde{\phi}). \tag{5.21}$$

Eq.(5.20) is a linear integral operator equation which can be solved by an iterative scheme, in our case we use the Picard iterative approximation given by

$$\mathbf{I}_{\rm dif}^{(n)}(r,\Psi,\Phi,\theta,\phi) = \mathbf{J}(r,\Psi,\Phi,\theta,\phi) + \mathbb{L}_s^{\rm sp}\mathbb{L}_{\rm a}\mathbf{I}_{\rm dif}^{(n-1)}(\tilde{r},\tilde{\Psi},\tilde{\Phi},\hat{\theta},\hat{\phi}). \tag{5.22}$$

This iterative scheme has been used in plane–parallel and 3–D radiative transfer calculations such as SHDOM (Evans 1998) and the Picard Iterative scheme (Kuo et al. 1995a,b).

From Eq.(5.16), we notice that it has the form $\mathbf{I} = \mathbb{F}(\mathbf{I})$. This form of the radiative transfer equation naturally suggests that a fixed point iteration is appropriate for a numerical solution. The radiance, $\mathbf{I}$, is a fixed point of the function $\mathbb{F}(\mathbf{I})$. In order to locate such a fixed points one begins with an initial estimate $\mathbf{I}^0$ (which undoubtedly is not a fixed point) and computes in succession: $\mathbf{I}^{(1)} = \mathbb{F}(\mathbf{I}^{(0)})$, $\mathbf{I}^{(2)} = \mathbb{F}(\mathbf{I}^{(1)})$, $\cdots$,$\mathbf{I}^{(n)} = \mathbb{F}(\mathbf{I}^{(n-1)})$. If the sequence $\mathbf{I}^{(n)}$ converges to the limit $\mathbf{I}$ and the function satisfies some continuity conditions (Kuo et al. 1995a,b) then one obtains $\mathbb{F}(\mathbf{I}^{(n)}) \rightarrow \mathbb{F}(\mathbf{I})$. Thus to exploit this technique, for the present multi–dimensional problem, one has to select a suitable starting field $\mathbf{I}^{(0)}$.

5.2.1 The initial field

One way of starting the global iteration is by using single scattering radiance calculated analytically. Another way is to use a semi–analytical approach such as the successive order of scattering (SOS) method which uses the single scattered radiance as an initial estimate to generate higher orders of scattered radiation. As pointed out by O'Brien (1992), the SOS method is logically equivalent to the simulation of trajectories in the backward Monte Carlo approach and it is specially inefficient in optically thick atmospheres. Thus, the major criteria for a desirable solution technique is lost since we would like a fast and efficient algorithm to generate our initial guess solution. In Kuo et al. (1995a,b), in the case of a plane–parallel atmosphere, the radiance was obtained by employing a low order expansion of the spherical harmonics solution as an initial guess for a similar iterative scheme. It has been shown that using such an initial guess solution fewer iterations are required compared to the SOS method to achieve convergence.

In this work, we generate an initial guess solution using the doubling and adding algorithm (D&A). The D&A method has been proven to be very efficient for optically thick atmospheres. It is fast and conceptually easy to implement and generalize. In our implementation we have included a spherical correction for the direct solar beam to obtain a pseudo–spherical initial guess solution. The idea behind this method (Rozanov et al. 2001) for the case of a spherical atmosphere is that a better initial approximation can be achieved by retaining the local integral operator $\mathbb{L}_{\rm a}$ of Eq.(5.20) and simplifying instead the integral operator $\mathbb{L}_s^{\rm sp}$ which characterizes the global behavior of light in the atmosphere.

According to Rozanov et al. (2001) simplifying the differential operator as given by equations Eq.(3.40) and Eq.(3.40) does not simplify the integral operator $\mathbb{L}_s^{\rm sp}$. The one–dimensional differential operator $\mathbb{L}_s^{\rm pp}$ is used in our radiative transfer model instead of $\mathbb{L}_s^{\rm sp}$ to obtain an initial estimation of the radiation field. This means the first guess radiance $\mathbf{I}_{\rm dif}^{(0)}(r,\Psi,\Phi,\theta,\phi)$ has to satisfy the following equation:

$$\mathbf{I}^{(0)}_{\rm dif}(r,\Psi,\Phi,\theta,\phi) = \mathbf{J}(r,\Psi,\Phi,\theta,\phi) + \mathbb{L}^{\rm pp}_s \mathbb{L}_{\rm a} \mathbf{I}^{(0)}_{\rm dif}(\tilde{r},\tilde{\Psi},\tilde{\Phi},\hat{\theta},\hat{\phi}), \tag{5.23}$$

where the one–dimensional plane–parallel integral operator $\mathbb{L}^{\rm pp}_s$ is given by

$$\mathbb{L}^{\rm pp}_s = \frac{1}{\cos\theta}\int_r^{r_b} d\tilde{r}\kappa(\tilde{r})\exp\left(-\frac{1}{\cos\theta}\int_r^{\tilde{r}}\hat{\kappa}(\hat{r})d\hat{r}\right), \tag{5.24}$$

here r_b refers to the medium boundary and the corresponding differential operator is,

$$\frac{d}{ds} = \cos\theta\frac{\partial}{\partial r}. \tag{5.25}$$

Notice Eq.(5.23) is a pseudo–spherical solution since the term **J** contains the direct solar beam calculated as in a spherical atmosphere and the second term on the right hand side is the multiple scattering term calculated as in a plane–parallel atmosphere. Therefore, using the pseudo–spherical solution as an initializer allows us to introduce all scattering orders at once in the initial guess solution.

5.2.2 Multidimensional integration of the RTE

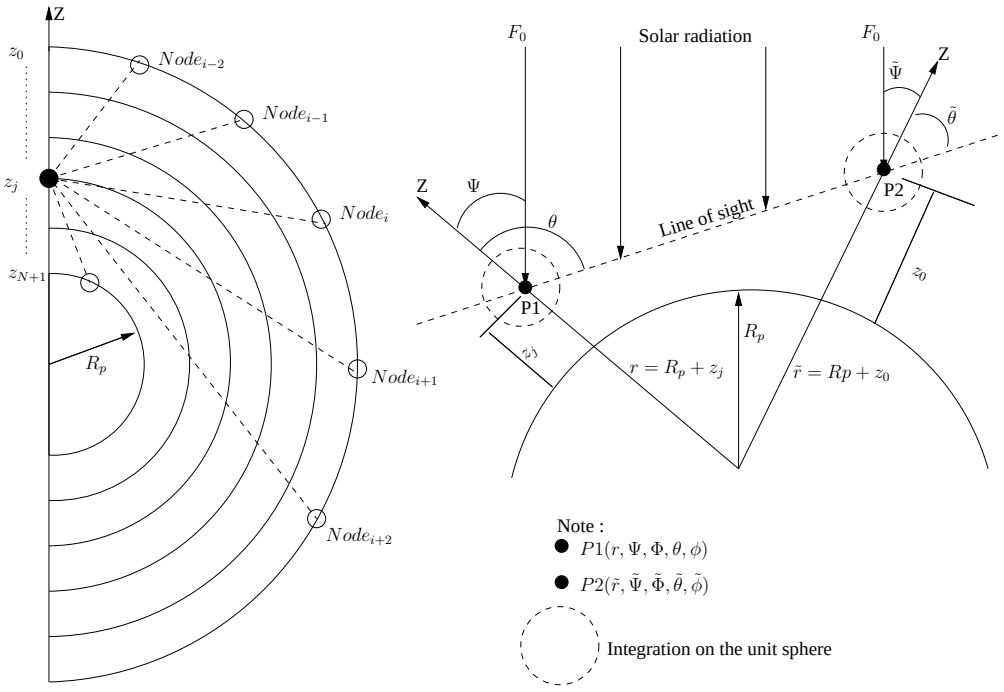

FIGURE 5.1: Characteristic integration along the line of sight for a spherical atmosphere.

Once the initial radiation field $\mathbf{I}^{(0)}_{\rm dif}$ has been computed (for a set of solar zenith angles) we need to integrate the RTE along the line of sight for prescribed viewing angles. The spatial coordinates of any point on the line of sight $\tilde{r}, \tilde{\Psi}$ and $\tilde{\Phi}$ and the local radiance direction defined by $\tilde{\theta}$ and $\tilde{\phi}$ can be calculated from the initial set of variables r, Ψ, Φ, θ and ϕ using the following relations (see also Fig. 5.1),

$$\tilde{r} = \sqrt{r^2 - 2\,r\,s\,\cos\theta + s^2}, \tag{5.26}$$

$$\cos\tilde{\theta} = \frac{r\,\cos\theta - s}{\tilde{r}}, \tag{5.27}$$

$$\cos\tilde{\Psi} = \frac{r\,\cos\Psi - s\,\zeta}{\tilde{r}}, \tag{5.28}$$

$$\cos\tilde{\Phi} = \frac{r\,\sin\Psi}{\tilde{r}\sin\tilde{\psi}}\cos\Psi - \frac{s}{\tilde{r}\sin\tilde{\Psi}}\eta, \tag{5.29}$$

$$\cos\tilde{\phi} = \frac{\cos\tilde{\psi}\cos\tilde{\theta} - \zeta}{\sin\tilde{\Psi}\sin\tilde{\theta}}. \tag{5.30}$$

The terms η and ζ are given by

$$\eta = \cos\Psi\cos\Phi\sin\theta\cos\phi - \sin\Phi\sin\theta\sin\phi + \sin\Psi\cos\Phi\cos\theta, \tag{5.31}$$

$$\zeta = \cos\Psi\cos\theta - \sin\Psi\sin\theta\cos\phi. \tag{5.32}$$

The set of angular variables $\hat{\theta}$ and $\hat{\phi}$ are chosen according to the integration scheme selected to calculate the double integral in operator $\mathbb{L}_{\rm a}$ of Eq.(5.19). As it was seen in sections (4.4.2) and (4.4.3), for one–dimensional cases the usual approach is to calculate the integral operator $\mathbb{L}_{\rm a}$ as a combination of Gaussian quadrature for θ_i angles and Fourier series expansion for ϕ_i angles. Other used approaches include the spherical harmonics method (Evans 1998), quadrature methods based on the trapezoidal rule etc. The variation of the global and local angular coordinates along the line of sight precludes the use of such a method which are nevertheless very efficient for plane–parallel atmospheres. To solve such a problem, we have included an area equalizing integration scheme able to handle the angular integral (integration on the unit sphere, Fig. 5.2) of Eq.(5.19).

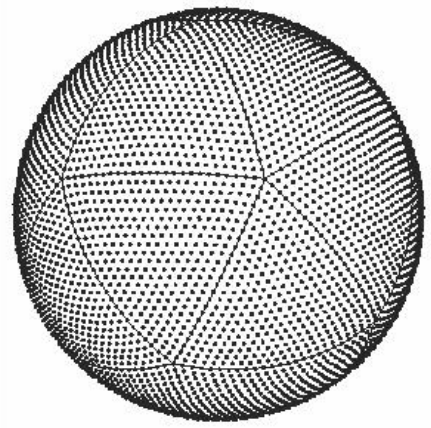

FIGURE 5.2: The icosahedron–based pixelization scheme. Each dot represents an integration node which are used to pixelize the unit sphere.

This method is fully described in Tegmark (1996). The idea is to find a good pixelization scheme for the unit sphere (see Fig.5.2). Specifically if we are to place N points

(pixel centers) on the sphere, where is the best place where to put them?. The method uses the following criteria:

- The worst–case distance to the nearest pixel should be minimized.
- It should be able to accurately approximate integrals by sums.

Defining d as the maximum distance that a point on the sphere can be from the pixel closest to it, the first criteria above, seeks to minimize d. The second criteria states that the integral of a function over the sphere should well be approximated by $4\pi/N$ times the sum of the function values at the pixel location.

The icosahedron pixelization scheme basically inscribes a sphere in an icosahedron whose faces are pixelized with a regular triangular grid. Then the points are mapped radially onto the sphere. The points are shifted around slightly to give all pixels approximately equal area. A Fortran package for this scheme is available in:

http://www.hep.upenn.edu/ ˜max/icosahedron.html

5.2.3 Sweeping scheme

Each spatial point $\hat{\mathbf{r}}(\hat{r}_i, \hat{\Psi}_j, \hat{\Phi}_k)$ (where $1 \leq i \leq N_{\text{layers}}+1$, $1 \leq j \leq N_\Psi$ and $1 \leq k \leq N_\Phi$) represents a physical location in the atmosphere at which the radiation field is calculated and stored. For notational convenience the r grid is labeled such that $r_{N_{\text{layers}}+1} = R_p$ and $r_1 = R_p + Z_{\text{atm}}$ (R_p is the planet's radius and Z_{atm} is the height of the atmosphere). In each spatial point, we establish a local non-uniform grid $\hat{\mathbf{\Omega}}(\hat{\theta}_k, \hat{\phi}_k)$ (where $1 \leq k \leq N_{\text{nodes}}$) of k nodes which are the integration nodes generated by the icosahedron method. Unlike the planar case, the local angles depend on the spatial point of interest.

In order to compute $\mathbf{I}^{(n)}_{\text{dif}}(\hat{\mathbf{r}}, \hat{\mathbf{\Omega}})$, a line integration is carried out along a line through $\hat{\mathbf{r}}$ and parallel to $\hat{\mathbf{\Omega}}$. This path is called a *characteristic*. This *characteristic* will intersect the boundary in at most two points. At the boundary, for which direction $\hat{\mathbf{\Omega}}$ points into the interior of the atmosphere, $\mathbf{I}^{(n)}_{\text{dif}}(\hat{\mathbf{r}}, \hat{\mathbf{\Omega}})$ is computed successively for each inner radii along the *characteristic*. Eqs. (5.27)–(5.30) are used to calculate the full angular variation along the line of sight for each grid point intersection $(\hat{\mathbf{r}}, \hat{\mathbf{\Omega}} \rightarrow \tilde{\mathbf{r}}, \tilde{\mathbf{\Omega}})$.

The initial radiation field $\mathbf{I}^{(n-1)}_{\text{dif}}$ is interpolated (using cubic interpolation) to match the new angles in direction $(\tilde{\mathbf{r}}, \tilde{\mathbf{\Omega}})$. The scattering angle is calculated for the new local angles $\tilde{\mathbf{\Omega}}$ and the polarized Mueller (or scattering) matrix is then rotated to the new local meridional plane at position $(\tilde{\mathbf{r}}, \tilde{\mathbf{\Omega}})$ for each integration node and the multiple scattering source function is evaluated. A similar process is followed to compute the single scattered source function for direction $(\tilde{\mathbf{r}}, \tilde{\mathbf{\Omega}})$.

The process is performed until the boundary is reached. If the *characteristic* reaches the surface the appropriate ground reflection is applied, if the *characteristic* leaves the atmosphere, no boundary radiation is added. The process is repeated for all integration nodes and for each global iteration. After each iteration a convergency check is performed and the next iteration $\mathbf{I}^{(n+1)}_{\text{dif}}(\hat{\mathbf{r}}, \hat{\mathbf{\Omega}})$ is started. The full sweeping scheme can now be expressed algorithmically as (Rozanov et al. 2001),

$$\mathbf{I}_{\rm dif}^{(n)}(\hat{r},\hat{\Psi},\hat{\Phi},\hat{\theta},\hat{\phi}) \overset{\text{interpolation}}{\longrightarrow} \mathbf{I}_{\rm dif}^{(n)}(\tilde{r},\tilde{\Psi},\tilde{\Phi},\hat{\theta},\hat{\phi}), \tag{5.33}$$

$$\downarrow$$

$$\mathbf{S}_{\rm ms}^{(n)}(\tilde{r},\tilde{\Psi},\tilde{\Phi},\tilde{\theta},\tilde{\phi}) = \mathbb{L}_{\rm a}\mathbf{I}_{\rm dif}^{(n)}(\tilde{r},\tilde{\Psi},\tilde{\Phi},\hat{\theta},\hat{\phi}), \tag{5.34}$$

$$\downarrow$$

$$\mathbf{I}_{\rm dif}^{(n+1)}(\hat{r},\hat{\Psi},\hat{\Phi},\hat{\theta},\hat{\phi}) = \mathbf{J}(\hat{r},\hat{\Psi},\hat{\Phi},\hat{\theta},\hat{\phi}) + \mathbb{L}_s^{\rm sp}\mathbf{S}_{\rm ms}^{(n)}(\tilde{r},\tilde{\Psi},\tilde{\Phi},\tilde{\theta},\tilde{\phi}), \tag{5.35}$$

where $\mathbb{L}_{\rm a}$ is the angular integration operator given by Eq. (5.19) and $\mathbb{L}_s^{\rm sp}$ is the spherical integration operator given by Eq.(5.17). The vector $\mathbf{J}(\hat{r},\hat{\Psi},\hat{\Phi},\hat{\theta},\hat{\phi})$ contains all terms of the radiative transfer equations that require no iteration (as given in Eq.5.20) and remains unchanged during the iterations.

5.3 Numerical results

5.3.1 Convergence of iterative scheme

As was mentioned before, the pseudo–spherical radiation field when used as a global initializer causes the iterative scheme to converge rapidly. Typically three to four global iterations are necessary to obtain convergency for a full spherical solution. In order to estimate the accuracy obtained after each iteration, the solutions for two consecutive global iterations were plotted in Fig.(5.3).

We observed that after the second global iteration the maximum differences are around 5% or less; a huge improvement was obtained after the 3rd iteration where the differences are less than 1% (as seen in Fig 5.3) and after that the differences are almost negligible. As was stated before, the convergency properties of the Picard iterative approximation (or fixed point iteration) are vastly improved and typically few global iterations are needed when the initial radiation field is close enough. Nevertheless, in order to guarantee a certain accuracy our model includes a simple convergency rule that increases the number of iterations when needed. Furthermore, an acceleration scheme based on NG acceleration (Ng 1974) is available if more than four iterations are necessary.

5.3.2 Solar angle variation

Our spherical model was run for a standard Titan atmosphere, as described in Grieger et al. (2003) and Salinas et al. (2003). The idea behind this test is to evaluated the variation of diffuse radiance with variation of solar zenith angle for a fixed azimuth angle of view and for a fixed atmospheric altitude.

In Fig.(5.4) we plot radiance as a function of zenith angle for different solar zenith angles at a fixed azimuth. We can quickly notice that when the Sun is high in the sky the

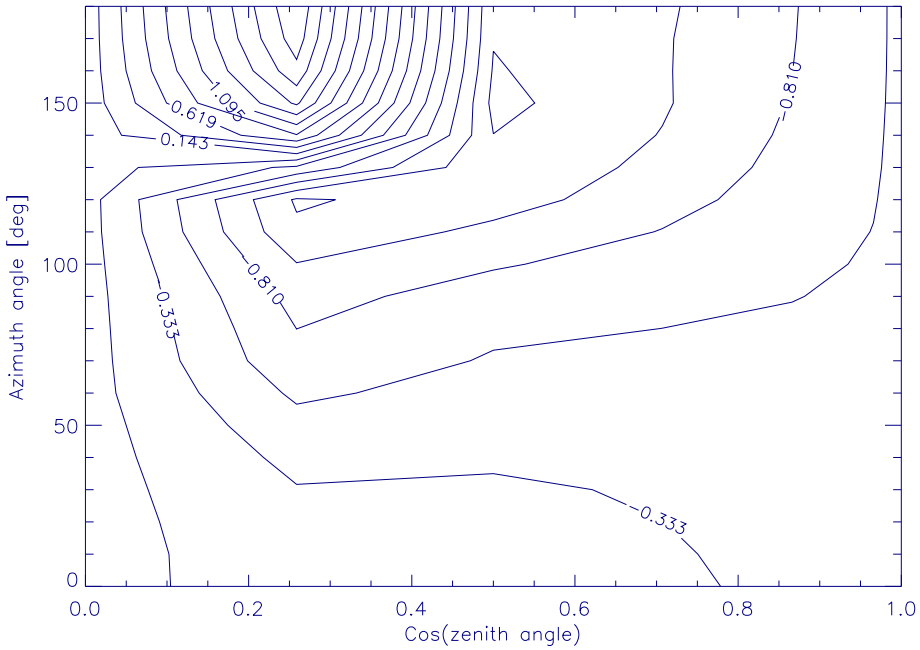

FIGURE 5.3: Relative difference between global iterations, i.e. $(I_{dif}^{(n+1)}/I_{dif}^{(n)} - 1) * 100\%$ as function of zenith angle and azimuth angle at 100 km. altitude and solar zenith angle 50^o.

intensities are larger than when close to the horizon (90° angle of view) and below the horizon (95° angle of view). This differences are due to the larger solar path the streams encounter in limb viewing geometry. Even tough our model uses the multiple scattered radiation essentially from a pseudo–spherical solution, the iterative scheme quickly corrects for the global angular variation and preserves the geometry of the system thus including the solar angle variation along the line of sight.

5.3.3 Validation tests

Analytical solutions to radiation transport in multi–dimensional geometries are rare in the literature, specially if polarization treatment is included into the problem. Numerical solutions, when available, are restrictive in the sense that have been developed for specific applications such as Earth atmosphere (therefore not allowing us to include a wide range of phase functions), do not include polarization and most of them are only available for Cartesian geometry. This limits the available range for direct comparison with other models. One way to validate our model will be to directly compare model calculated radiances with in–situ measurements of known atmospheres if possible or to find limiting cases which will show that we are solving the problem in a self–consistent way.

Under this perspective, we have devised three tests: a self–consistence test and two direct tests that can validate our radiative transfer model. Apart from the self–consistence test, the first direct test is the large radius test. In this test, the planet radius is made extremely large compared with the thickness of the atmosphere. Under this condition,

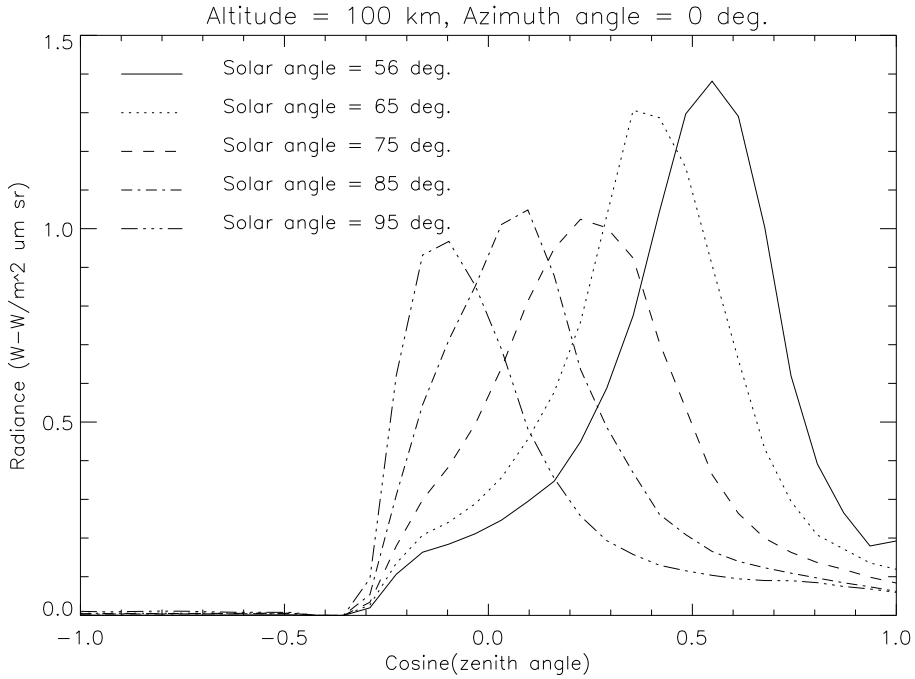

FIGURE 5.4: Radiance variation with solar angle for a set of line of sight view at a fixed azimuth angle.

which is a limiting case, a spherical solution would approach a plane–parallel solution i.e. the full spherical geometry solution would give similar results as in plane–parallel geometry and thus would allow us to validate our model in a simple and direct way. The second test is direct comparison with measured radiance from a know atmosphere. For this test we have chosen the Martian atmosphere since its radiance has been measured at landing sites and the atmospheric properties are fairly known. For this test we have used atmospheric parameters as specified in Markiewicz et al. (1999, 2002).

Self–consistence test

A self–consistence test for the present radiative transfer model was run. The diffuse radiation for the full angle of view and several altitudes was computed performing no global iteration and compared to the input radiance from the pseudo–spherical solution. The intensities in this case are expected to coincide because the pseudo–spherical source function (Eq.5.35) was used and the spherical operator $\mathbb{L}_s^{\mathrm{sp}}$ for such a geometry has to result in the same intensities as in the pseudo–spherical operator i.e. $\mathbb{L}_s^{\mathrm{pp}}$. These intensities were found in an agreement better than 1%. The differences can be mainly attributed to the interpolation scheme we use when performing the spherical calculation as opposed with the pseudo–spherical case and to the change in the computational grid between geometries i.e. we use a uniform regular grid in the plane–parallel case and a non–uniform irregular grid in the spherical case (Sec. 5.2.2).

Large radius test

For plane–parallel problems the only important parameter is the thickness or altitude of the atmosphere, for spherical atmospheres besides atmospheric altitude, the radius of the planet plays an important role in determining the "sphericity" of the atmosphere. When the radius of the planet is large enough compared to the altitude of the atmosphere i.e. $R_{\mathrm{planet}} >> Z_{\mathrm{atm}}$, then angular variations are almost negligible and a limiting case occurs. The spherical calculation approaches the plane–parallel calculation since the "sphericity" of the system is dumped out by the large radius. In order to measure the degree of proximity between both calculations, we performed radiation transfer computations for a prescribed atmosphere and compared their peak intensities for both cases. Fig.(5.5) shows the radiation field in plane–parallel geometry and Fig.(5.6) show contour plots of the radiation field for the spherical case. We observe a deviation of not more than 2% from comparing both cases. The diffuse illumination shown in Fig.(5.6) exhibits a similar behaviour as in the plane–parallel case. There are some differences in the form and shape of the solar aureole. This can be attributed to the different schemes used to integrate the radiation field in a plane–parallel atmosphere (Gaussian integration and Fourier series in azimuth) and the pixelization method employed in the spherical case. As it was explained in sections (4.4.2) and (4.4.3) for the plane–parallel case Gaussian integration coupled with Fourier series in azimuth exactly integrates the Legendre expansion of the scattering phase matrix so that proper normalization is achieved and the system conserves energy. In the spherical case, proper phase function normalization and energy conservation depends very much on the number of nodes we choose to use for integration on the unit sphere. Therefore a relatively large number of integration nodes has to be chosen to ensure energy conservation at the expense of increased computing time.

Martian atmosphere test

In this section, we perform radiative transfer calculations for the optical properties of the Martian aerosols as derived from Imager Mars Pathfinder midday sky brightness data for two geometries, plane–parallel and spherical. The Imager for Mars Pathfinder (IMP) obtained data on the midday sky brightness in filters centered at 443.6, 481.0, 670.8, 896.1 and 965.3 nm (Markiewicz et al. 1999, 2002).

The derived atmospheric properties for day "Sol 56" as explained in the above references are shown in table (5.1) for five wavelengths. These values where fitted with radiative transfer calculations based on the plane–parallel approximation to extract size distributions, optical properties and shape of the aerosols. The estimated values of the refractive index and shape parameters are close to those derived from Viking and Phobos data.

With the derived optical properties of the Martian aerosols it is possible to calculate the diffuse downward intensity as seen from the surface for several wavelengths by using our model in both, plane–parallel and spherical geometry. The aim is two fold: first, to test our model in plane–parallel mode and check if we are able to reproduce the results reported by Markiewicz et al. (1999, 2002). This being the case, we can then use our sample atmosphere and obtain the radiation field for low sun and limb viewing geometry

γ(nm.)	τ		$\nu_{\rm eff}$	b	$\theta_{\rm min}$	n_i	$Q_{\rm ext}$	$Q_{\rm sca}$	$< \cos\ \theta >$
443.6	0.56	1.45	0.28	0.042	170	0.015	2.80	2.09	0.77
481.0	0.60	1.66	0.30	0.051	140	0.009	2.84	2.30	0.75
670.8	0.59	1.60	0.15	0.052	160	0.0032	3.00	2.80	0.73
896.1	0.61	1.85	0.25	0.046	220	0.0038	3.10	2.89	0.74
965.3	0.60	2.00	0.26	0.044	230	0.0024	3.20	3.07	0.72

TABLE 5.1: The optical depth and single scattering properties derived from Sol 56 data (Markiewicz et al. 1999, 2002). γ represents wavelength in nm., τ optical depth, $r_{\rm eff}$ and $\nu_{\rm eff}$ particle's effective radius and effective variance, respectively, b is the slope of the phase function at forward–scatter, $\theta_{\rm min}$ is the scattering angle at which the phase function has its minimum, n_i imaginary part of the index of refraction, $Q_{\rm ext}$ and $Q_{\rm sca}$ extinction and scattering efficiencies, respectively, and $< \cos\ \theta >$ is the asymmetry factor.

by using our spherical model and compare it with reported measurements from landing sites.

Results from plane–parallel computations with our model for two wavelengths are plotted in Fig.(5.7). The input atmospheric parameters are as in Table(5.1). These results where compared with published results from Markiewicz et al. (2002, 1999) and a good agreement was obtained. This result allows us to use this atmospheric setting for a full angle of view radiative transfer calculation in spherical geometry for a low solar angle i.e. $\theta_0 = 90^\circ$, and compare results with in–situ measurements from the imager for Mars Pathfinder experiment (IMP). Further description of the instrument can be found in Smith et al. (1997).

The IMP was designed for a resolution or 1 mrad/pixel with an effective field of view of 248 $\times$ 256 pixel sub–array, which corresponds to 14.4° (horizontal) and 14.0° (vertical). The IMP includes very stable filters between 440 nm and 1000 nm so that the data used for comparison are properly calibrated. We have chosen as a comparison case data from IMP sunset evening aerosol measurements. These measurements are shown in Fig.(5.9) for a wavelength of 443 nm with the Sun slightly above the horizon (0.88 $^\circ$). To test our spherical model, we have made a complete angle of view simulation using the atmospheric parameters, as given by Table(5.1) for a Sun at the horizon. Simulation results for these computations are shown in Fig.(5.8) for two altitudes using a 492 integration nodes over the sphere. The upper plot shows the diffuse intensity as seen at the top of the atmosphere at 30km) altitude. The irregularity of the contour lines is mainly due to the irregular distribution of the integration nodes used making it difficult to resolve the shape of the solar aureole. In the lower plot we display a full angle of view of a Martian sunset as seen from ground level. This computation is especially useful for our validation purposes since data values for a sub field of view is available from the IMP experiment.

Unfortunately the different resolution of IMP solar sunset measurements and model results does not allow us to make a pixel by pixel comparison but we are able to compare scattered radiation intensities from modeling to observations mapped to the model pixels. This is difficult since the output of our simulations spans a whole hemisphere and very few angles will lay within the field of view of the measurements.

Comparing the bottom plot of Fig.(5.8) with the upper plot of Fig.(5.9) we can see that diffuse intensities around the simulated aureole are comparable in magnitude with re-

ported measurements (Fig.5.9). However, the maximum intensities are not directly comparable since the data measurements include the un–scattered direct solar beam which has not been added to our simulated results. The shape of contours of scattered radiation are not well reproduced by our model. This can have two possible explanations: first, our resolution is significatively lower than measurements, which undoubtedly decreases our ability to reproduce the observed contours. Secondly, the phase functions we are using for our simulated sunset are not compleatly suitable since they were retrieved under certain assumptions and approximations (Markiewicz et al. 1999, 2002) The first issue can possibly be reconciled by running high resolution simulations.

The lower plot of Fig.(5.9) shows a direct comparison between simulation results and data from IMP. Several points of our simulations that fall within the field of view of the data set can be directly compared. These simulation values are plotted in red color. In this plot we observe that our results are off by 50% or more in some cases. This can have several explanations, one of them was discussed above, i.e., grid resolution. We can also point out that our model atmosphere setting is spherically symmetric but the input atmospheric parameters were originally retrieved using a plane–parallel method neglecting spatial variation of the phase function and the atmospheric optical parameters. These results coupled with the fact that our phase function did not vary with altitude (the used input phase function was retrieved with a single layer atmosphere) shows the need to take into account spatial variations not only of phase functions but all other atmospheric parameters.

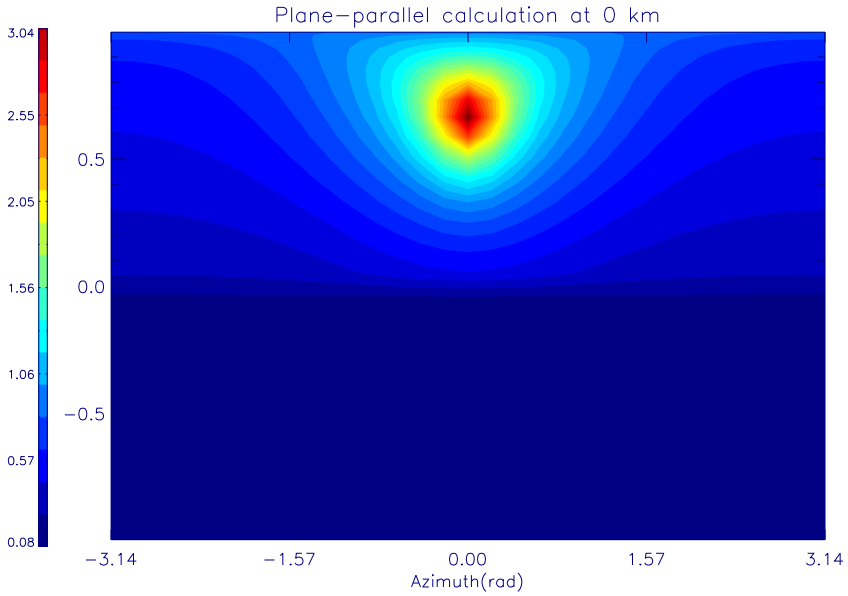

FIGURE 5.5: Plane–parallel calculation for Titan's atmosphere at solar zenith angle = $56°$.

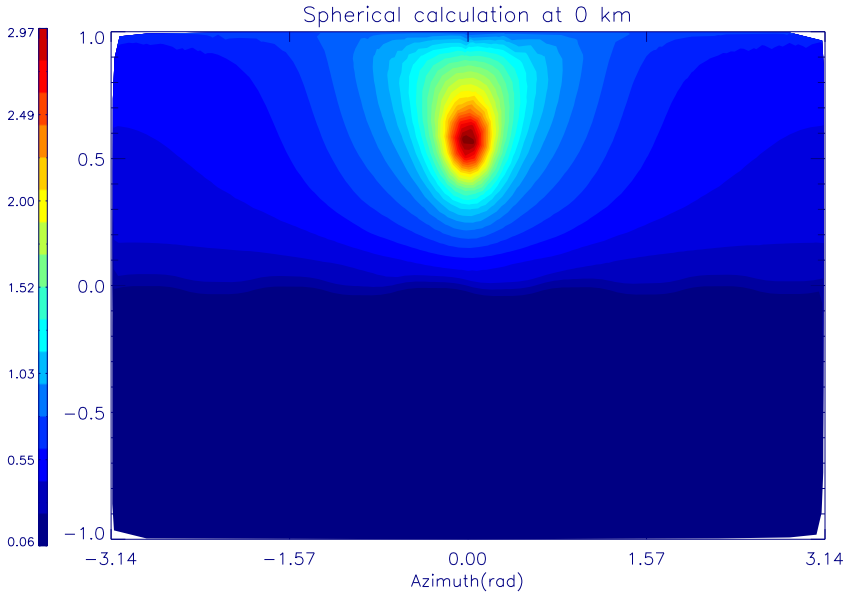

FIGURE 5.6: Spherical calculation with large radius ($r = 1000 * R_{titan}$) for Titan's atmosphere at solar zenith angle = $56°$.

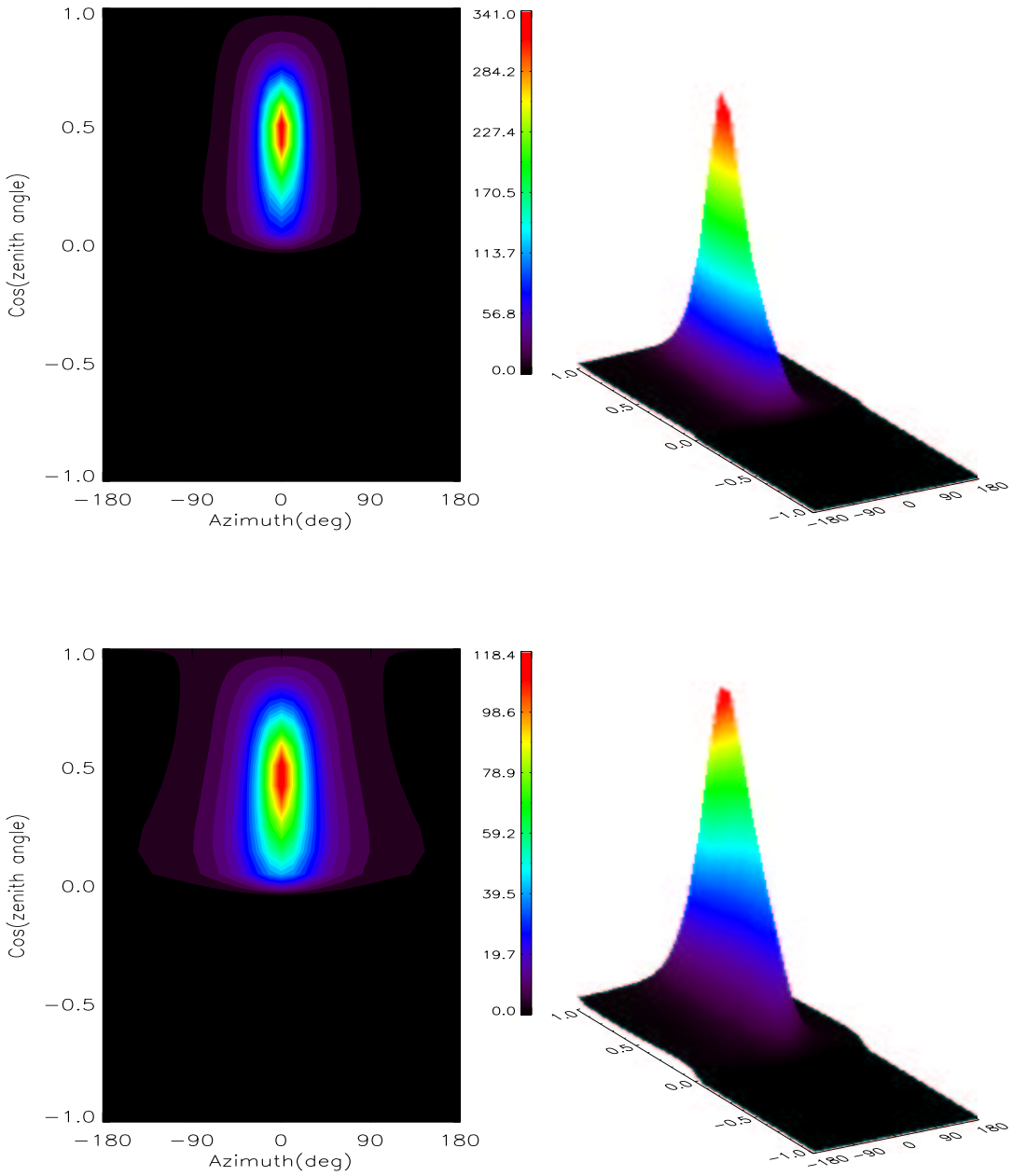

FIGURE 5.7: The diffuse downward intensity I[$\mathrm{W\,m^{-2}sr^{-1}}\mu\mathrm{m^{-1}}$] as seen from the Martian surface for two wavelengths, 443.6 nm (top plot) and 965.0 nm (lower plot) from plane–parallel approximation. The Sun is 30° above the horizon.

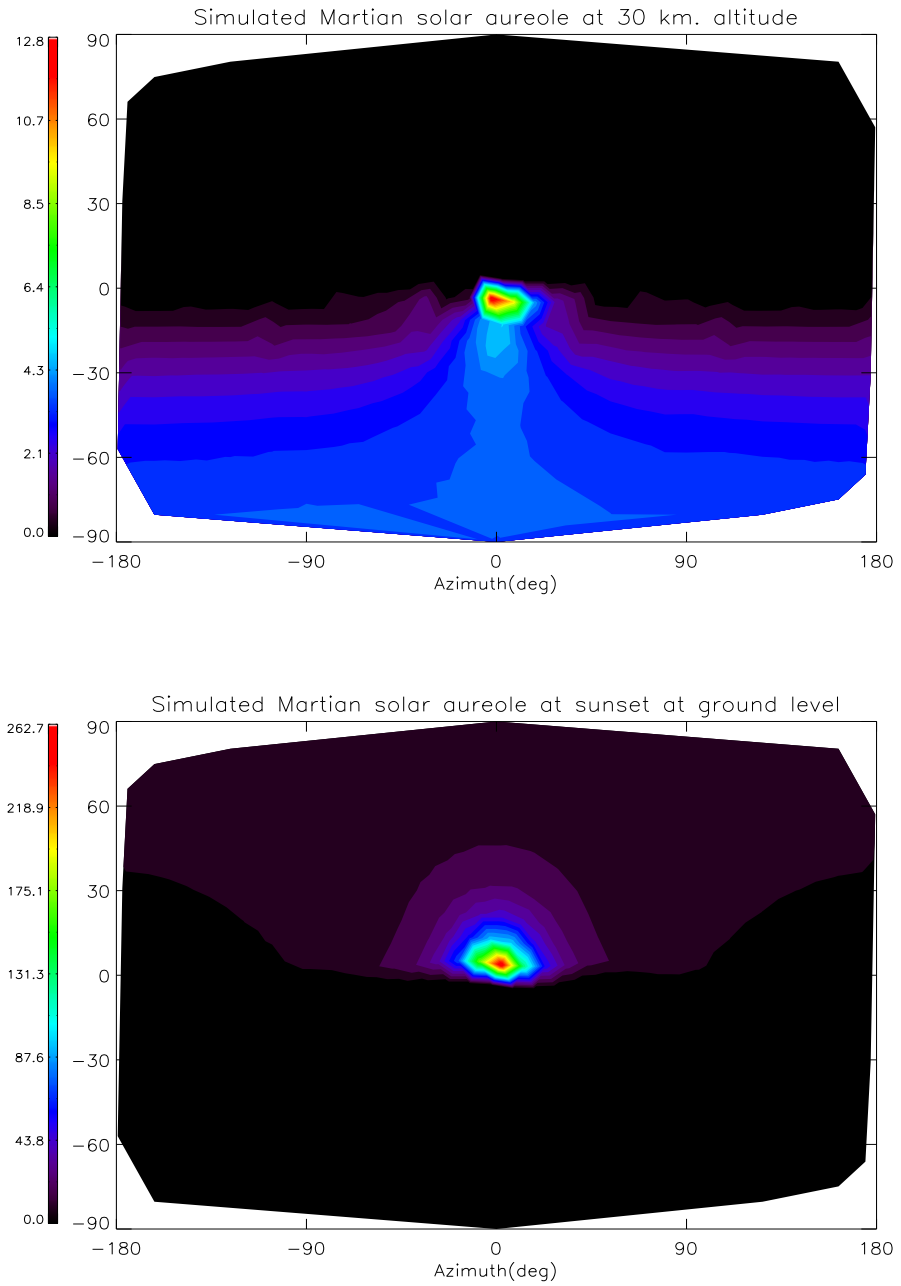

FIGURE 5.8: The diffuse intensity I [W $\mathrm{m}^{-2}\mathrm{sr}^{-1}\mu\mathrm{m}^{-1}$] for 443.6 nm as seen from the top of Mars atmosphere (top plot) and at ground level (lower plot) from spherical calculation.

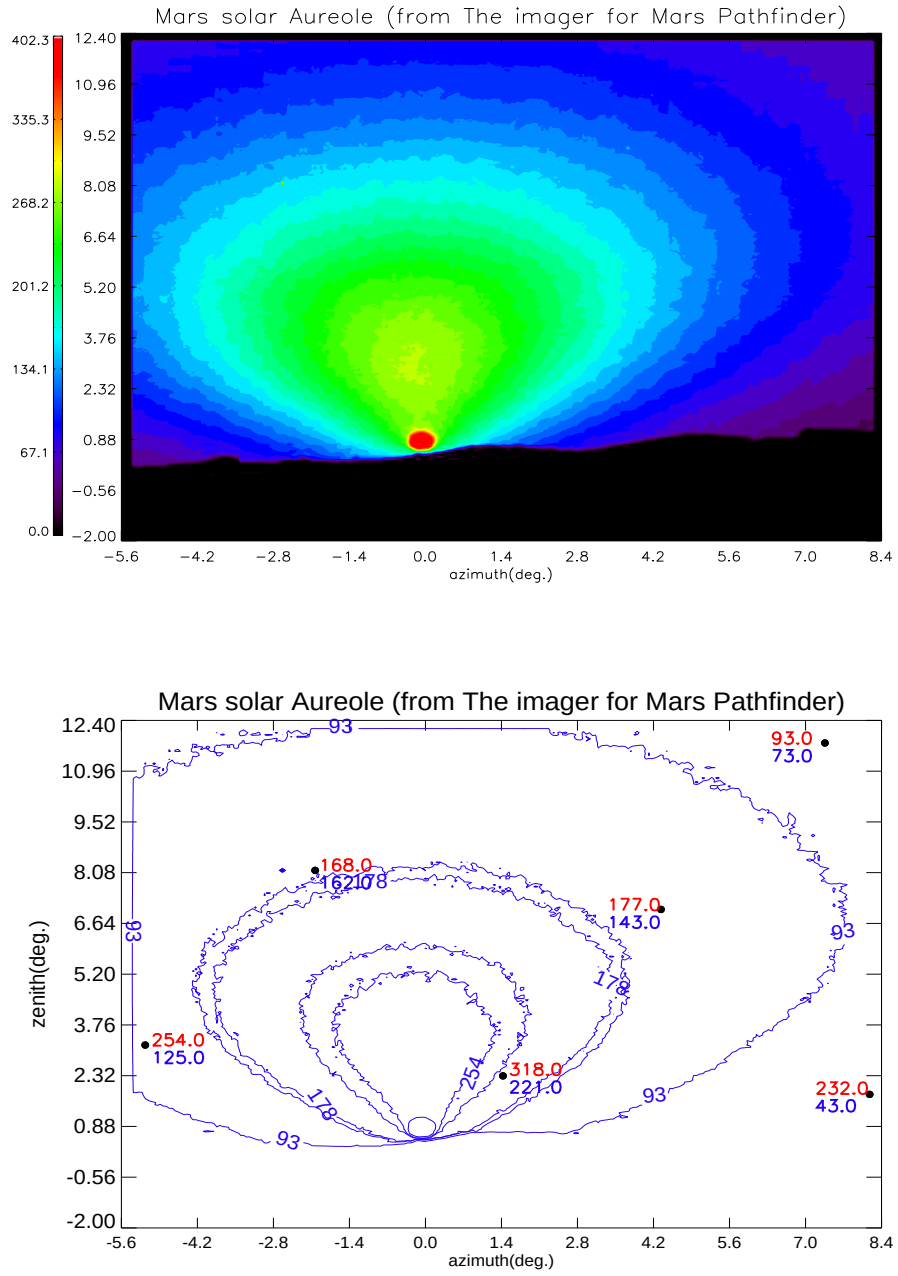

FIGURE 5.9: Diffuse intensity I [W $m^{-2}sr^{-1}\mu m^{-1}$] as seen from the Martian surface at 443.6 nm (top plot) and simulated intensity from our model (red numbers, lower plot) compared to measured radiances mapped to model pixels (blue numbers, lower plot).

Chapter 6

Titan

This chapter presents a synthesis of the properties of Titan's atmosphere as they are understood at the present time. Its purpose is two fold, first to provide a bridge between the previous chapters and relate the theory and modeling of radiative transport with the final goal of this thesis work which is the modeling of Titan's atmosphere. Second, to highlight the relation of this work with the scientific goals to be accomplished by the arrival of *Cassini-Huygens* mission to Titan.

6.1 Introduction

Titan is Saturn's largest moon. It orbits at a distance of about 1.2 million km from its primary, or some 20.6 Saturn radii. This could be compared with Ganymede, which is about 1.0 million km from Jupiter.

Titan was discovered by Huygens in 1655, but it was not until the present times that it has become the object of a serious scientific investigation. After Solá's doubtful claims of having observed an atmosphere around Titan in 1908 (doubtful because he had claimed the same thing for some Galilean satellites), Sir James Jeans decided in 1925 to include Titan and the biggest satellites of Jupiter in his theoretical study of sscape processes in the atmospheres around the solar system objects. Its results showed that Titan could have kept an atmosphere in spite of its small size and weak gravity if low temperature conditions, that he evaluated to be between 60 and 100 K had prevailed.

In this scenario, a gas of molecular weight higher than or equal to 16 could not have escaped Titan's atmosphere since the satellite's formation. The constituents which could have been present in non-negligible quantities in the mix of gas and dust particles that condensed from the solar system and which, at the same time, satisfies Jeans' criterion are: ammonia, argon, neon, molecular nitrogen and methane. Ammonia (NH_3) is solid at the estimated Titan temperature and could therefore not contribute substantially to its atmosphere. The others, however, are gases within the same temperature range. Methane (CH_4), unlike argon, neon and molecular nitrogen, exhibits strong absorption bands in the infrared which makes it relatively easy to detect.

In 1944, Gerald Kuiper discovered two absorption bands of methane at 6190 Å and

7250 Å on Titan, from which he derived an estimate of 200 m-amagats for the amount of methane on Titan. Limb darkening was finally unambiguously observed in 1975, suggesting an optically thick atmosphere. About the same time in 1975 Trafton found unexpectedly strong absorption in the $3\nu_3$ methane band at 1.1μm, indicating either a methane abundance at least ten times higher than that inferred by Kuiper or a broadening of the CH_4 bands induced by collisions with molecules of another yet undetected but quite abundant gas in the atmosphere.

In 1973, observations of the satellite's albedo and polarization of the reflected light had confirmed the presence of cloud particles up to high altitudes. Theoretical considerations suggested that clouds of condensed CH_4 and photochemical fog of more complex condensates might be both present, the latter arising as a result of methane photolysis at ultraviolet waveleghts. The fragments combine to produce polymers which condense to form oily droplets. Something similar happens on Earth in the photochemical smog generated by terrestrial road traffic. Evidence has been found in Titan's thermal emission spectrum of not only CH_4, but also C_2H_6 (at 12.2μm), C_3H_3D (at 9.39μm), C_2H_4 (at 10.5μm) and C_2H_2 (at 13.7μm).

Mass	1.346×10^{23} kg
Equatorial radius	$2,575$ km
Mean density	1.88 g/cm^3
Mean distance from Saturn	$1,221,850$ km
Orbital period	15.945 days
Rotational period	15.945 days
Mean orbital velocity	5.58 km/sec
Orbital eccentricity	0.0292
Orbital inclination	$0.33°$
Escape velocity	2.65 km/sec
Visual geometric albedo	0.21
Magnitude	8.28
Mean surface temperature	94 K
Atmospheric pressure	1496 ± 20 mbar

TABLE 6.1: Titan physical data from *Voyager 1* obsevations

Before the *Voyager* encounter there were divided opinions whether methane or nitrogen was the principal component of Titan's atmosphere. Danielson et al. (1973), and Caldwell (1977) favoured methane as the main component with about 90% of the atmosphere and predicted surface conditions of $T = 86$ K at a pressure of 20 mbar. Lewis (1971) and Hunten (1977) expected that dissociation of ammonia would have produced molecular nitrogen in large quantities and concluded that the surface temperature and pressure would be quite high (200 K and 20 bar).

Just prior to the *Voyager* encounter, Jaffe et al. (1980) measured the emission temperature of the surface using the newly developed VLA (Very Large Array). Based on this, they suggested the possibility of oceans of methane, an idea which was ahead of its time. Trough popular for a while, the idea of one ocean soon run into trouble on grounds

of tidal dissipation, which should have dumped out the marked eccentricity of Titan's orbit (Dermott & Sagan 1995) and radar observations which tend to discount a smooth surface. The idea was finally abandoned, along with any expectation of thick, extensive methane clouds, when the relative transparency of Titan's aerosol layers at some infrared wavelengths was discovered and features could be observed on the surface.

6.2 Titan's atmosphere

6.2.1 Atmospheric components

Most of our knowledge about the atmospheric composition of Titan's atmosphere, has been inferred mostly from *Voyager* infrared observation made in 1981. In addition, ground-based IR and microwave observations have permitted the retrieval of the vertical distributions of some atmospheric components or detection of new species.

The major constituent of Titan's atmosphere is molecular nitrogen (N_2) with a mole fraction of at least 90%. The solar occultation experiment of the ultraviolet spectrometer (UVS) of *Voyager 1* observed directly molecular and atomic nitrogen in the upper atmosphere (Broadfoot et al. 1981), while the radio occultation experiment (RSS) and the infrared interferometer spectrometer experiment (IRIS) determined a mean molecular weight of $m \approx 28.6$ amu in the lower atmosphere, indicating also the dominance of N_2 (Lindal et al. 1983).

Compound	Formula	Mixing ratio
Nitrogen	N_2	$0.90 - 0.99$
Argon	Ar	< 0.06
Methane	CH_4	$0.017 - 0.045$
Hydrogen	H_2	0.001
Ethane	C_2H_6	1.3×10^{-5}
Acetylene	C_2H_2	3×10^{-6}
Propane	C_3H_8	5×10^{-7}
Ethylene	C_2H_4	1.5×10^{-7}
Propyne	C_3H_4	5×10^{-9}
Diacetylene	C_4H_2	1.4×10^{-9}
Hydrogen cyanide	HCN	1.7×10^{-7}
Cyanoacetylene	HC_3N	Detected
Acetonitrile	CHC_3CN	Detected
Carbon dioxide	CO_2	1.4×10^{-8}
Carbon monoxide	CO	5×10^{-5}

TABLE 6.2: Chemical composition of Titan's atmosphere (adapted from Gautier, 1992 and Raulin et al., 1995)

Argon has never been detected in Titan's atmosphere; its presence is speculated because of the fact that the mean molecular weight measured in the atmosphere can be

substantially higher than 28 amu (Samuelson et al. 1981). Argon is the only constituent heavier than N_2 and cosmologically abundant in the form of ^{36}Ar and ^{38}Ar and it would not condense in Titan's atmospheric conditions (Owen 1982). The estimated upper limit for the presence of argon is around 10% (Samuelson et al. 1997). Apart from argon, methane (CH_4) is the most abundant constituent. The detection of its strong absorption bands by Kuiper (1944) was the first certain confirmation of the existence of Titan's atmosphere. Its mole fraction is a few % in the lower atmosphere. Updated results from a re-analysis of Voyager's IR data by Coustenis & Bezard (1995) concerning the stratospheric abundance of methane (Courtin et al. 1995) set it between 1.7% and 4.5%, while the tropospheric value is poorly constrained.

The third most abundant detected atmospheric constituent, H_2, is present only as a few tenths of a percent (Samuelson et al. 1981, Toon et al. 1988, Courtin et al. 1995). In Table (6.2), we adopt the most recent value derived from *Voyager* data reanalysis (Courtin et al. 1995).

Furthermore, Titan's atmosphere is characterized by a variety of hydrocarbons, nitriles and oxygen compounds. HCN has been detected at mm wavelengths by ground-based observations, providing a disc-averaged vertical distribution in the stratosphere (Tanguy et al. 1990). HC_3N has also been detected at mm wavelengths by Bézard et al. (1992). Bézard et al. (1993) have detected the acetonitrile CH_3CN for the first time.

Two O–compounds have also been detected: CO (Lutz et al. 1983) and CO_2 at a very low mole fraction (Coustenis & Bezard 1995). In Table 6.2, we adopt the value of Lutz et al. (1983) for the tropospheric abundances.

Recently, a small amount of water vapour was detected by ISO (Infrared Space Observatory) in the infrared spectrum (Coustenis et al. 1998). H_2O is thought to enter Titan's atmosphere by meteorite bombardment or by sputtering of water ice from neighbor satellite or Saturn's rings.

6.2.2 Thermal structure

Analogously to Earth's atmosphere, Titan's atmosphere is subdivided into regions defined by the temperature variations with height or pressure. These two characteristics of the atmosphere are interconnected via the hydrostatic law. On both bodies, the mean temperature profile is characterized by temperature inversions which are regions where the temperature increases with altitude, while the opposite i.e. temperature decreases with altitude occurs between these regions. This is a consequence of a region of heating in the middle atmosphere, the ozone layer in Earth's case and the deep haze layer in Titan's case. Both of these regions absorb solar energy and heat the region producing a local temperature maximum (Fig. 6.1).

The regions between the temperature maxima and minima, which exist for the same basic physical reason, are given corresponding names in both atmospheres, however the analogy is not so precise, since Titan's atmosphere is more extensive than Earth's. In fact, the extend of Titan's atmosphere is comparable with its radius ($1/5$ ratio).

Our current knowledge about the thermal structure of Titan's neutral atmosphere is based mainly on three experiments performed during the *Voyager 1* flyby. The refractivity data of RSS yielded the vertical temperature profile at two locations near the equator

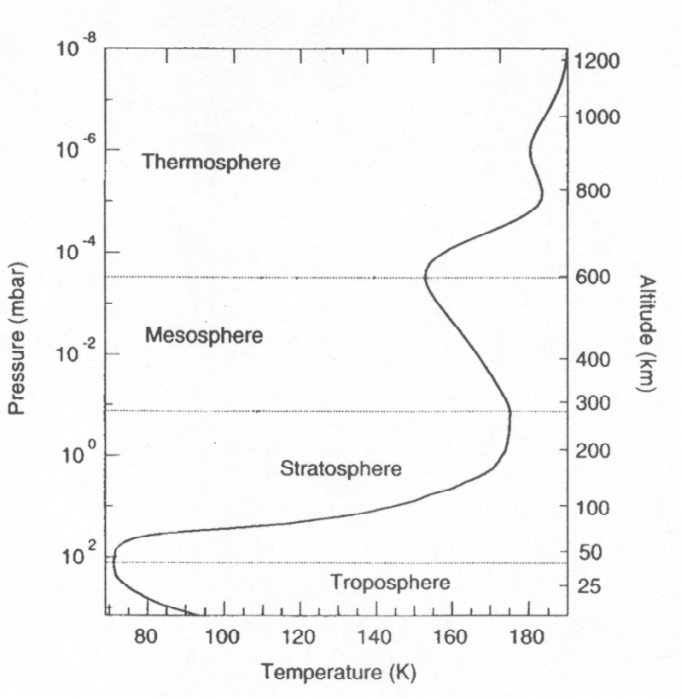

FIGURE 6.1: Vertical temperature profile of Titan's atmosphere. *(Recommended engineering model by Yelle et al. (1997) developed for the preparation of the Huygens mission.)*

for altitudes below 200 km (Lindal et al. 1983, Lellouch et al. 1989). The latitudinal temperature structure at two stratospheric pressure levels was determined from the emission of the methane ν_4 band centred at $1304\mathrm{cm}^{-1}$ (7.7μ) measured by IRIS by means of different radiative transfer models (Flasar et al. 1981, Flasar & Conrath 1990, Coustenis & Bezard 1995). Similar data where obtained also for the tropopause and near surface, but the exact sampled altitude range remained somewhat uncertain (Samuelson et al. 1997). The thermal profile of the outer atmosphere above 500 km was inferred by the solar occultation experiment of UVS (Smith et al. 1982). The engineering model for Titan (Yelle & et al. (1997), Fig. 6.1) for the preparation of the *Huygens* mission was constructed by matching the RSS, UVS and IRIS data sets considering other recent observational constrains on gas abundances. Titan's atmosphere can be divided into the *troposphere* (0 - 43 km), *stratosphere* (43 - 300 km), *mesosphere* (300 - 565 km) and *thermosphere* ($>$ 565 km) according to the engineering model used for the *Huygens* mission.

Troposphere

Much of the electromagnetic radiation emitted by the Sun and reaching a planet is at wavelengths in or near the visible part of the spectrum. Aerosol layers scatter photons and reflect a portion of the radiation back into space, some of it is absorbed by haze, clouds if present and by atmospheric gases. The rest of the energy, about 10% reaches Titan's ground level where it is absorbed. The lower atmosphere is then heated by the ground and becomes unstable against convection.

Convective instability exists in the lowest part of any optically thick atmosphere. Since the temperature decreases with altitude, the warmer air lying under colder air is unstable and so it rises while the colder air sinks. On Earth, the region where this turning happens is known as the *troposphere*. The upper boundary is the level where the overlying atmosphere is of such a low density that a substantial amount of radiative cooling to space can occur in the thermal infrared region of the spectrum. At this level, called the *tropopause*, radiation cools raising air so efficiently that the temperature tends to become constant with altitude and convection stops.

On Titan, temperature falls with height from the ground to about 40 km. so this level is often refereed as the *tropopause*. However the level in which convective equilibrium is replaced by radiative equilibrium may be somewhat lower than 40 km.. Based on the temperature profile produced from the *Voyager* radio occultation experiment, we will define the *tropopause* as the region from the surface to the first temperature minimum; however, until Titan's atmospheric temperature structure has been characterized globally, we are probably stuck on the knowledge of where this overturn occurs.

Stratosphere

The *stratosphere* on Titan is the region from about 40 to 300 km altitude where temperature increase with height, i.e. the region between the first temperature minimum and the first maximum above the surface. On Earth the *stratosphere* is usually the region where the convection stops and the air forms layers which tend to be stable, i.e. the atmosphere is stratified. This due to the absence of enough absorption above the *tropopause* to stop the emitted photons from reaching space causes the lapse rate to tend to zero. On Titan, the corresponding effect is due to the absorption and thermalization of solar–UV radiation by different gases and aerosols in the atmosphere. The temperature is raising from 70 K at around 40 km of altitude (where the first inversion occurs) up to about 180 K around 300 km. In general, we can say that the mean stratospheric temperature is about 70 K in Titan.

Mesosphere

In the *mesosphere*, the temperature drops from 178 K at the *stratopause* to 135 K at the *mesopause*. In the upper atmosphere, the major source of heating is the absorption of thermal radiation by the vibration–rotation bands of C_2H_6 followed by solar IR and UV radiation absorption mainly by CH_4 while the absorption of thermal radiation by CH_4 and C_2H_2 contributes to cooling. In the lower *mesosphere* the absorption by CH_4 and C_2H_2 conversely becomes a major source of heating, followed by the absorption of solar–IR by CH_4, while C_2H_6 becomes thermal coolants. In the whole upper atmosphere the absorbing gases are in non–LTE (local thermodynamic equilibrium) except for the rotational transitions for HCN in the *thermosphere*.

The thermal structure of the lower atmosphere is controlled by the competition of anti–greenhouse effect by stratospheric haze and greenhouse effect by tropospheric gases in the atmosphere (McKay et al. 1991). Titan's anti–greenhouse effect is unique in the solar system Titan's organic haze absorbs the majority of the incoming visible solar light

while it is transparent for thermal radiation emitted by the surface and atmosphere.

Thermosphere

In the *thermosphere*, the temperature raises from 135 K at the *mesopause* to 175 K. The temperature is determined mainly by heating due to absorption of EUV radiation by N_2 and cooling by rotational transitions of HCN. Moreover, magnetospheric N^+ ions, cause a temperature raise of up to 30 K by sputtering when Titan is located within Saturn's magnetosphere (Lammer et al. 1998).

6.3 Aerosols and condensates : Titan's haze layer

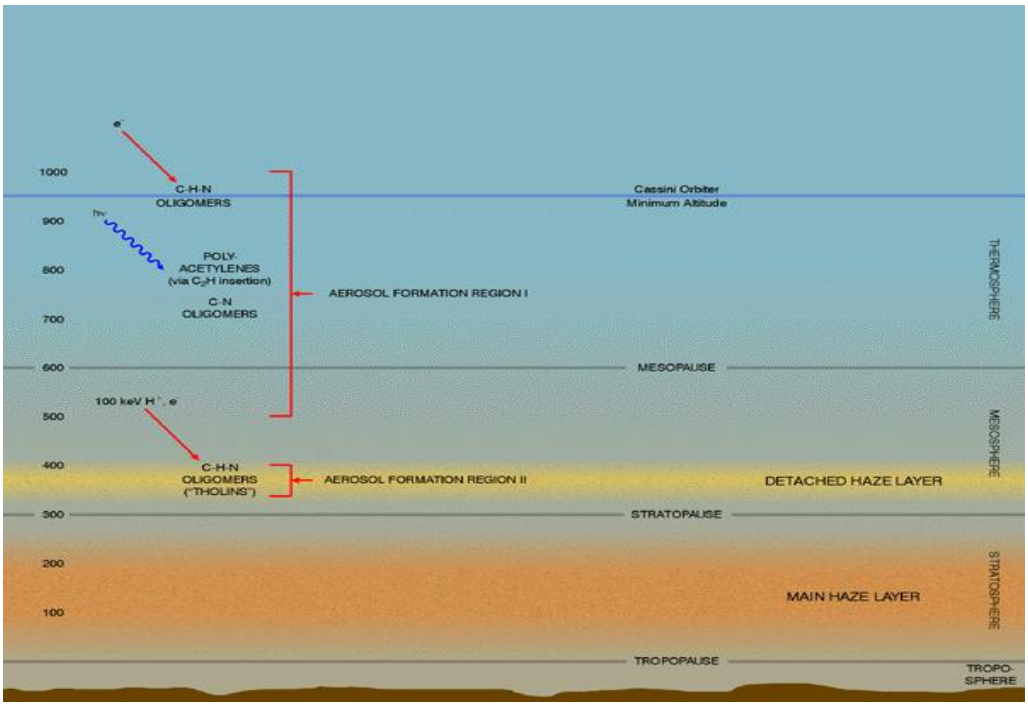

FIGURE 6.2: This figure illustrates Chassefière & Cabane (1995) model of Titan haze formation. (Source: Cassini INMS.)

In the previous section, we discussed the structure and composition of the atmosphere of Titan in terms of gases present. However, this description is incomplete since observations have shown the existence of small particles or aerosols, which form extensive layers of haze and cover the entire atmosphere. The presence of aerosols is due to the existence of complex chemistry and low temperatures prevailing on Titan which almost guarantees that some species will condensate.

The haze on Titan is often described as a photochemically produced smog, and it extends very high in the atmosphere. The products of the photo–dissociation of nitrogen and methane are thought to recombine and eventually produce large molecules which will

condense to form stratospheric haze layers further down. If this process continues long enough, some of the higher order products will become so abundant that sooner or later they are bound to stick together and form large particles which fall out of the stratosphere.

Laboratory experiments have been used in a effort to simulate the production of the haze material from methane and nitrogen. The optical properties of this organic matter, often called *tholin*, produced in these experiments, match the general features of the Titan geometric albedo spectrum inferred from observations. They can also fit detailed microphysical and radiative simulations with spherical and, more realistically, irregular or compound particles. The fact that laboratory produced *tholin* produces a good analog for Titan's haze supports the idea that the haze is composed of refractory organics of photochemical origin.

Titan's detached haze layer consists of aerosols formed from polyacetylenes and perhaps from $C - N$ oligomers, photo–chemically created between 500 and 800 km. The main haze layer, on the other hand, is constituted by $C - H - N$ oligomers produced between 350 and 400 km by reactions initiated by the influx of energetic particles from Saturn's magnetosphere. Such $C - H - N$ oligomers (*tholin*) may be formed at higher altitudes as well, and thus may also contribute to the detached haze layer.

6.3.1 Titan's haze in the visible

Half a century ago, Earth–based observations of Titan revealed the presence of methane absorption bands in the infrared spectrum and indicated the presence of a dark-orange or brown aerosol haze layer in the upper atmosphere. The presence of methane, which was known to readily photolyze, and the colour of the cloud deck, let to the conclusions that organic aerosols were produced in the atmosphere.

The highest spatial resolution images of Titan obtained from *Voyager* in 1990, especially photographs of the limb, confirmed this basic picture, showing an optically thick haze deck composed of several distinct layers in the stratosphere completely hiding the surface at visible wavelengths (Fig. 6.3). The uppermost of these is very tenuous and shows up primarily in the ultraviolet region of the spectrum. In *Voyager* observations of the high phase angle brightness, particles are observed as high as 500 km above the surface with an extensive detached haze layer occurring from 300 to 350 km. The visible limb of the planet, where the vertical haze optical depth is 0.1 is about 220 km above the surface. The haze controls the propagation of sunlight in Titan's atmosphere and thereby influences the temperature of the atmosphere and the surface (Coustenis & Taylor 1999).

6.3.2 Titan's geometric albedo

The geometric albedo of Titan as a function of wavelength was the first and remains a very useful data set for understanding the nature of the haze. Fig.(6.4) shows a recent data set as compiled by Karkoschka (1994, 1998) from 0.3-1 μm, together with the IUE data from McGrath et al. (1998), from 0.2-0.3 μm and data for wavelength beyond 1 μm from Coustenis & Bezard (1995). The figure also shows the processes that determine the albedo in each wavelength range.

In the UV, the geometric albedo is determined by the relative opacity of the dark absorbing haze material and the bright Rayleigh scattering of the gas (Courtin et al. 1991). In the visible, the albedo is determined entirely by the properties of the haze, which is optically thick at those wavelengths. In the visible, gas opacities are negligible and the haze completely obscures the surface. At longer wavelengths ($> 0.6\mu$m), the scattering extinction efficiency of the particles decreases due to the increase ratio of wavelength to particle size. Thus at wavelengths larger than 0.6μm, the haze becomes progressively transparent and the surface properties influences the observed albedo (McKay et al. 1989). However, near 0.8 μm CH_4 absorption features become prominent. Thus in this spectral region the albedo is determined mainly by the CH_4 amount and surface properties and to a lesser degree by the haze (McKay et al. 1989, Coustenis & Bezard 1995).

Ground based spectroscopic observations in the near-IR methane windows between 0.9 and 2.5 μm by Griffith (1993), Lemmon et al. (1993, 1995), Coustenis & Bezard (1995) show a time variability of albedo respect to the orbital phase around Saturn. This revelead that Titan is phase-locked with Saturn, and that the haze is sufficient translucent in the IR-windows to reveal a noticeable longitudinal variations in surface albedo. The geometric albedo of Titan has also undergone small oscillations over the past two decades, with variations for $10 \pm 1.3\%$ at 0.47 μm and $7 \pm 1.3\%$ at 0.55μm which correlate with the seasonal cycle (Lockwood 1977, Lockwood & Thompson 1979, Lockwood et al. 1986). These variations appear to be atmospheric in origin, and suggest that Titan's haze varies regularly with season.

6.3.3 Imaging and photo–polarimetry

Voyager imaging of Titan, in the visible range, has shown a marked hemispherical asymmetry in the brightness of the haze (Sromovsky et al. 1981). When *Voyager* observed Titan (northern spring), the southern hemisphere has an albedo about 25% brighter than the north at blue wavelengths, with the interhemispheric contrast smaller at green and violet wavelengths. Lorenz et al. (1997) suggested that a change in particle number density between 70 and 120 km could explain the observed asymmetry.

Data from *Pioneer 11* and *Voyager* photo–polarimetry (Tomasko & Smith 1982, West et al. 1983) showed a large positive polarization at 90° phase angle. This requires particles, if they are spherical in shape with radii no larger than 0.1μm. However, *Voyager* observations (Rages & Pollack 1983) of the brightness of Titan at high phase angle require particles that are at least 0.2μm and probably as big as 0.5μm in radius. Thus Titan's haze cannot consist of simple spherical particles, and it is now believed that they are non-spherical aggregates of small spherical monomers (West & Smith 1991, Rannou et al. 1995, Karkoschka & Lorenz 1997, Tomasko et al. 1997). Several microphysical models have been developed to understand the composition and optical properties of Titan' haze. These models and our own approach to this problem is highlighted in the next section.

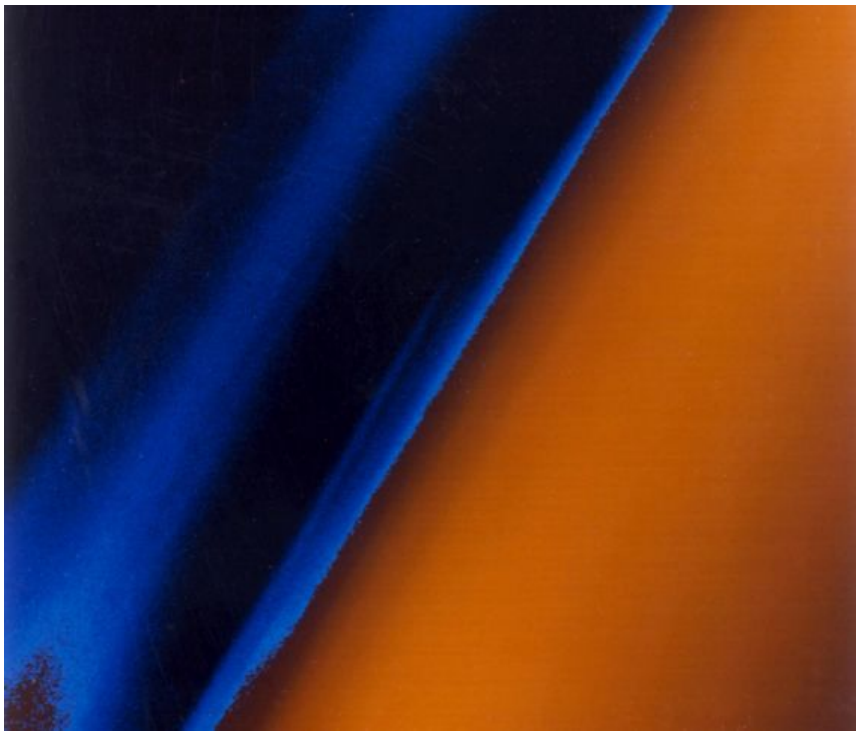

FIGURE 6.3: The *Voyager 1* spacecraft's historic tour of the outer Solar System took it past Saturn in late 1980. On November 12, 1980, *Voyager 1* recorded this view looking across the edge of Titan (Credit:Voyager Project, JPL, NASA)

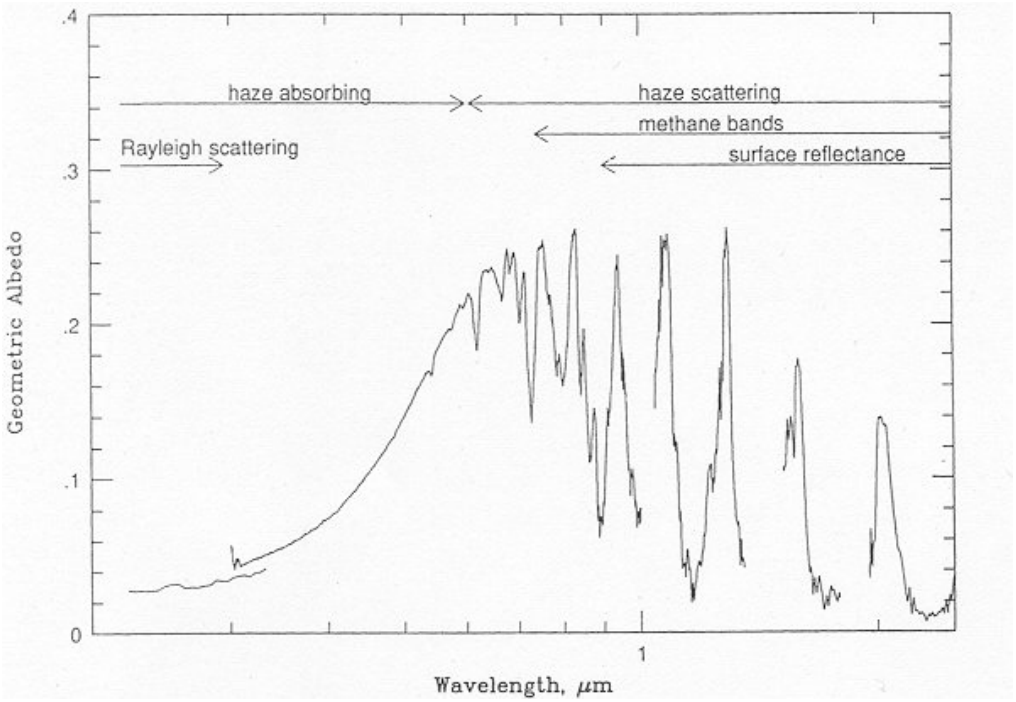

FIGURE 6.4: The geometric albedo of Titan from International Ultraviolet Explorer $0.2 - 0.3\mu$m and ground based observations.

6.4 Microphysical models of Titan's aerosols

A variety of microphysical models have been developed to simulate the characteristics of the haze on Titan. The first estimates of haze production made before the *Voyager* results by Podolak & Bar-Nun (1979) suggested a production rate of $3.5 \times 10^{-14} \mathrm{gcm}^{-1}\ \mathrm{s}^{-1}$ based on the rate of CH_4 photolysis as well as on the albedo required to match the observed reflectance of Titan. Toon et al. (1980) found with a detailed microphysical model that the production rate of $35 \times 10^{-14} g\ cm^{-1}\ s^{-1}$ was necessary to fit the geometric albedo in a pure CH_4 atmosphere.

After the *Voyager* encounter it was clear that Titan's atmosphere is primarily composed of N_2 making the pre–*Voyager* estimates irrelevant. The detection of gaseous organics in the stratosphere confirmed that the haze was likely to be organic material. Yung et al. (1984) developed a photochemical model treating only the chemistry of $C_n\ (n > 4)$ species and included a series of reactions that produced hydrocarbon "polymer", their mass production rate of $2 \times 10^{-14} \mathrm{gcm}^{-1}\ \mathrm{s}^{-1}$. A similar approach was used by Lara et al. (1994).

McKay et al. (1989) used a simple monodisperse haze model based on the *Voyager* atmospheric profile to deduce that a haze production rate of $1.2 \times 10^{-14} g\ cm^{-1}\ s^{-1}$ would fit the geometric albedo from 0.3 to 2μm. Toon et al. (1992), using a very detailed aerosol model, found that a haze production rate of $1.2 \times 10^{-14} g\ cm^{-1}\ s^{-1}$ would fit the geometric albedo. Rannou et al. (1995), Rannou et al. (1997), Tomasko et al. (1997) have considered the effects of fractal geometry on the haze. Although the dynamics of the haze is quite different with fractal shapes, the inferred production rates are similar to those obtained previously. In the next sections, we discuss the current understanding of the scattering properties of Titan's aerosols as inferred from current microphysical models.

6.4.1 Scattering properties of the haze: Fractal aggregates

As said above, it is now thought that the particles in Titan's main haze layer are non–spherical aggregates. West & Smith (1991) first suggested aggregates of spherical monomers for Titan's haze. In a series of papers Cabane and co–workers (Israel et al. 1991, Cabane et al. 1992, 1993, Cabane & Chassefière 1995, Cabane & Chassefiere 1993, Rannou et al. 1993, Rannou et al. 1995, Rannou et al. 1997) have developed a sophisticated model of Titan's haze as fractal particles. A similar model has been developed by Tomasko et al. (1997).

The basis for fractal models lies in the fact that when liquid particles combine they form a new compact sphere corresponding to the combined mass, but when solid particles combine they can form a range of shapes from compact spheres to long strings of particles. A convenient parameter that characterizes the shape of these aggregates is the fractal dimension D_f. Table (6.3) gives the fractal dimension as a function of the aggregation conditions in Titan's atmosphere.

Microphysical models (Rannou et al. 1993, Rannou et al. 1995, Tomasko et al. 1997) suggest that Titan's main haze can be physically divided into two regions, a hight altitude region in which the fractal dimension is 3 (monomer growth) and the lower altitude region win which the fractal dimension is 2 (cluster–cluster ballistic growth). Typical profiles for

Growth model of the cluster	Mean free path $<$ radius	Mean free path $>$ radius
Particles combining with clusters	2.5	3
Clusters combining with clusters	1.75	2

TABLE 6.3: Fractal dimension for different aggregation models (adapted from Cabane & Chassefiere (1993))

the haze particles sizes and densities are shown in Fig. 6 of(Tomasko et al. 1997).

This can be understood following Cabane et al. (1992). Consider a photochemically active zone located at altitude z_0 and assumed to be a Gaussian as a function of altitude. At each instant the haze contains freshly produced macromolecules and larger older particles. The coagulation process between particles is more efficient of they are of different sizes. Continuous growth of the largest particles in the photochemical zone is promoted. These growing particles, roughly spherical in shape and compact (caused by ballistic particle–cluster process, with fractal dimension of $D_f = 3$), evolve into monomers which will later build aggregates.

This hypothesis was confirmed using an Eulerian microphysical model of the aerosols (Israel et al. 1991), were a given particle is followed in the course of its growth (Rannou et al. 1993). Once these monomers are sufficiently heavy they begin to fall out of the photochemical zone. The microphysical parameters z_0 (altitude of the photo–chemically active zone) and Q (photochemical production rate) may then be used to compute the size of the monomers. For $Q = 3.5 \times 10^{-14} g\ cm^{-1}\ s^{-1}$, and for altitudes $z_0 = 300, 385, 535, \text{ and, } 680\text{km}$, the monomer radii are respectively $r_m = 0.13, 0.09, 0.03, \text{ and } 0.01\mu\text{m}$. It follows then that a rather low production altitude below 450 km leads to monomer radii consistent with the optical properties of Titan (Rannou et al. 1995). Bellow the photo–chemical zone, the collisions occur without the presence of smaller particles, since they are incorporated into the monomers faster than they settle.

6.4.2 Microphysical and optical model of the Titan haze

Microphysical models are necessary to take into account the detailed structure of Titan's haze, specially the shape and the size of the particles (*tholins*), their number density and their distribution in the atmosphere. In order to predict *DISR* measurements and explore capabilities of the instrument, Rodin (2002, 2003) have developed a 1–D model of Titan haze that accounts for coagulation of *tholin* particles, their mixing and sedimentation. Tholin particles are believed to be formed in the upper layers of the atmosphere, from a coagulation process from primordial clusters of roughly nanometer size. This coagulation is a result of photolytically induced oxidation of nitrogen and hydrocarbons, specially methane in the range of altitude between 300 and 450 km. In order to estimate the scattering properties, we make use of the optical parameters of aggregate *tholins* particles calculated by Lemmon (1994), for several particle sizes. Volume absorption coefficient is added to gaseous absorption due to methane gas only.

A more detailed description of the microphysical and optical modeling of Titan haze

used here can be found in a co–authored paper Grieger et al. (2003), which is included in the bibliography. Results from that microphysical model were used in all our computations.

6.5 The Cassini–Huygens mission

The Cassini mission is designed to explore the Saturnian system and all its elements: the planet and its atmosphere, rings, magnetosphere and a large number of its moons, namely Titan and the icy satellites. The mission will pay special attention to Titan, Saturn's largest moon and the Solar System's second largest after Jupiter's Ganymede. Cassini's broad scientific aims are to:

- Determine the dynamical behaviour of Saturn's atmosphere.
- Determine the chemical composition, physical structure and energy balance of Titan's atmosphere.
- Observe the temporal and spatial variability of Titan's clouds and hazes.
- Characterize Titan's surface.
- Determine the structure, composition and geological history of Saturn's icy satellites.
- Study the structure of the rings and the composition of the rings' material.
- Study the structure, chemical composition and global dynamics of Saturn's magnetosphere.

An important aspect of the Cassini mission is studying the interaction and interrelation of the system's elements. Studying the interrelation between the rings and the icy satellites and the interaction of the satellites and of Titan's ionosphere with Saturn's magnetosphere is a key objective.

Huygens science objectives

The scientific objectives of the *Cassini/Huygens* mission at Titan are:

- To determine atmospheric composition.
- Investigate energy sources for atmospheric chemistry.
- Study aerosol properties and cloud physics.
- Measure winds and global temperatures.
- Determine properties of the surface and infer internal structure.

- Investigate the upper atmosphere and ionosphere.

Huygen's goals are to make a detailed in–situ study of Titan's atmosphere and to characterize the satellite's surface along the descent ground track and near the landing site. Following the entry phase, at the start of the descent phase and after deployment of the parachute at about 165 km. altitude, all instruments will have direct access to the atmosphere. The objectives are to make detailed in–situ measurements of atmospheric structure, composition and dynamics. Images and other remote-sensing measurements of the surface will also be made during the atmosphere descent. After a descent of about 120 to 159 minutes, the Probe will impact the surface at about 5 to 6 m/s. As it is hoped that *Huygens* will survive after impact for at least a few minutes, the payload includes the capability for making in–situ measurements for a direct characterization of the landing site surface. If everything functions nominally, the Probe batteries can provide 30 to 45 minutes of electrical energy for an extended surface science phase that would be the bonus of the mission. The current mission scenario foresees the Orbiter listening to the Probe for a full 3 hours, which includes at least a 30 minutes surface phase, as the maximum descent time is expected to be 2.5 hours. A surface phase of only a few minutes would allow a quick characterization of the state and composition of the landing site. An extended surface phase would allow a detailed analysis of a surface sample and meteorological studies of the surface weathering and atmosphere dynamics.

Descent Imager/Spectral Radiometer (DISR)

DISR is a multi–sensor optical instrument capable of imaging and making spectral measurements over a wide range of the optical spectrum (ultraviolet–infrared, 0.3–$1.64\mu m$). An important feature of Titan is its aerosols and thick atmosphere, where the temperature structure is determined by the radiative and convective heat-transport processes. *DISR* measures the upward and downward heat fluxes. An aureole sensor measures the intensity of the Sun's halo, yielding the degree of sunlight scattering caused primarily by the column density of aerosols along the line of sight. This in turn allows deduction of the aerosols' physical properties. Upward–looking radiometers will measure the solar aureole (the bright area around the Sun seen in hazy atmospheres, and caused by forward scattering by aerosols) at 550 and 939 nm. *DISR* is also equipped with a side–looking horizon instrument to image the clouds.

DISR also has the ability to address one of *Huygens* prime objectives: investigating the nature and composition of the surface. Two cameras (one visible, one infrared) looking downwards and sideways image the surface and, as *Huygens* spins slowly, build up mosaic panoramas. By recording several panoramas during the last part of the descent, it may be possible to infer the Probe's drift (if the surface is not featureless) and contribute to the wind measurements.

Titan's daytime surface brightness is about 350 times that of nigh time on Earth with a full Moon. While the surface illumination is adequate for imaging, a surface lamp will be activated a few hundred metres up to provide enough light in the methane absorption bands for spectral–reflectance measurements. These will provide unique information on the composition of the surface material.

The fist thing that can be done with these measurements is to determine at what rate the Sun is heating the atmosphere. This is done by subtracting the downward and upward fluxes. This difference at each altitude gives the amount of solar radiation being absorbed by gases and aerosols, this will provide limits to the vertical distribution of temperature.

Combinations of measurements of small angle scattering in the solar aureole, of side and back scattering and polarization, and of the extinction as a function of wavelength, all allow the optical properties of the haze particles (optical depth, single scattering albedo and the shape of the scattering phase function) to be worked out. The main aim of this thesis work is to be able to infer those properties by using our radiation model to match the properties observed by *DISR* during *Huygens* landing in 2005.

Chapter 7

Modeling Titan's atmosphere

After the *Voyager 1* flyby of Titan in 1980, several initiatives were started to promote a mission to Titan. In 1997, the *Cassini/Huygens* mission was launched and it is scheduled to reach the Saturnian system in July 2004. The *Cassini* spacecraft will deliver the *Huygens* lander to Titan in January 2005. *Huygens* six scientific instruments will make a series of measurements during it's descent. Several measurements will be carried out by the Descent Imager/Spectral Radiometer (*DISR*). We'll focus in simulated results for the Solar Aureole Imager (*SA*) sub–instrument.

As described in Tomasko et al. (1997), the *DISR* will take images and spectral measurements in different directions at various spectral ranges and spatial resolutions. The detectors of the *DISR* are a 512 x 254 CCD for the visible, two linear arrays of 132 photodiodes for the infrared and two photodiodes for the violet spectral range. Light from the fore–optics of three surface imagers (high resolution, medium resolution and side looking), two visible spectrometers (upward and downward looking) and the Solar Aureola imager (*SA*) is conducted by fiber optic to the CCD.

Herein, we carry out radiative transfer calculations for Titan's atmosphere as it would be seen by the *SA* instrument. The *SA* will take images of the solar aureole in two wavelengths – $500 \pm 35\mathrm{nm}$ and $935 \pm 35\mathrm{nm}$ – and two polarizations. We have considered only the 500 nm channel for our calculations because at this wavelength the optical thickness is higher and effects of the spherical nature of the atmosphere can be expected to be more pronounced. Our aim is to prepare for *Cassini/Huygens* arrival and use our forward model to fit the observed radiation measurements in order to retrieve information about the optical properties of the atmosphere such as scattering phase functions, single scattering albedo, extinction coefficients, gas absorption, ground properties, linear and circular polarization.

7.1 Titan atmospheric scenario

7.1.1 Microphysical and optical model of the Titan haze

Microphysical models are necessary to take into account the detailed structure of Titan's haze, specially the shape and the size of the particles (*tholins*), their number density and their distribution in the atmosphere. In order to predict *DISR* measurements and explore

capabilities of the instrument, we have developed a 1-D model of Titan haze that accounts for coagulation of tholin particles, their mixing and sedimentation. Tholin particles are believed to be formed in the upper layers of the atmosphere, from a coagulation process from primordial clusters of roughly nanometer size. This coagulation is a result of photolytically induced oxidation of nitrogen and hydrocarbons, specially methane in the range of altitude between 300 and 450 km. A more detailed description of the microphysical and optical modeling of Titan haze used here can be found in Grieger et al. (2003).

7.1.2 Setting up the atmospheric scenario

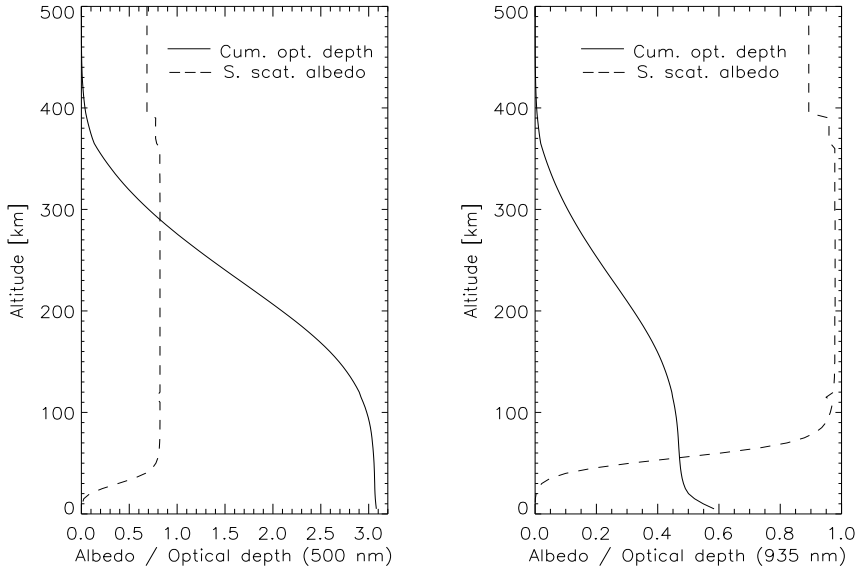

FIGURE 7.1: The cumulative optical depth and single scattering albedo of the model atmosphere as a function of altitude for the two wavelengths of the *SA*.

In our model calculation, we assume Titan's atmosphere to be vertically distributed in concentric spherical shells, i.e. the optical properties vary only with altitude. This approach can be justified by the fact that any horizontal variation of atmospheric properties in Titan's atmosphere is poorly known. This facilitates our calculations since we require only one global variable r to describe the optical properties of the atmosphere. Under this assumption, the top of the atmosphere (TOA) is set to 500 km, a planetary radius R_p of 2575 km, and within each shell, all optical properties i.e. extinction coefficient, single scattering albedo and polarized phase matrix, are assumed to be constant.

The cumulative optical depth and the single scattering albedo corresponding to the modeled aerosols are shown in Fig.(7.1) for two wavelengths, 500 nm and 935nm. The first 100 km from the top have a relatively low optical depth $\tau \sim 0.1$, the optical depth sharply increases from 400 to 100km altitude. Below that is constrained again to about $\tau \sim 0.1$. We have readily included methane absorption as described in Grieger et al. (2003).

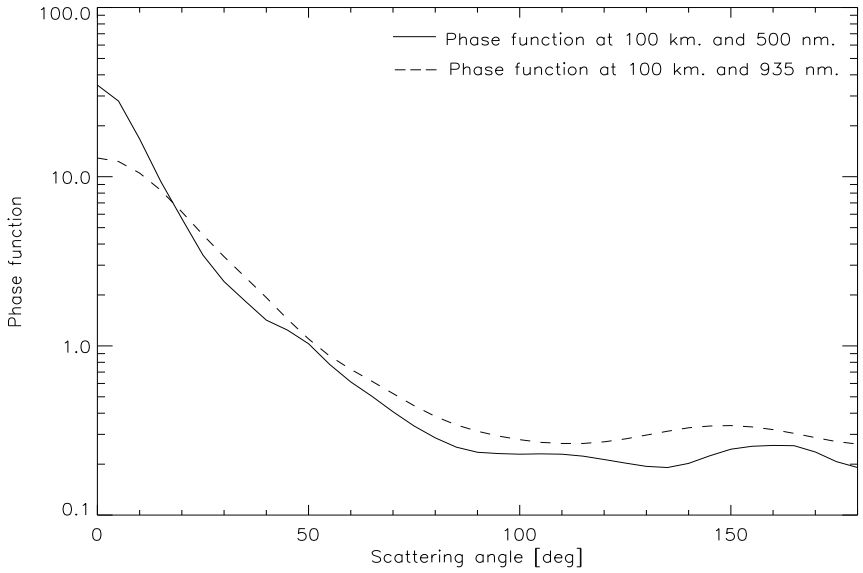

FIGURE 7.2: Phase functions example at 100 km for the two wavelengths of the *SA*.

The radiation field throughout the atmosphere is calculated for Titan's conditions with a Solar zenith angle of $\theta_0 = 50^\circ$ which is the nominal value for Huygens descent and $\theta_0 = 90^\circ$ as an additional test case for our spherical model. The solar flux is assumed to be F_0 (500nm) = 13.8 W m^{-2} μ m $^{-1}$. The atmospheric properties are for a wavelength of 500nm, which is one of the wavelengths of *Huygens SA* measurements. All computations include polarization and methane gas absorption. The ground was assumed to be Lambertian with an albedo of $\omega_{\rm g} = 0.1$, and ground temperature of 87 K$^\circ$. The vertical distribution of temperature was adopted from Yelle & et al. (1997).

7.2 Results of Titan's simulated solar aureole

The intensity and the state of polarization of a beam of light can be fully described by means of the stokes parameters *I, Q, U* and *V* (Chandrasekhar 1965, Van de Hulst 1957). Here, the local meridian plane acts as the plane of reference for the Stokes parameters. The Stokes parameter *I* represents the intensity of the beam. The parameters *Q* and *U* are related to the degree of linear polarization according to $\mathrm{LP} = \sqrt{Q^2 + U^2}/I$ and *V* to the direction of linear polarization relative to the local meridian plane $\chi = \frac{1}{2}\arctan(U/V)$.

The state of polarization of the incident radiation is given by the flux vector $\mathbf{F}$ and the flux incident at the top of the atmosphere per unit area perpendicular to the incident beam is F_0, the first element of $\mathbf{F}$. The diffuse radiation can be calculated once the incident radiation and the single scattering properties of the aerosols have been specified. Herein, we assume unpolarized radiation to be incident at the top of the atmosphere with flux $\mathbf{F} = F_0 \cdot \{1, 0, 0, 0\}$.

7.2.1 Spherical/Plane–parallel Intensity comparison

Here we present results of comparisons between intensities calculated from the spherical model with those of a plane–parallel atmosphere model. The radiance dependency at two different altitudes are examined, all the results presented here have been done for a standard Titan atmosphere as described in Sec.(7.1.2).

As stated in Herman et al. (1994), for an infinitely thick atmosphere or for a infinitesimally thin atmosphere, the scattered downward radiation at the surface is zero. An initial gain mechanism is started when light reaches the surface, multiple scattered radiation begins to accumulate until it reaches its maximum value and then decreases as a result of attenuated radiation due to the influence of other layers. Similarly, the incident solar beam, which drives the scattering process, is reduced as it penetrates deeper into the atmosphere and as a result less energy is available to enhance the scattering process.

Quantitatively, the increase in intensity as a result of increased optical depth is obtained from the integration over optical depth of the source term of Eq.(5.15), and the decrease of the transmitted intensities with the increase of optical depth is a consequence of the $e^{-\tau(s)}$ term of Eq.(5.15). Therefore, large optical depths are obtained from both large zenith angles (long geometric paths) and an optically thick atmosphere.

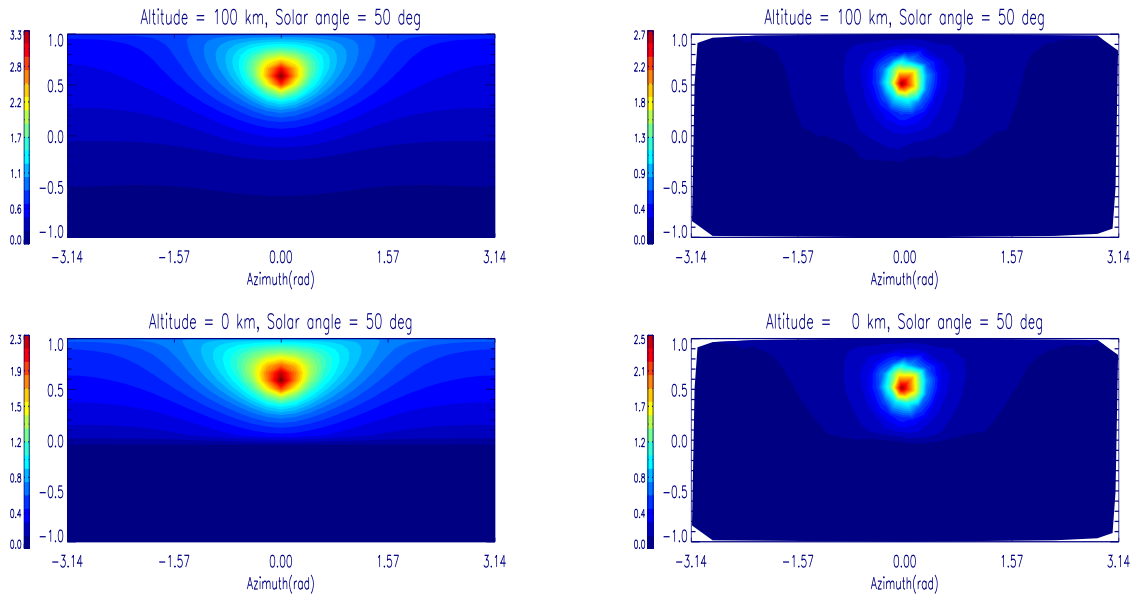

FIGURE 7.3: Intensities: Plane–parallel (left) vs. spherical (right) model at 500 nm

In Fig.(7.3) we present the full angle of view (unit sphere) radiation field for all local zenith ($cos\ \theta$, vertical axis) and azimuth angles (ϕ, horizontal axis) for two altitudes at a fixed wavelength. Excluding the case of the sub–horizon Sun, optical paths are always longer for transmitted light in the plane–parallel case. This leads to larger intensities in a plane–parallel atmosphere as compared to a spherical one, specially at low optical depths, this can be clearly seen when comparing the top two plots of the above figure. At larger optical depths, the attenuation of the direct solar beam coupled to attenuation by

subsequent atmospheric layers should show a decrease of transmitted intensity in a plane–parallel atmosphere as compared to a spherical atmosphere. Intensities for the plane–parallel case are therefore smaller at larger optical depths caused by reduced transmission. This effect can slightly be seen in the lower two plots of Fig. (7.3). The effect is not as clear in our results since the difference in optical depth between the shown altitudes is rather small (Fig. 7.1).

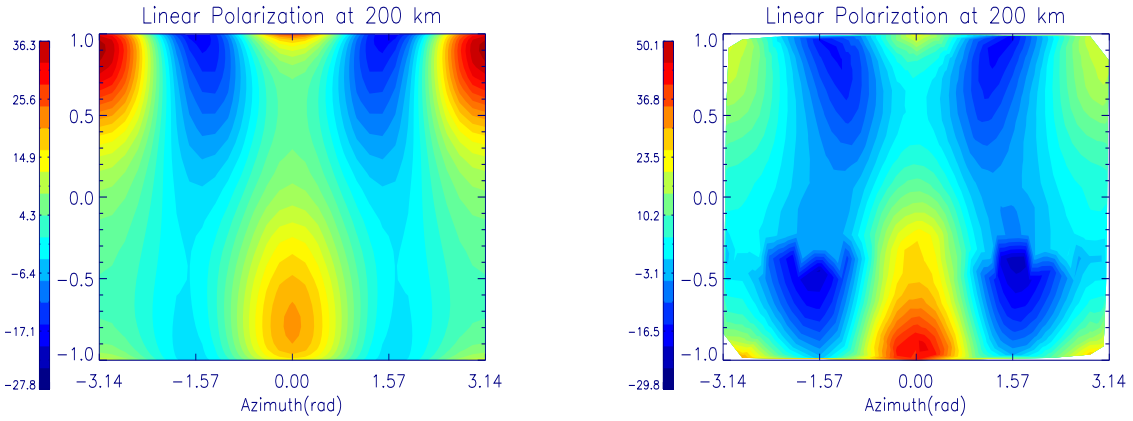

FIGURE 7.4: Linear polarization: Plane–parallel (left) vs. spherical (right) model at 500 nm

Our plane–parallel model overestimate the diffuse or multiple–scattered radiation when compared with the spherical model. This overestimation can be as high as to 18% at the center of the solar aureole, this value was estimated from our computations for the downward radiation ($\cos(\theta) < 0$). Plane–parallel models seem to spread out diffuse radiation more than in the spherical case where most of the radiation is around the aureole. This is because backscattered photons reach the TOA faster than in the plane–parallel case, this leads to a lower probability of enhanced multiple scattering from aerosols.

For the upward radiation ($\cos(\theta) > 0$), there seems to be also an increase of multiple scattered radiation, similar to the downward situation. An explanation for this is that plane–parallel layers, which are of infinite extend, will always include a surface term. Some photons reaching the surface will be reflected back and forth, increasing the amount of diffuse radiation while in the spherical case some photons will eventually leave the atmosphere and therefore do not contribute to this enhancement.

In Fig.(7.4) we show the degree of linear polarization for a fixed altitude of 200 km, just above where *Huygens* will start its measurements. Both of these calculations where done for the prescribed atmosphere as explained in Sec.(7.1.2). Both plots, plane–parallel and spherical show good qualitative and quantitative agreement, the spherical model shows a stronger backscattering peak in the principal plane i.e. $\phi = 0$ and $\phi = \pi$. This is consistent with the shape of the phase function we used at this altitude. In optically thin atmospheres the pattern of the degree of linear polarization shows the same general behaviour as the corresponding curve for $-P_2/P_1$ of the scattering matrix in Eq.(4.40); furthermore the forward scattering peak appears stronger in the spherical case than in the plane–parallel case.

7.2.2 Titan's solar aureole at 50° and 90° solar angle

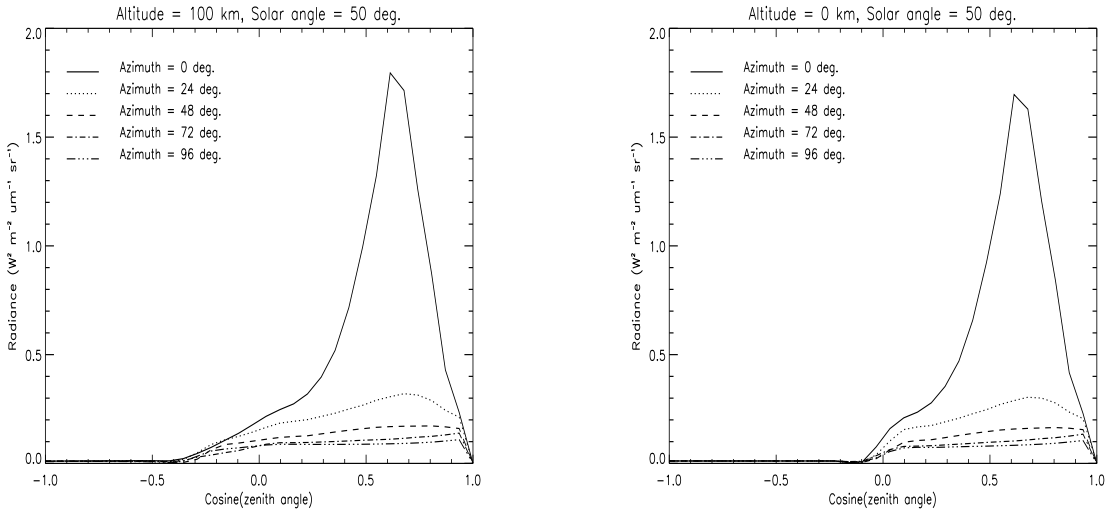

FIGURE 7.5: Variation of the Intensity field for several azimuth angles

Meridional sections of radiative intensity for solar zenith angle of 50 ° are shown in Fig.(7.5) for several azimuth angles at two altitudes. The peaks for $\phi = 0$ are higher than for other azimuth angles due to the large contribution of the radiation scattered in the forward directions i.e. $\cos\theta = 0$. This case scenario is likely to be found during *Huygens* descent since in an observation cycle, two frames are taken during one rotation of the probe, one towards the sun (slightly off the Sun to avoid the direct beam) and the other in a direction opposite to the Sun. This obviously leads to azimuthal variations during the descent and its influence is fully considered by our spherical approach.

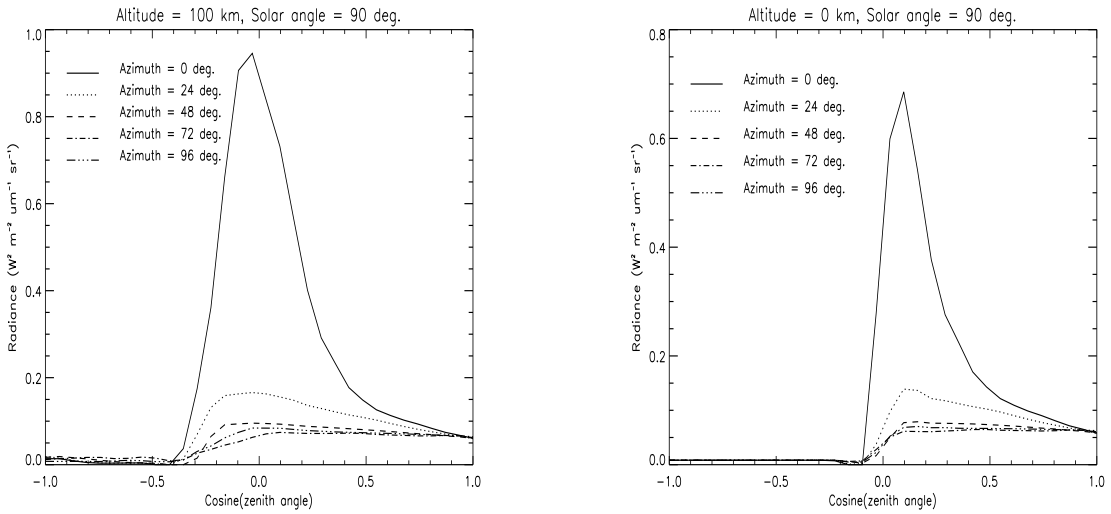

FIGURE 7.6: Variation of the Intensity field for several azimuth angles

The calculation for 90° solar angle has been done for reference purposes. Plane–parallel models cannot handle viewing angles close to the horizon therefore no direct comparisons can be made.

At 300 and 200 km (two upper plots of Fig. 7.7) the optical depths are about $\tau \sim 0.6$ and $\tau \sim 2.0$, respectively, the computed intensities are higher if compared with the lower right plot in the same picture, this difference is because, when the Sun is at the horizon, the optical path is longer at the bottom of the atmosphere so that the attenuation of the direct solar beam coupled to attenuation by subsequent atmospheric layers should show a decrease of transmitted intensity. This effect, which is clearly shown here was also discussed when comparing plane–parallel and spherical cases in the previous section. At 100 km ($\tau \sim 3.0$, lower left plot) this effect is less obvious since at this altitude we are still inside Titan's haze. Even thought, the incident solar beam is reduced at this altitude and as a result less energy is available to enhance the scattering process, the presence of the haze layer leads to slightly higher multiple scattering enhancement as compared to radiation at the lower atmosphere in which no aerosols are present (due to aerosol rainout occuring below 88 km altitude) and this portion of the atmosphere is basically transparent with an optical depth of about 0.1. We also should note here, that in the altitude range from 160 km down to the surface, the inclusion of methane gas absorption dominates over scattering by aerosols, this further contributes to the attenuation process of the direct solar beam.

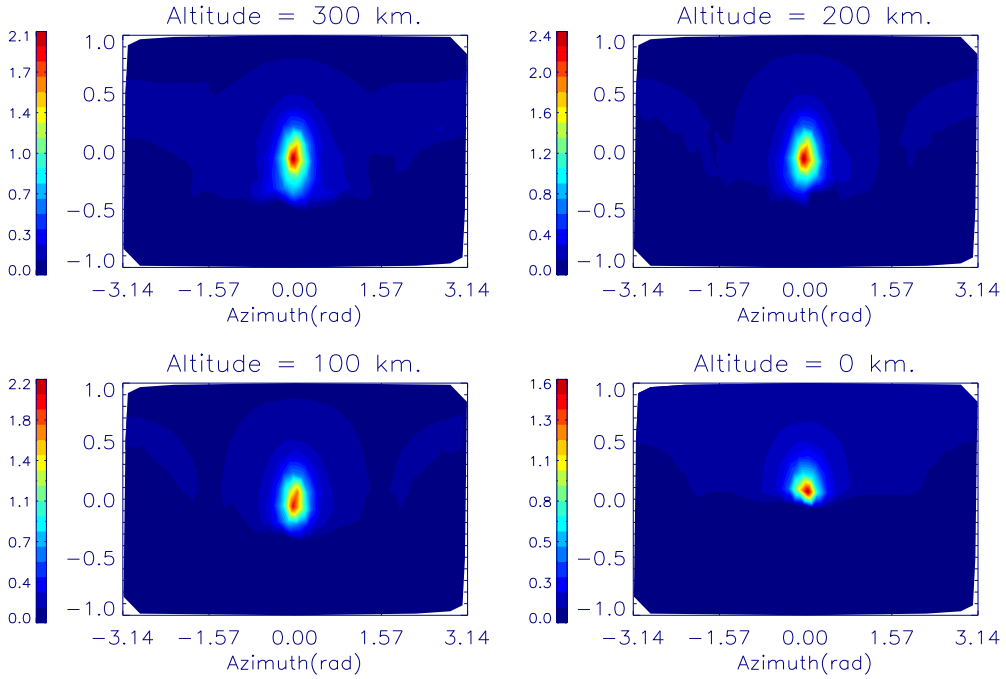

FIGURE 7.7: Internal radiation at solar zenith angles 90^{o} at several altitudes

7.3 Discussion and conclusions

Simulation results for the internal polarized radiation field of Titan has been presented. These simulations used a new microphysical model for Titan's aerosols which included methane gas absorption. The full spherical nature of Titan's atmosphere were taken into account using a combination of methods for numerically solving the radiative transfer equation for a spherical planetary atmosphere. These methods were introduced in previous chapters in which a scheme to treat the problem was proposed and later developed. A one–dimensional doubling and adding algorithm is used to generate approximate pseudo–spherical solutions from a set of prescribed solar zenith angles, this solutions together with an interpolation scheme are used to solve the polarized intensity field, for a spherical planetary atmosphere, by the method of characteristics. Plane–parallel solutions and spherical solutions were compared for a standard Titan atmosphere, both cases has shown differences in up to 18 % at the centre of the solar aureole. Plane–parallel solutions have shown to overestimate scattered radiation in some cases while underestimating others. This is not the case of a spherical atmosphere where optical paths are calculated correctly and angular variations, for all viewing directions, are included. Furthermore, polarization maps were found in good quantitative and qualitative agreement between plane–parallel and spherical approaches.

These simulations shows that within the limitations of our model atmosphere i.e., assuming that phase functions, extinction and methane gas absorption coefficients, single scattering albedo, ground albedo etc. are valid parameters for Titan's case, the radiation field inside Titan's atmosphere can effectively be reproduced for *DISR* scenario. These simulations have several implications for future data analysis of *DISR* measurements in which all atmospheric parameters, as specified above, can be more accurately retrieved by using our spherical model and comparing its computed radiances with the measured data sets.

Further testing is necessary to ensure the validity of this model. Comparison with other similar models is foreseen as a necessary step in its validation. Further enhancements can include the photo–chemistry of the upper regions of Titan's atmosphere as well the inclusion of aerosol microphysics directly into the model. Also of interest will be variations in surface albedo and variations due to ground topography. Also planned are more in depth studies of the type presented here. Future research will include investigations in sub-horizon Sun, i.e. light scattering at twilight.

Summary and conclusions

The primary purpose of this research is to develop a multi–dimensional polarized radiative transfer model for Titan's atmosphere and to validate this model with existing results where possible. A secondary aspect of the research, is to apply the model to Titan's atmosphere using atmospheric properties, as they are known to date, to demonstrate that the model produces feasible results and to show how different these results are from polarized and unpolarized plane–parallel computations. The underlying theory of radiative transfer and polarization for plane–parallel and spherical geometry as well as its numerical treatment was presented in chapters 2 to 5. Of major importance is the definition of the four–Stokes vector parameters I, Q, U and V that describe the power, level of linear polarization, plane of polarization and the ellipticity of the electromagnetic wave. These quantities are convenient because they can be measured by appropriate optical devices. The vector radiative transfer equation describes how the Stokes vector changes as energy propagates through an absorbing, emitting and anisotropically scattering medium such as a spherical planetary atmosphere.

Numerical tests and model validations were presented for both, plane–parallel and spherical cases. In the plane–parallel case, the validation was performed against existing models involving both thermal and collimated sources of radiation for emitting, absorbing and anisotropically scattering plane media containing randomly oriented axi–symmetric particles. Evaluation for I, Q, U and V Stokes components were performed. Furthermore, a pseudo–spherical treatment for the direct solar beam was introduced. Differences with the plane solution were compared and validated for limiting cases in different atmospheric scenarios. A validation was outlined for the multi–dimensional case, comparison results for polarized radiation in spherical atmospheres are not available in the literature. Therefore some limiting cases were explored and a test was performed using the large planet radius limit. An experimental comparison scenario was also proposed. The Martian atmosphere was chosen for this test. Atmospheric properties for this atmosphere was taken from existing literature and simulated radiances were compared with reported measurements from landing sites. However these prescribed tests are by no means a complete validation of our model, further comparison tests will be necessary, to ensure the functionality and robustness of this model.

Chapter 6 was mainly dedicated to the optical and atmospheric properties of Titan's atmosphere. We outlined the main components of the atmosphere and described its thermal structure. Aerosols and condensates were the central issue in our discussion. Particle production and aerosol formation are mainly responsible for Titan's haze. The particles making up the haze are the principal sources of absorption and scattering in Titan atmosphere. Understanding of the Titan aerosols leads naturally to the microphysics of the

haze. Microphysical modeling of Titan haze is necessary because aerosol scattering, in the form of scattering phase functions, are the main input to our radiative transfer calculations for Titan's atmosphere.

Chapter 7 was dedicated to modeling Titan's atmosphere. The methods outlined in previous chapters were applied to simulate Titan's internal radiation field. The field is modeled in full spherical geometry and including polarization. Since the main purpose of this thesis is to prepare for the arrival and data evaluation of the *Cassini–Huygens* mission to Titan, calculations were performed taking into consideration the geometry, frequency, angular resolution and other parameters prescribed for the DISR experiment on board *Huygens*. These results have to be seen in the context of an initial simulation exercise because the prescribed atmospheric scenario will likely change in the next few years, be it by new ground based observations or most likely by ground–breaking observations by the *Cassini* orbiter and it Huygens landing in 2005.

Finally, as in any scientific venture nothing is static and further improvement of our radiation model can be foreseen. For example, though the model is capable of performing polarized radiative transfer computations for multi–dimensional atmospheres containing oriented (as opposed to randomly–oriented) particles, this capability has not been exploited. Application to other planetary atmospheres with more complicated and realistic inhomogeneous structures than those applied in this research will improve the validity of this model. Thus in the future, more realistic atmospheres should be considered and results should be compared with observation. Another area in which the model can be improved is computational efficiency. The model is designed to run in single processor machines, but the natural parallelism of the Stokes vector suggest that the radiation field could be calculated, in principle, independent of each other. This naturally leads to a multi–processor version of our model and thus a vast gain in computer time, resources and efficiency, specially when polarization in fully spherical geometry for realistic truly 3–dimensional atmospheres is required.

Bibliography

Bézard B., Marten A., Paubert G., 1992, First Ground-based Detection of Cyanoacetylene on Titan, Bulletin of the American Astronomical Society, **24**, 953–+

—, 1993, Detection of Acetonitrile on Titan, Bulletin of the American Astronomical Society, **25**, 1100–+

Balluch M., 1996, A new numerical model to compute photolysis rates and solar heating with anisotropic scattering in spherical geometry, Ann. Geophysicae, **24**, 1–21

Broadfoot A.L., Sandel B.R., Shemansky D.E., Holberg J.B., Smith G.R., Strobel D.F., McConnell J.C., Kumar S., Hunten D.M., Atreya S.K., Donahue T.M., Moos H.W., Bertaux J.L., Blamont J.E., Pomphrey R.B., Linick S., 1981, Extreme ultraviolet observations from Voyager 1 encounter with Saturn, Science, **212**, 206–211

Cabane M., Chassefière E., 1995, Laboratory simulations of Titan's atmosphere: organic gases and aerosols, , **43**, 47–65

Cabane M., Chassefiere E., 1993, Growth of aerosols in Titan's atmosphere and related time scales - A stochastic approach, , **20**, 967–970

Cabane M., Chassefière E., Israel G., 1992, Formation and growth of photochemical aerosols in Titan's atmosphere, Icarus, S. 176–189

Cabane M., Rannou P., Chassefière E., Israel G., 1993, Fractal aggregates in Titan's atmosphere, Planet. Space Sci., **41**, 257–267

Caldwell J., Thermal radiation from Titan's atmosphere, in: IAU Colloq. 28: Planetary Satellites, S. 438–450 (1977)

Caudill T.R., Flittner D.E., Herman B.M., Torres O., McPeters R.D., 1997, Evaluation of the pseudo-spherical approximation for backscattered ultraviolet radiances and ozone retrieval, , **102**, 3881–3890

Chandrasekhar S., Radiative transfer (Dover, New York, 1965)

Chassefière E., Cabane M., 1995, Two formation regions for Titan's hazes: indirect clues and possible synthesis mechanisms, , **43**, 91–103

Cheng D.K., Field and wave Electromagnetics (Addison Wesley, New York, 1989)

Collins D.K., Bittner W.G., Wells M.B., Horak H.G., 1972, Backward monte carlo calculations of the polarization characteristics of the radiation emerging from spherical shell atmospheres, Appl. Opt., **11**, 2684–2696

Coulson K.L., 1959, Radiative Flux from the Top of Rayleigh Atmosphere., Ph.D. Thesis

Courant R., Hilbert D., Methods of mathematical physics, vol. 2 (Interscience, New York, 1962)

Courtin R., Gautier D., McKay C.P., 1995, Titan's thermal emission spectrum: Reanalysis of the Voyager infrared measurements., Icarus, **114**, 144–162

Courtin R., Wagener R., McKay C.P., Caldwell J., Fricke K.H., Raulin F., Bruston P., 1991, UV spectroscopy of Titan's atmosphere, planetary organic chemistry, and prebiological synthesis. II. Interpretation of new IUE observations in the 220–335 nm range, Icarus, **90**, 43–56

Coustenis A., Bezard B., 1995, Titan's atmosphere from Voyager infrared observations. 4: Latitudinal variations of temperature and composition, Icarus, **115**, 126–140

Coustenis A., Salama A., Lellouch E., Encrenaz T., Bjoraker G.L., Samuelson R.E., de Graauw T., Feuchtgruber H., Kessler M.F., 1998, Evidence for water vapor in Titan's atmosphere from ISO/SWS data, , **336**, L85–L89

Coustenis A., Taylor F., Titan : the Earth-like moon (World Scientific, Singapore, 1999)

Dahlback A., Stamnes K., 1991, A new spherical model for computing the radiation field available for photolysis and heating at twilight, Planet. Space Sci., **39**, 671–683

Danielson R.E., Caldwell J.J., Larach D.R., 1973, An Inversion in the Atmosphere of Titan, Icarus, **20**, 437–+

Dermott S.F., Sagan C., 1995, Tidal Effects of Disconnected Hydrocarbon Seas on Titan, , **374**, 238–+

Evans K.F., 1998, The spherical harmonic discrete ordinate method for three-dimensional atmospheric radiative transfer, J. Atmos. Sci, **55**, 429–446.

Evans K.F., Stephens G.L., 1991, A new polarized atmospheric radiative transfer model, Journal of Quantitative Spectroscopy and Radiative Transfer, **46**, 413–423

Flasar F.M., Conrath B.J., 1990, Titan's stratospheric temperatures - A case for dynamical inertia?, Icarus, **85**, 346–354

Flasar F.M., Samuelson R.E., Conrath B.J., 1981, Titan's atmosphere - Temperature and dynamics, , **292**, 693–698

Fry E.S., Katawar G.W., 1981, Relationships between elements of the stokes matrix, Appl. Opt., **20**, 2811–2814

Goody R.M., Yung Y.L., Atmospheric Radiation: Theoretical basis (Oxford University Press, New York, 1989)

Grieger B., Lemmon M.T., Markiewicz W.J., Keller H.U., 2002, Inverse radiation modeling of Titan's atmosphere to assimilate Solar Aureole Imager data of the Huygens probe, Planet. Space Sci.

Grieger B., Rodin A.V., Salinas S.V., Keller H.U., 2003, Simultaneous retrieval of optical depths and scattering phase functions in Titan's atmosphere from Huygens/DISR data, Planet. Space Sci. (submitted)

Griffith C.A., 1993, Evidence for surface heterogeneity on Titan, , **364**, 511–514

Hansen J.E., Travis L.D., 1974, Light scattering in planetary atmospheres, Space Science Reviews, vol. 16, Oct. 1974, p. 527-610., **16**, 527–610

Herman B.M., Ben-David A., Thome K.J., 1994, Numerical technique for solving the radiative transfer equation for a spherical shell atmosphere, , **33**, 1760–1770

Hovenier J.W., 1970, Principles of Symmetry for Polarization Studies of Planets, , **7**, 86–+

Israel G., Chassefiere E., Cabane M., Raulin F., Boon J.J., 1991, Aerosols in Titan's atmosphere - Models, sampling techniques and chemical analysis, Annales Geophysicae, **9**, 1–13

Jackson J.D., Classical Electrodynamics (John Wiley Sons, Inc., New York, 1962)

Jaffe W., Caldwell J., Owen T., 1980, Radius and brightness temperature observations of Titan at centimeter wavelengths by the Very Large Array, , **242**, 806–811

Jones P.D., Bayazittoglu Y., 1992, Coordinate systems for the radiative transfer equation in curvilinear media, Journal of Quantitative Spectroscopy and Radiative Transfer, **48**, 427–440

Karkoschka E., 1994, Spectrophotometry of the jovian planets and Titan at 300- to 1000-nm wavelength: The methane spectrum, Icarus, **111**, 174–192

—, 1998, Methane, Ammonia, and Temperature Measurements of the Jovian Planets and Titan from CCD-Spectrophotometry, Icarus, **133**, 134–146

Karkoschka E., Lorenz R.D., 1997, Latitudinal Variation of Aerosol Sizes Inferred from Titan's Shadow, Icarus, **125**, 369–379

King M.D., 1983, Number of terms required in the Fourier expansion of the reflection function for optically thick atmospheres, Journal of Quantitative Spectroscopy and Radiative Transfer, **30**, 143–161

Kuo K., Weger R.C., Welch R.M., 1995a, The picard iterative approximation to the solution of the integral equation of radiative transfer–Part 1. The plane–parallel case, Journal of Quantitative Spectroscopy and Radiative Transfer, **53**, 425–444

Kuo K., Weger R.C., Welch R.M., Cox R.M., 1995b, The picard iterative approximation to the solution of the integral equation of radiative transfer–Part 2. Three- dimensional geometry, Journal of Quantitative Spectroscopy and Radiative Transfer, **55**, 195–213

Lammer H., Stumptner W., Bauer S.J., 1998, Dynamic escape of H from Titan as consequence of sputtering induces heating, Planet. Space Sci., **46**, Nr. 9/10, 1207–1213

Lara L.M., Lorenz R.D., Rodrigo R., 1994, Liquids and solids on the surface of Titan: Results of a new photochemical model, , **42**, 5–14

Lellouch E., Coustenis A., Gautier D., Raulin F., Dubouloz N., Frère C., 1989, Titan's atmosphere and hypothesized ocean: A reanalysis of the Voyager 1 radio-occultation and IRIS 7.7 μm data, Icarus, **79**, 328–349

Lemmon M.T., 1994, Properties of Titan's haze and surface, Dissertation, University of Arizona

Lemmon M.T., Karkoschka E., Tomasko M., 1993, Titan's rotation - Surface feature observed, Icarus, **103**, 329–332

—, 1995, Titan's rotational light-curve, Icarus, **113**, 27–38

Lenoble J., Radiative transfer in scattering and absorbing atmospheres: standard computational procedures (Deepak publishing, Hampton, Virginia, 1985)

Lindal G.F., Wood G.E., Hotz H.B., Sweetnam D.N., Eshleman V.R., Tyler G.L., 1983, The atmosphere of Titan - an analysis of the Voyager 1 radio occultation measurements, Icarus, **53**, 348–363

Liou K.N., An introduction to atmospheric radiation (Academic Press, San Diego, California, 1980)

Lockwood G.W., 1977, Secular brightness increases of Titan, Uranus, and Neptune, 1972-1976, Icarus, **32**, 413–430

Lockwood G.W., Lutz B.L., Thompson D.T., Bus E.S., 1986, The albedo of Titan, , **303**, 511–520

Lockwood G.W., Thompson D.T., 1979, A relationship between solar activity and planetary albedos, , **280**, 43–45

Lorenz R.D., Smith P.H., Lemmon M.T., Karkoschka E., Lockwood G.W., Caldwell J., 1997, Titan's North-South Asymmetry from HST and Voyager Imaging: Comparison with Models and Ground-Based Photometry, Icarus, **127**, 173–189

Lutz B.L., de Bergh C., Owen T., 1983, Titan - Discovery of carbon monoxide in its atmosphere, Science, **220**, 1374–+

Marchuk G.I., Mikhailov G.A., Nazaraliev M.A., The Monte Carlo methods in atmospheric optics (Springer Series in Optical Sciences, Berlin: Springer, 1980, 1980)

Markiewicz W.J., Keller H.U., Thomas N., Titov D., Forget F., 2002, Optical properties of the Martian aerosols in the visible spectral range, Advances in Space Research, **29**, 175–181

Markiewicz W.J., Sablotny R.M., Keller H.U., Thomas N., Titov D., Smith P.H., 1999, Optical properties of the Martian aerosols as derived from Imager for Mars Pathfinder midday sky brightness data, , **104**, 9009–9018

McGrath M.A., Courtin R., Smith T.E., Feldman P.D., Strobel D.F., 1998, The Ultraviolet Albedo of Titan, Icarus, **131**, 382–392

McKay C.P., Pollack J.B., Courtin R., 1989, The thermal structure of Titan's atmosphere, Icarus, **80**, 23–53

McKay C.P., Pollack J.B., Courtin R., 1991, The greenhouse and antigreenhouse effects on Titan, Science, **253**, 1118–1121

Ng K.C., 1974, Hypernetted chain solutions for the classical one-component plasma up to Gamma equals 7000, , **61**, 2680–2689

O'Brien D.M., 1992, Accelerated quasi Monte Carlo integration of the radiative transfer equation, Journal of Quantitative Spectroscopy and Radiative Transfer, **48**, 41–59

Oikarinen L.E., Sihvola E., Kyrola E., 1999, Multiple scattering radiance in limb-viewing geometry, , **104 (D24)**, 31261–31275

Owen T., 1982, The composition and origin of Titan's atmosphere, , **30**, 833–838

Podolak M., Bar-Nun A., 1979, A constraint on the distribution of Titan's atmospheric aerosol, Icarus, **39**, 272–276

Rages K., Pollack J.B., 1983, Vertical distribution of scattering hazes in Titan's upper atmosphere, Icarus, **55**, 50–62

Rannou P., Cabane M., Botet R., Chassefière E., 1997, A new interpretation of scattered light measurements at Titan's limb, , **102**, 10997–11014

Rannou P., Cabane M., Chassefiere E., 1993, Growth of aerosols in Titan's atmosphere and related time scales - A stochastic approach, , **20**, 967–970

Rannou P., Cabane M., Chassefiere E., Botet R., McKay C.P., Courtin R., 1995, Titan's geometric albedo: Role of the fractal structure of the aerosols, Icarus, **118**, 355–372

Rodin A.V., 2002, On the moment method of modeling microphysics of clouds in rariied turbulent atmospheres. I Condensation and mixing, Solar System Res., **36**, Nr. 2, 97–106

—, 2003, On the moment method of modeling microphysics of clouds in rariied turbulent atmospheres. II Stochastic coagulation, Solar System Res.

Rozanov A., Rozanov V., Burrows J.P., 2001, A numerical radiative transfer model for a spherical planetary atmosphere: combined differential-integral approach involving the picard iterative approximation, Journal of Quantitative Spectroscopy & Radiative Transfer, **69**, 491–512

Rozanov A.V., Rozanov V.V., Burrows J.P., 2000, Combined differential-integral approach for the radiation field computation in a spherical shell atmosphere: Nonlimb geometry, , **105**, 22937–22942

Salinas S.V., Grieger B., Rodin A.V., Keller H.U., 2003, A spherical model for computing polarized radiation in Titan's atmosphere, Planet. Space Sci. (submitted)

Samuelson R.E., Hanel R.A., Kunde V.G., Maguire W.C., 1981, Mean molecular weight and hydrogen abundance of Titan's atmosphere, , **292**, 688–693

Samuelson R.E., Nath N.R., Borysow A., 1997, Gaseous abundances and methane supersaturation in Titan's troposphere, , **45**, 959–980

Sen K., Wilson S., Radiative transfer in curved media (World scientific publishing, Singapore, 1990)

Smith G.R., Strobel D.F., Broadfoot A.L., Sandel B.R., Shemansky D.E., Holberg J.B., 1982, Titan's upper atmosphere - Composition and temperature from the EUV solar occultation results, , **87**, 1351–1359

Smith P.H., Tomasko M.G., Britt D., Crowe D.G., Reid R., Keller H.U., Thomas N., Gliem F., Rueffer P., Sullivan R., Greeley R., Knudsen J.M., Madsen M.B., Gunnlaugsson H.P., Hviid S.F., et al., 1997, The imager for Mars Pathfinder experiment, , **102**, 4003–4026

Sobolev V., Light scattering in planetary atmospheres (Pergamon press, Oxford, 1975)

Sromovsky L.A., Suomi V.E., Pollack J.B., Kraus R.J., Limaye S.S., Owen T., Revercomb H.E., Sagan C., 1981, Implications of Titan's north-south brightness asymmetry, Nature, **292**, 698–702

Tanguy L., Bezard B., Marten A., Gautier D., Gerard E., Paubert G., Lecacheux A., 1990, Stratospheric profile of HCN on Titan from millimeter observations, Icarus, **85**, 43–57

Tegmark M., 1996, An Icosahedron-Based Method for Pixelizing the Celestial Sphere, , **470**, L81+

Tomasko M.G., Doose L.R., Smith P.H., West R.A., Soderblom L.A., Combes M., Bézard B., Coustenis A., deBergh C., Lellouch E., Rosenqvist J., Saint-Pé O., Schmitt B., Keller H.U., Thomas N., Gliem F., The Descent Imager/Spectral Radiometer (DISR) aboard Huygens, in: A. Wilson (Hg.), Huygens Science, Payload and Mission, Bd. SP-1177, S. 109–138 (ESA Publications Division, ESTEC, Noordwijk, The Netherlands, 1997)

Tomasko M.G., Smith P.H., 1982, Photometry and polarimetry of Titan: Pioneer 11 observations and their implications for aerosol properties, Icarus, **51**, 65–95

Toon O.B., McKay C.P., Courtin R., Ackerman T.P., 1988, Methane rain on Titan, Icarus, **75**, 255–284

Toon O.B., McKay C.P., Griffith C.A., Turco R.P., 1992, A physical model of Titan's aerosols, Icarus, **95**, 24–53

Toon O.B., McKay C.P., Pollack J.B., 1980, A physical model of Titan's aerosols, Icarus, **43**, 260–282

Vaillon R., Lallemand M., Lemonnier D., 1996, Radiative heat transfer in orthogonal curvilinear coordinates using the discrete ordinates method, Journal of Quantitative Spectroscopy & Radiative Transfer, **55**, 7–17

Van de Hulst H.C., Light scattering by small particles (Dover, New York, 1957)

West R.A., Lane A.L., Hart H., Simmons K.E., Hord C.W., Coffen D.L., Esposito L.W., Sato M., Pomphrey R.B., 1983, Voyager 2 photopolarimeter observations of Titan, J. geophys. Res., **88**, 8699–8708

West R.A., Smith P.H., 1991, Evidence for aggregate particles in the atmospheres of Titan and Jupiter, Icarus, **90**, 330–333

Wiscombe W., 1977, The delta-M method: Rapid yet accurate radiative flux calculations for strongly asymmetric phase functions, Journal of Atmospheric Sciences, **36**, 1408–1422

Yelle R.V., et al., The Yelle Titan Atmosphere Engineering Models, in: Huygens: Science, Payload and Mission, S. 243–+ (1997)

Yung Y.L., Allen M., Pinto J.P., 1984, Photochemistry of the atmosphere of Titan: Comparison between model and observations, Astrophys. J. Suppl. Ser., **55**, 465–506

Acknowledgments

I thank my supervisors at MPAe, Dr. habil. Horst Uwe Keller and Dr. Wojciech Markiewicz, for posing this challenging problem as my thesis topic and for their continuous guidance and sharing of knowledge in the subject. Also, the completion of this thesis relied highly on their active part of my work. Thanks Uwe! Thanks Wojciech!.

I also thank my supervisor, at the Universitäts–Sternwarte Göttingen, Prof. Dr. Franz Kneer for accepting me as his Ph.D. student at the Physics Dep., for sharing some enlightening discussions and for the opportunity to share my work at the observatory's seminars. Gracias Franz!.

Special thanks to my colleague and friend Dr. Björn Grieger, for his patience and interest in my work, and for the countless opportunities in which we discussed serious problems at tea time. Thanks Björn!.

Many thanks to Dr. Robert A. West, for hosting me at NASA–JPL labs, during the first months of my thesis. His knowledge of radiative transfer has helped enormously to expand my horizons on the subject and to become acquainted with research in planetary science. Thanks Bob!.

Also many thanks to our two secretaries, Andrea Macke and Sabine Stelzer, thanks to them, things have run smoothly and they helped to solve many problems during my stay.

Writing this acknowledgment I immediately recall the many good times with my colleagues and friends at MPAe, especially with Francisco Frutos, now in Costa Rica, who helped me to settle in Lindau and to understand the German way of life. Ho–Tra–Mi, who is now at Bern, for all her help during this last two years and for being the perfect office–mate. To the Spanish–speaking gang, Geronimo Villanueva, Luciano Rodriguez, Hebe Cremades and JuanMa Borrero for the innumerable long nights discussing work and life and making me feel like I was at home. To Ganna Portyankina, Ai Inada and Elena Podladchikova for forcing me (almost), with a cup of tea, to have a break when I was under pressure specially the last weeks before the completion of this thesis.

I would like to keep adding people to this acknowledgment, but it would become way too long. Anyway, the majority of the people from MPAe and MPRS are acknowledged.

Financial support from the Max–Planck–Institüt für Aeronomie and the Max–Planck Society is gratefully acknowledged.

Finally and most important, I thank my parents, Manuel and Azucena, my brothers Marco, Fausto and Luis and my sister Aurora for the tremendous support and love, even when I sacrificed my time with them to follow my goals. To my long time partner, Elsie Duvenage, for her close support, love and encouragement during these years, for being there when I needed her most and for believing in me. Without her, this thesis wouldn't have been possible.

Scientific contributions

Conference Contributions :

[1] Salinas, S.V., Grieger, B., Markiewicz, W.J., Keller, H.U. *Simulating the internal polarized radiation field of Titan as seen from Huygens/DISR with a new spherical model.* European Geophysical Society XXVII General Assembly, Nice, France, 2002.

[2] Salinas, S.V., Rodin A. V., Markiewicz, W.J., Keller, H.U. *A spherical model for polarized radiation in Titan's atmosphere.* American Astronomical Society, DPS meeting # 34, Birmingham, Alabama, Oct. 2002.

Publications :

[1] S.V. Salinas, B. Grieger, H. U. Keller, *A spherical model for computing polarized radiation in Titan's atmosphere.* Planet.& Space Sci. 2003/2004 (accepted)

[2] B. Grieger, A. V. Rodin, S. V. Salinas, H. U. Keller, *Simultaneous retrieval of optical depths and scattering phase functions in Titan's atmosphere from Huygens/DISR data.* Planet.& Space Sci. 2003/2004 (accepted)

Lebenslauf

Persönliche Daten

Name : Santo Valentin Salinas Cortijo

Geburstdatum : July 20, 1967

Geburstsort : Chimbote, Peru

Staatsangehörigkeit : Peruanisch

Schulbildung

04/1973–12/78 : Grundschule an der Colegio Nacional “Jose Olaya”
88014, Chimbote, Peru

04/1979–12/83 : Weiter führende schule Colegio Nacional “Jose Olaya”
88014, Chimbote, Peru

Studium

04/1987–08/91 : Ingenieur–Studium (Energie–Technik) an der Universidad Nacional del Santa, Chimbote, Peru.

08/1991 : Zwischenprufüng (Vordiplom gleichwertig)

02/1993–12/97 : Physikstudium an der University of South–Africa, Pretoria, Südafrika

05/2001 : Bakkalaureus der Wissenschaften

08/1998–12/00 : Studium der Numerischen und Angewandte Mathematik an der Kungl Tekniska Högskolan, Stockholm, Schweden.

12/2000 : Diplomprufüng
Thema : *Modeling and optimization of electric and optical properties of semiconductor spatial light modulators.*

Seit 09/2001 : Physikstudium (promotion) an der Georg-August- Universität Göttingen

Anstellung

04/1987–07/91 : Studienarbeit, Fakultät für Ingenieurwesen (Energie),
Universidad Nacional del Santa, Chimbote, Peru.

01/1992–12/95 : Lehrer für Spanisch und Englisch
IEC Technical College, Kumamoto, Japan.

02/1993–12/97 : Studienarbeit (im Fernstudium) an der
University of South–Africa, Pretoria, Südafrika

01/1995–07/98 : Bauingenieur mathematische modellierung und analyse
Supersymmetry Services Pte. Ltd., Singapore.

08/1998–12/00 : Diplomarbeit (M.Sc.) an der Kungl Tekniska Högskolan,
Stockholm, Schweden.

Seit 04/2000 : Max-Planck-Stipendiat (Doktorand).
Max-Planck-Institut für Aeronomie, Katlenburg-Lindau,